MANCHESTER 1824

The University of Manchester

Unified semi-analytical wall boundary conditions for inviscid, laminar and turbulent slightly compressible flows in *SPARTACUS-2D* combined with an improved time integration scheme on the continuity equation.

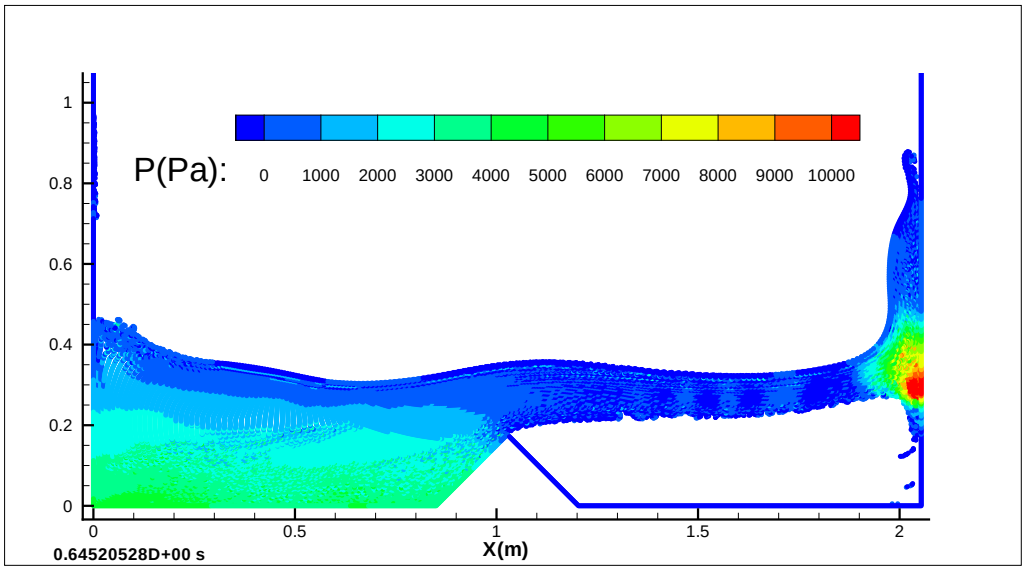

Martin FERRAND

martin.ferrand@ponts.org

A thesis submitted to the University of Manchester

for the degree of Master of Philosophy

in the Faculty of Engineering and Physical Sciences

School of Mechanical, Aerospace and Civil Engineering

February 17, 2011

Contents

List of Figures

List of Tables

Unified semi-analytical wall boundary conditions on non-viscid, laminar and turbulent slightly compressible flows in *SPARTACUS-2D* combined with an improved time scheme integration on the continuity equation.

Abstract

Smoothed Particle Hydrodynamics (*SPH*) is a meshless Lagrangian numerical method ideal for simulating potentially violent free-surface phenomena such as a wave breaking, or a dam break where many Eulerian methods can be difficult to apply.

Dealing with wall boundary conditions is one of the most challenging parts of the *SPH* method and many different approaches have been developed among (*i*) repulsive forces such as Lennard-Jones one, which is efficient to give impermeable boundaries but leads to non-physical behaviours, (*ii*) fictitious (or ghost) particles which provide a better physical behaviour in the vicinity of a wall but are hard to define for complex geometries and (*iii*) semi-analytical approach such as Kulasegaram *et al.* [15] which consists of renormalising the density field near a solid wall with respect to the missing kernel support area. The present work extends this semi-analytical methodology, where intrinsic *gradient* and *divergence* operators are employed that ensure conservation properties. The accuracy of the physical field such as the pressure next to walls is considerably improved, and the consistent manner developed to wall-correct operators allows us to perform simulations with turbulence models. This work will present three key advances:

- The time integration scheme used for the continuity equation requires particular attention, and as already mentioned by Vila (1999), we prove there is no point in using a dependence in time of the particles' density if no kernel gradient corrections are added. Thus, by using a near-boundary kernel-corrected version of the time integration scheme of the form proposed by Vila, we are able to simulate long-time simulations ideally suited for turbulent flow in a channel in the context of accurate boundary conditions.

- In order to compute the kernel correction, Feldman and Bonet [9] use an analytical value which is computationally expensive whereas Kulasegaram *et al.* [15] and De Leffe *et al.* [7] use polynomial approximation which can be difficult to define for complex geometries. We propose here to compute the renormalisation term of the kernel support near a solid with a novel time integration scheme, allowing us any shape for the boundary.

- All boundary terms issued from the continuous approximation are given by surface summations which only require information from a mesh file of the boundary. The technique developed here allows us to correct the pressure gradient and viscous terms and hence provide a physically correct wall-shear stress so that even the diffusion equation of a scalar quantity can be solved accurately using *SPH* such as the turbulent kinetic energy or its dissipation in a $k - \epsilon$ model of turbulence.

The new model is demonstrated for cases including hydrostatic conditions for a channel flow, still water in a tank of complex geometry and a dam break over triangular bed profile with sharp angle where significant improved behaviour is obtained in comparison with the conventional boundary techniques. Simulation of the benchmark test case of a square object moving in an enclosed tank is shows good agreement with the reference solution and no voids are formed within the fluid domain. The performance of the model for a $2 - D$ turbulent flow in a channel is demonstrated where the profiles of velocity, turbulent kinetic energy and its dissipation are in agreement with the theoretical ones. Finally, the performance of the model is demonstrated for flow in a fish-pass where velocity field and turbulent viscosity field are satisfactory reproduced compared to mesh-based codes.

Declaration

No portion of the work referred to in the thesis has been submitted in support of an application for another degree or qualification of this or any other university or other institute of learning.

Copyright

Acknowledgements

This Mphil thesis would not have been possible unless *EDF R&D* have sponsored my research. I am also really grateful to Pr. Dominique LAURENCE, my supervisor, who relied on me since the beginning, helped me with plenty of ideas and pieces of advice. I owe my deepest gratitude to Dr. Benedict ROGERS, my first advisor who kept encouraging me, guiding me and forced me to be more organized in my work. I would like to thank Damien VIOLEAU, my French advisor, who always trusted in me, and made me the honour to be an informal reviewer of his book. He has also made available his support in a number of ways such as really picky reviewing of my presentations and reports.

I would like to show my gratitude to Pr. Peter STANSBY, Head of School MACE, who showed me an interest in my work.

I am indebted to my many of my colleagues and friends to support me: Juan URIBE who solved my computer problems, Stefano ROLFO who welcome me in a wonderful way with a tasty Italian food, and finally all the French Mancunian connection, Charles MOULINEC who gave me pieces of advice, Nicolas CHINI who gave me a part of his wisdom, Christophe KASSIOTIS who followed in details my work and was an important support, Flavien BILLARD who was more than a big Brother and Victor PEPIN, who tried to learn me how to play football against English people.

Finally, I would like to thank my French school, l'École des Ponts Paritech, to have given me the chance to live my last year of study abroad.

Chapter 1

Introduction

1.1 Background

Smoothed Particle Hydrodynamics (*SPH*) is a meshless Lagrangian method used to simulate flows in fluid mechanics. The Lagragian point of view may be compared to the Eulerian one: the first one consists in studying a flow following fluid particles. Each physical quantity is then attached to its fluid element and transported with it with respect to the laws of physics. On the contrary, Eulerian approaches study physical quantities at a fixed position. Many methods such as finite differences, finite volumes and finite elements are originally based on that approach, which are also called mesh-based methods. Although they have been successfully used for many engineering problems and have been developed to perform simulations for industry, they still face problems to simulate highly non-linear deformations such as a $3D$ dam break for instance.

SPH is one of the most used Lagrangian techniques. Due to its meshless formulation, *SPH* is easily able to simulate merging domains, and due to its Lagrangian formulation, it does not diffuse any interface. It was first introduced by Lucy [18], and Gingold and Monaghan [11]. The use of *SPH* has since widely expanded in fluid dynamics and solid mechanics [25] although its original applications were in astrophysics. The basic concept of *SPH* is that continuous media are represented by discrete particles with volume, density and mass. The particles have a kernel function to define their range of interaction, and the fields are approximated by integral interpolations which is nothing else but the convolution of the variable with the kernel function.

1.1.1 Overview of where *SPH* is going

This section aims to present a non exhaustive list of fields where *SPH* has been developed and used.

First of all, the *SPH* method was invented primarily to investigate and carry out astrophysics simulations. This method was particularly better suited that mesh-based Eulerian approach for: strong non-linear interactions between cosmic objects and high deformations, concentration of masses and empty areas. *SPH* was for instance used for the star collisions and galaxy formation predictions (see Patsis [29]).

Secondly, although widely developed and used through finite elements methods, solid mechanics found an interest to investigate the *SPH* method to compute cases where grid-based approaches face problems: we may cite for instance fracture an fragmentation of a solid. Indeed, when one studies fracture, one should be able to refine meshes where large distortion appears, to be accurate. Knowing where a discontinuity will occur before the simulation is a difficult problem to handle. On the contrary, as a grid-less method, *SPH* treats this sort of problem easily into account. We could refer for example to Das and Cleary [6] who used the SPH method to successfully simulate the $3D$ fracture and fragmentation in a thin plate.

Last, but not least, *SPH* has been adapted to perform fluid mechanics simulation in cases, mainly for violent deforming with complex free-surface flow. Two major variants exist:

(i) a weakly compressible version where the pressure is obtained analytically by an equation of state. The Mach number, based on a numerical speed of sound, is supposed to be less than 10%, and

(ii) a incompressible version, where the pressure field is obtained solving a Poisson's equation to enforce incompressibility (see Xu [37] for a state-of-the-art).

The approach (i) was introduced first, and has as drawbacks a relatively small time step due to the numerical speed of sound and the pressure field can be impacted by small perturbations of the density field. The main advantages are to ensure naturally free-surface condition for pressure without imposing it. However, method (ii) allows bigger time steps in the time schemes and gives smoother pressure field, but requires a Poisson problem to be solved and to enforce pressure boundary condition at the free surface.

We have chosen here to investigate the weakly version of *SPH* mainly because of its simplicity. However, as it will be mentioned in Chapter 2, further developments herein can be extended to the incompressible version.

Plenty of industrial studies using *SPH* have been carried out over the last decades. Among these, we can cite Marongiu *et al.* [19] who performed simulations of a jet impacting a Pelton turbine. The complexity of the flow makes *SPH* more efficient than other mesh-based methods.

1.1.2 Objectives of this work

As one of the most challenging part of *SPH*, the representation and the treatment of solid walls require a special care. To model the Eulerian wall, which move with a prescribed velocity, in a Lagrangian fluid field which

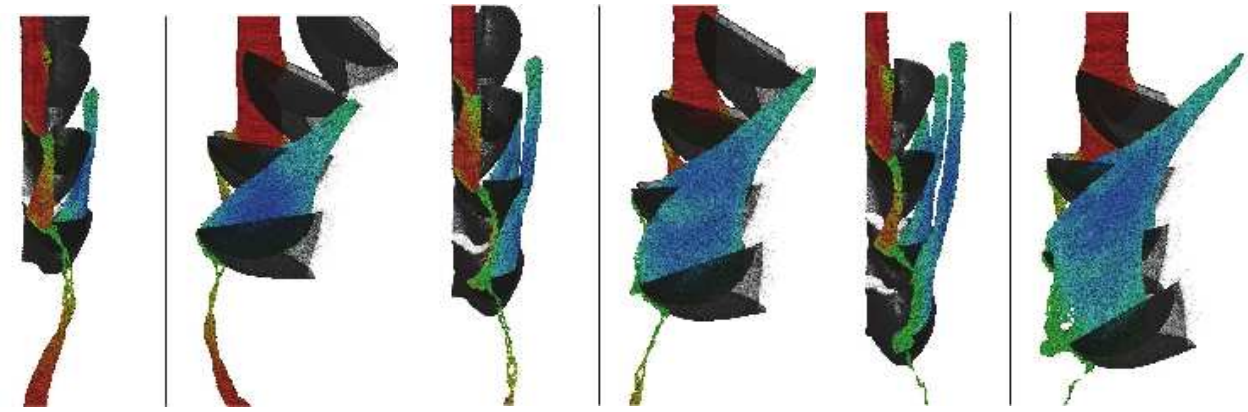

(a) $T = 8.6ms$ (b) $T = 10.6ms$ (c) $T = 12.6ms$

Figure 1.1: Views of the flow in rotating buckets in a Pelton turbine at different times, along X axis (left) and Z axis (right) simulated by Marongiu *et al.* [19]. Fluid particles are coloured by their velocity.

moves with the flow velocity is the root of the problem. Moreover, as every bounded physical problem, we must impose boundary Neumann or Dirichlet conditions on various field such as the pressure field or scalar field.

Many techniques have been developed over the past decades with their own advantages and disadvantages. The present work aims at proposing an Eulerian analytical approach to model solid boundaries. The theoretical work is done in $2D$ and tested with the code *SPARTACUS-2D* (see [4]) developed at *EDF R&D*. However, we tried to keep as general the developments in order to, *in fine*, adapt it to the $3D$. Thus the goal is to obtain a method allowing complex geometries without any so-called *fictitious* particles. Given the overall aim of the current research effort is to deal with turbulence and behaviour near the wall, accurate and physical boundary conditions on scalar fields are required.

The most sophisticated versions of *SPH* such as arbitrary Eulerian-Lagrangian formulation combined with the solving of Riemann problems, or again the incompressible formulation, are not considered here as we first of all seek to keep as simple as possible the treatment of walls. Note that present improvements might be adapted to the other formulations.

1.1.3 Structure of the report

This thesis is composed of three chapters and is an extension of Ferrand *et al.* [10]. The first Chapter presents briefly the aim of *SPH* and its field of application before introducing basic equations and important remarks for the thesis. Chapter 2 aims at setting out a semi-analytical approach to deal with boundary conditions in *SPH*, combined with a conservative time integration scheme. Particular effort is made to explain the methodology chosen and to generalize the different formulations to a generic *SPH* problem. Finally in the third chapter, new formulations are tested against the existing ones, compared to analytical solutions and confronted to other discretization techniques such as the finite differences approach.

1.2 Basic *SPH* formulations for slightly compressible Newtonian fluid

1.2.1 Conservative governing equations

The slightly compressible Newtonian fluid is modelled by a set of particles denoted by the subscripts $(.)_a$ and $(.)_b$ in a domain Ω. The set of all the fluid particles is denoted by $\mathcal{F}$. Each particle $a \in \mathcal{F}$ possesses information such as its mass m_a (assumed constant), its position $\mathbf{r}_a$, its velocity $\mathbf{u}_a$ which is the Lagrangian derivative of the position, its density ρ_a, its volume $V_a = \frac{m_a}{\rho_a}$, and its pressure p_a. The spatial discretization is based on a weighting interpolation with a kernel function w with a compact support. Ω_a then refers to the support of the kernel function centred in $\mathbf{r}_a$ of radius R. We generally denote by the subscripts $(.)_{ab}$ the difference of a quantity between the positions a and b. For instance $\mathbf{u}_{ab} \equiv \mathbf{u}_a - \mathbf{u}_b$ and $\mathbf{r}_{ab} \equiv \mathbf{r}_a - \mathbf{r}_b$. Two exceptions are

made with the following notations $w_{ab} \equiv w(\mathbf{r}_{ab})$ and $\boldsymbol{\nabla} w_{ab} \equiv \boldsymbol{\nabla}_a w(\mathbf{r}_{ab})$. Here, the symbol $\boldsymbol{\nabla}_a$ denotes the *gradient* at the point $\mathbf{r}_a$ [1]. With these notations, a commonly used form of the continuity equation is (see *e.g.* [23]):

$$\frac{\mathrm{d}\rho_a}{\mathrm{d}t} = \sum_{b \in \mathcal{F}} m_b \boldsymbol{\nabla} w_{ab}.\mathbf{u}_{ab} \tag{1.1}$$

where $\frac{\mathrm{d}}{\mathrm{d}t}$ denotes the Lagrangian derivative, that is to say the derivative along the particle path. It can be derived from the following definition of the density:

$$\rho_a = \sum_{b \in \mathcal{F}} m_b w_{ab} \tag{1.2}$$

The inviscid momentum equation can be written as follows:

$$\frac{\mathrm{d}\mathbf{u}_a}{\mathrm{d}t} = -\sum_{b \in \mathcal{F}} m_b \left(\frac{p_a}{\rho_a^2} + \frac{p_b}{\rho_b^2} \right) \boldsymbol{\nabla} w_{ab} + \mathbf{g} \tag{1.3}$$

where $\mathbf{g}$ is the gravity field. The equation of state links density and pressure:

$$p_a = \frac{\rho_0 c_0^2}{\gamma} \left[\left(\frac{\rho_a}{\rho_0} \right)^{\gamma} - 1 \right] \tag{1.4}$$

where ρ_0 is the reference density of the fluid, c_0 is the speed of sound and $\gamma = 7$ for water.

The speed of sound is in fact a numerical parameter. The time step in *SPH* can vary and must obey three conditions. One of these is based on the speed of sound c_0:

$$\delta t \leq 0.4 \frac{h}{c_0} \tag{1.5}$$

Hence, if we decrease c_0, with the knowledge that c_0 should be greater than 10 times the maximum velocity, we increase the time step δt.

One can check that these equations satisfy the following conservation equations of linear and angular momentum:

$$\begin{aligned} \sum_{a \in \mathcal{F}} \mathbf{F}_a^{int} &= 0 \\ \sum_{a \in \mathcal{F}} \mathbf{r}_a \times \mathbf{F}_a^{int} &= \mathbf{0} \end{aligned} \tag{1.6}$$

where $\mathbf{F}_a^{int} \equiv -m_a \sum_{b \in \mathcal{F}} m_b \left(\frac{p_a}{\rho_a^2} + \frac{p_b}{\rho_b^2} \right) \boldsymbol{\nabla} w_{ab}$. The properties (1.6) holds if the kernel w verifies properties of isotropy (which implies symmetry,*ie* $w_{ab} = w_{ba}$ and implies that $\boldsymbol{\nabla} w_{ab} = -\boldsymbol{\nabla} w_{ba}$ and $\boldsymbol{\nabla} w_{ab}$ is collinear to $\mathbf{r}_{ab}$).

Operator definitions

We can define operators gradient ($\mathbf{Grad}_a\{A_b\}$) and divergence ($\mathrm{Div}_a\{\mathbf{A}_b\}$) of discrete scalar or vector fields ($\{A_b\}$ or $\{\mathbf{A}_b\}$) as:

$$\begin{aligned} \mathbf{Grad}_a\{A_b\} &\equiv \rho_a \sum_{b \in \mathcal{F}} m_b \left(\frac{A_a}{\rho_a^2} + \frac{A_b}{\rho_b^2} \right) \boldsymbol{\nabla} w_{ab} \\ \mathrm{Div}_a\{\mathbf{A}_b\} &\equiv -\frac{1}{\rho_a} \sum_{b \in \mathcal{F}} m_b \mathbf{A}_{ab}.\boldsymbol{\nabla} w_{ab} \end{aligned} \tag{1.7}$$

[1] the gradient operator is defined by $\boldsymbol{\nabla}_a \equiv \mathbf{e}_x \frac{\partial}{\partial x_a} + \mathbf{e}_y \frac{\partial}{\partial y_a} + \mathbf{e}_z \frac{\partial}{\partial z_a}$, ($\mathbf{e}_x$, $\mathbf{e}_y$, $\mathbf{e}_z$) being the basis vector triad of the Cartesian coordinate system in $3D$.

where $\mathbf{A}_{ab} \equiv \mathbf{A}_a - \mathbf{A}_b$. Thus the equation of continuity (1.1) and the momentum equation (1.3) can be rewritten as follows:

$$\begin{array}{rcl} \dfrac{\mathrm{d}\rho_a}{\mathrm{d}t} & = & -\rho_a \mathrm{Div}_a\{\mathbf{u}_b\} \\ \dfrac{\mathrm{d}\mathbf{u}_a}{\mathrm{d}t} & = & -\dfrac{1}{\rho_a}\mathbf{Grad}_a\{p_b\} + \mathbf{g} \end{array} \tag{1.8}$$

The operators $\mathbf{Grad}_a$ and Div_a are said to be skew-adjoint (see Appendix A.3 for details), in other words, for two arbitrary fields of scalar $\{A_b\}$ and of vector $\{\mathbf{B}_b\}$, we have the property:

$$\langle \mathbf{Grad}_b\{A_a\},\, \mathbf{B}_b\rangle = -\left(A_b,\, \mathrm{Div}_b\{\mathbf{B}_a\}\right) \tag{1.9}$$

where the inner products are defined by a sum over the domain:

$$\begin{array}{rcl} \langle \mathbf{A}_b,\, \mathbf{B}_b\rangle & \equiv & \displaystyle\sum_{b\,\in\,\mathcal{F}} V_b \mathbf{A}_b.\mathbf{B}_b \\ (A_b,\, B_b) & \equiv & \displaystyle\sum_{b\,\in\,\mathcal{F}} V_b A_b B_b \end{array} \tag{1.10}$$

This property, which also holds for the continuous operators, could be used in simple variational calculus as follows, which is important for the conservation of the energy for instance. Indeed, if we compute the work the virtual displacement field $\{\mathrm{d}\mathbf{r}_b\}$, we obtain:

$$\begin{array}{rcll} \displaystyle\sum_{b\,\in\,\mathcal{F}} \mathbf{F}_b^{int}.\mathrm{d}\mathbf{r}_b & = & \left\langle \dfrac{\rho_b}{m_b}\mathbf{F}_b^{int},\, \mathrm{d}\mathbf{r}_b \right\rangle & (1.11a) \\ & = & -\displaystyle\sum_{a,b\,\in\,\mathcal{F}} m_a \frac{p_a}{\rho_a^2}\frac{\partial \rho_a}{\partial \mathbf{r}_b}.\mathrm{d}\mathbf{r}_b & (1.11b) \\ & = & -\displaystyle\sum_{a\,\in\,\mathcal{F}} V_a \frac{p_a}{\rho_a}\mathrm{d}\rho_a & (1.11c) \\ & = & \displaystyle\sum_{a\,\in\,\mathcal{F}} V_a p_a \mathrm{Div}_a\{\mathrm{d}\mathbf{r}_c\} & (1.11d) \\ & = & (p_b,\, \mathrm{Div}_b\{\mathrm{d}\mathbf{r}_c\}) & (1.11e) \\ & = & -\langle \mathbf{Grad}_b\{p_a\},\, \mathrm{d}\mathbf{r}_b\rangle & (1.11f) \end{array}$$

In the previous calculus, we have used the definition of the inner products (1.10) in the first line, then the definition of the internal forces in the second one, then the definition of the differential in the third one, the fourth line is nothing but the continuity equation, and finally the adjoint property (1.9) is used in the last line.

The previous calculus proves that for any virtual displacement field $\{\mathrm{d}\mathbf{r}_b\}$, the inner products $\left\langle \dfrac{\rho_b}{m_b}\mathbf{F}_b^{int},\, \mathrm{d}\mathbf{r}_b \right\rangle$ and $-\langle \mathbf{Grad}_b\{p_a\},\, \mathrm{d}\mathbf{r}_b,\rangle$ are equal, which implies that for each particle b:

$$\frac{1}{m_b}\mathbf{F}_b^{int} = -\frac{1}{\rho_b}\mathbf{Grad}_b\{p_a\} \tag{1.12}$$

That means that the continuity equation and the momentum equation are variationally consistent.

It is possible to define variants of these two operators conserving this property of adjunction. For more details see Violeau [33].

1.2.2 Viscous forces

The viscous term is of second-order and hence, necessitates treatment of second order spatial derivatives of the kernel. Usually in *SPH*, we avoid the use of such kernel derivatives, because they are really sensitive to the particle disorder and so generate numerical instabilities (see Issa [14]). For this reason, the common used formulae for the discrete Laplacian are obtained by decomposing into a divergence of a gradient. Then, the

divergence is approximated by a kernel derivative whereas the gradient is approximated by a finite differences formula.

The main two models in *SPARTACUS-2D* for computing the viscous term $\frac{1}{\rho}\nabla.\left(\mu\boldsymbol{\nabla}\,\mathbf{u}\right)$ are:

$$\frac{1}{\rho_a}\boldsymbol{\nabla}.\left(\mu\boldsymbol{\nabla}\,\mathbf{u}\right)_a = \sum_{b\,\in\,\mathcal{F}} m_b \frac{\mu_a+\mu_b}{\rho_a\rho_b}\frac{\mathbf{u}_{ab}}{r_{ab}^2}\mathbf{r}_{ab}.\boldsymbol{\nabla}w_{ab} \tag{1.13a}$$

$$\frac{1}{\rho_a}\boldsymbol{\nabla}.\left(\mu\boldsymbol{\nabla}\mathbf{u}\right)_a = 2(n+2)\sum_{b\,\in\,\mathcal{F}} m_b \frac{\mu_a+\mu_b}{\rho_a\rho_b}\frac{\mathbf{u}_{ab}.\mathbf{r}_{ab}}{r_{ab}^2}\boldsymbol{\nabla}w_{ab} \tag{1.13b}$$

where the dynamic viscosity μ is given by:

$$\mu \equiv \nu\rho \tag{1.14}$$

and n is the dimension of the space. The first model (1.13a) is due to Morris *et al.* (see [27]) and the second one (1.13b) to Monaghan (see [23]).

Basically, Monaghan's model is obtained by assuming that $\boldsymbol{\nabla}.\left(\mu\boldsymbol{\nabla}\mathbf{u}^T\right) = 0$ which is true for laminar incompressible flows. A general formula could be derived (see [33] for algebraic details):

$$\frac{1}{\rho_a}\boldsymbol{\nabla}.\left[\mu\left(\boldsymbol{\nabla}\mathbf{u}+\boldsymbol{\nabla}\mathbf{u}^T\right)\right]_a = \sum_{b\,\in\,\mathcal{F}} m_b \frac{\frac{\mu_a+\mu_b}{2}}{\rho_a\rho_b}\left[(n+2)\frac{\mathbf{u}_{ab}.\mathbf{r}_{ab}}{r_{ab}^2}\boldsymbol{\nabla}w_{ab}+\frac{\boldsymbol{\nabla}w_{ab}.\mathbf{r}_{ab}}{r_{ab}^2}\mathbf{u}_{ab}\right] \tag{1.15}$$

Divergence operator of a gradient field

The viscous force of Morris *et al.* can be derived as follows:

$$\frac{1}{\rho_a}\boldsymbol{\nabla}.\left(\mu\boldsymbol{\nabla}\,\mathbf{u}\right)_a = \frac{1}{\rho_a}\mathbf{Div}_a\left(\mu\boldsymbol{\nabla}\,\mathbf{u}\right) \tag{1.16}$$

where for an arbitrary gradient field $\{\boldsymbol{\nabla}\mathbf{A}_b\}$ and a scalar field $\{\mathbf{B}_b\}$:

$$\frac{1}{\rho_a}\mathbf{Div}_a\left(B_b\boldsymbol{\nabla}\mathbf{A}_b\right) = \frac{1}{\rho_a}\sum_{b\,\in\,\mathcal{F}} V_b\left(B_a\boldsymbol{\nabla}\mathbf{A}_a + B_b\boldsymbol{\nabla}\mathbf{A}_b\right).\boldsymbol{\nabla}w_{ab} \tag{1.17}$$

combined with the finite differences approximation:

$$\boldsymbol{\nabla}\mathbf{A}_a.\mathbf{e}_{ab} \simeq \boldsymbol{\nabla}\mathbf{A}_b.\mathbf{e}_{ab} \simeq \frac{\mathbf{A}_{ab}}{r_{ab}} \tag{1.18}$$

1.2.3 Kernels used

Generally speaking, kernels used in the *SPH* formulation depend on a lengthscale h (also called smoothing length), on the dimension of the position vector ($n=2$ or $n=3$) and on the norm of the position vector $r=|\mathbf{r}|$ and can be written as:

$$w\left(r\right) = \frac{\alpha_{f,n}}{h^n}f(q) \tag{1.19}$$

where q is given by

$$q \equiv \frac{r}{h} \tag{1.20}$$

and $\alpha_{f,n}$ is a normalisation factor to ensure that the integral of the kernel on its support is 1, *ie*:

$$\int_{\Omega_0} w\left(r\right)\mathrm{d}\mathbf{r} = 1 \tag{1.21}$$

The kernels used in the present work are:

1. The spline based kernel of order 4 defined by:

$$f(q) = \begin{cases} \left(\frac{5}{2}-q\right)^4 - 5\left(\frac{3}{2}-q\right)^4 + 10\left(\frac{1}{2}-q\right)^4 & \text{when} \quad 0 \le q < \frac{1}{2} \\ \left(\frac{5}{2}-q\right)^4 - 5\left(\frac{3}{2}-q\right)^4 & \text{when} \quad \frac{1}{2} \le q < \frac{3}{2} \\ \left(\frac{5}{2}-q\right)^4 & \text{when} \quad \frac{3}{2} \le q < \frac{5}{2} \\ 0 & \text{when} \quad \frac{5}{2} \le q \end{cases} \tag{1.22}$$

with

$$\begin{aligned} \alpha_{f,2} &= \frac{96}{1199\pi} \\ \alpha_{f,3} &= \frac{1}{20\pi} \end{aligned} \tag{1.23}$$

2. The quintic kernel (Wendland [36]) defined by:

$$f(q) = \begin{cases} \left(1-\frac{q}{2}\right)^4 (2q+1) & \text{when} \quad 0 \le q < 2 \\ 0 & \text{when} \quad 2 \le q \end{cases} \tag{1.24}$$

with

$$\begin{aligned} \alpha_{f,2} &= \frac{7}{4\pi} \\ \alpha_{f,3} &= \frac{21}{16\pi} \end{aligned} \tag{1.25}$$

The Fourier transformation of the latter is:

$$\begin{aligned} \widehat{f}(k) &= \int_0^{+\infty} f(q)\cos(kq)\mathrm{d}q \\ &= \frac{15\left[2k^2 - 2 + k\sin(2k) + 2\cos(2k)\right]}{2k^6} \end{aligned} \tag{1.26}$$

which is positive decreasing. This property is useful regarding the stability of the system of particles, for more information see [33].

1.3 Existing methods for wall modelling

Many ways of implementing solid walls in *SPH* have been developed over the past decades. Among the most popular and commonly used, we can cite:

(*i*) Lennard-Jones repulsive forces proposed by Monaghan [24],

(*ii*) fictitious particles (or also ghost particles) which consist in filling the empty area of the kernel support behind a wall with particles and giving them well chosen physical quantities (such as pressure and velocity) to enforce no slip or free slip condition for example,

(*iii*) semi-analytical boundary conditions based on a variational formulation introduced by Kulasegaram *et al.* [15] where a wall renormalization of the equations is made with respect to the missing area of the kernel support. We will describe a variant of this method in Chapter 2.

All of these have advantages and drawbacks. The Lennard-Jones potential force (*i*) originally describes the interaction between pairs of atoms and is used to model the repulsion between a fluid particle and a boundary particle (see Figure 1.2(a)). This method is then easy to implement, even for complex geometries and computationally cheap. However, it leads to spurious behaviour: for instance it is impossible to maintain particles fixed along a vertical wall in the presence of gravity.

The fictitious particles (*ii*) (recommended option in *SPARTACUS-2D*) prevent such a non-physical behaviour (see Figure 1.2(b)). However, the positioning of ghost particles in complex geometries can be really awkward, particularly in $3D$. Moreover, the computational effort required is not negligible, given that we increase the number of particles to take into account in the discrete summations (1.1) and (1.3).

Finally, the semi-analytical approach (*iii*) is attractive thanks to its variational formulation. That means that some physical quantities such as momentum will be automatically conserved. Unfortunately, the original attempt did not present a clear and simple way to compute renormalization terms. Furthermore, the formulation proposed in [15] was not able to reproduce hydrostatic pressure field or to take into account the shear stress along a wall. That is why this methodology needs to be modified, particularly if we want to focus on turbulence.

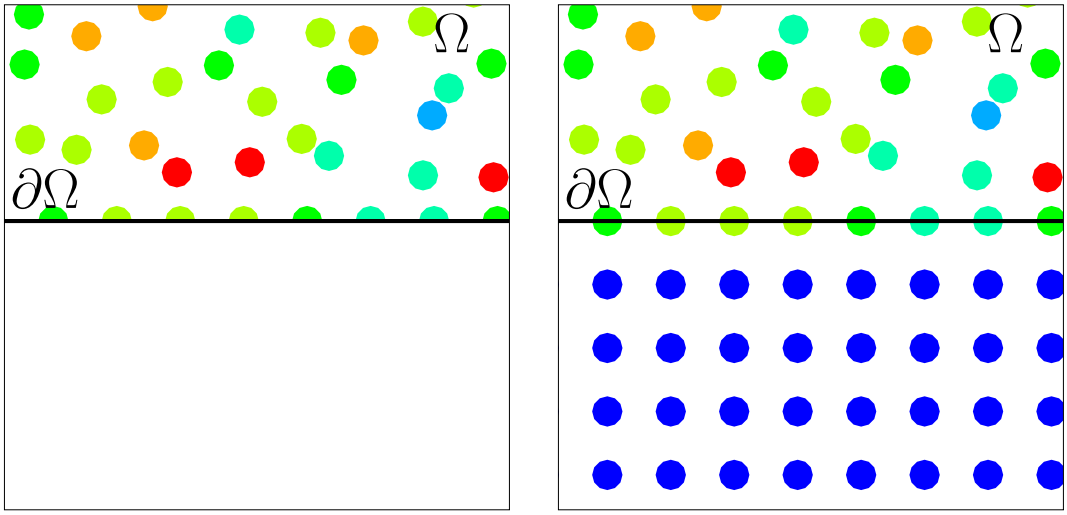

(a) Sketch of the Lennard-Jones repulsive forces: only edge particles are placed on the boundary $\partial\Omega$

(b) Sketch of the fictitious particles (in blue) used to complete the kernel area support for fluid particles on the "solid" side of the wall.

Figure 1.2: Sketch of two existing methods to model a wall: repulsive forces and fictitious particles.

Chapter 2

New boundary conditions and accurate time stepping

Treating wall boundary conditions is one of the most challenging parts of the *SPH* method and many different approaches have been developed by authors including Kulasegaram *et al.* [15], Oger *et al.* [28], Di Monaco *et al.* [8], Monaghan and Kajtar [22], Marongiu *et al.* [19] and De Leffe *et al.* [7]. Accurate boundary conditions are essential since in many applications the target values are precise loading on walls (forces on floating bodies or shoreline structures, tank walls, wind-wave exchanges, fluid-structure interactions in power-plants etc.), and is an obvious prerequisite of the current research project also aiming at improving turbulence modelling near walls.

The present work is based on Kulasegaram *et al.* [15] which consists of renormalizing the density field near a solid wall with respect to the missing kernel support area. This methodology, combined with the Lagrangian formalism, defines intrinsic *gradient* and *divergence* operators which are variationally consistent and ensure conservation properties.

The time integration scheme used for the continuity equation requires particular attention, and as already mentioned by Vila [32], we prove there is no point in using a dependence in time of the particles' density if no kernel gradient corrections are added. Thus, by using a near-boundary kernel-corrected version of the time integration scheme proposed by Vila, we are able to simulate long-time simulations ideally suited for turbulent channel flow with accurate boundary conditions.

As mentioned by De Leffe *et al.* [7], the method of Kulasegaram *et al.* defines an inaccurate gradient operator which provides non-consistent behaviour. Herein we introduce corrections of differential operators analogous to Di Monaco *et al.* [8] and De Leffe *et al.* [7] for slightly compressible viscous Newtonian flows, but all boundary terms issued from the continuous approximation are given by surface summations which only use information from a mesh file of the boundary.

In order to compute the kernel correction, Feldman and Bonet [9] use an analytical value which is computationally expensive whereas Kulasegaram *et al.* [15] and De Leffe *et al.* [7] use polynomial approximations which can be difficult to define for complex geometries. We propose here to compute the renormalization term of the kernel support near a solid with a time integration scheme, thereby more easily accounting for any shape of boundary.

All the present developments have been numerically tested using *SPARTACUS2D*, a *FORTRAN* code initially developed by *EDF R&D*.

2.1 Conservative systems: correction of the continuity and of momentum equations

2.1.1 Kulasegaram *et al.*'s renormalisation

Instead of assuming that $\rho_a \simeq \sum_{b \in \mathcal{F}} m_b w_{ab}$, which underestimates ρ_a when the particle a is close to a boundary (see Figure 2.1), we renormalise that estimation:

$$\rho_a \simeq \frac{1}{\gamma_a} \sum_{b \in \mathcal{F}} m_b w_{ab} \tag{2.1}$$

where γ_a is defined by:

$$\gamma_a \equiv \int_{\Omega \cap \Omega_a} w\left(\mathbf{r} - \mathbf{r}_a\right) \mathrm{d}\mathbf{r} \tag{2.2}$$

We recall that Ω is the studied fluid domain.

We can notice that far from a solid boundary $\gamma_a = 1$. Given the definition (2.2) we have chosen, γ_a is an Eulerian field depending only on the position of the particle a with respect to boundaries of Ω. Other authors such as Shepard [31] and Dalrymple and Rogers [5] use a renormalization term based on the fluid particles, which is not our choice here. However we will see that this correction is unable to correct the behaviour near the free-surface, that is why we have used an adaptation of the Shepard filter for flows with a free-surface (see §2.2 for more details).

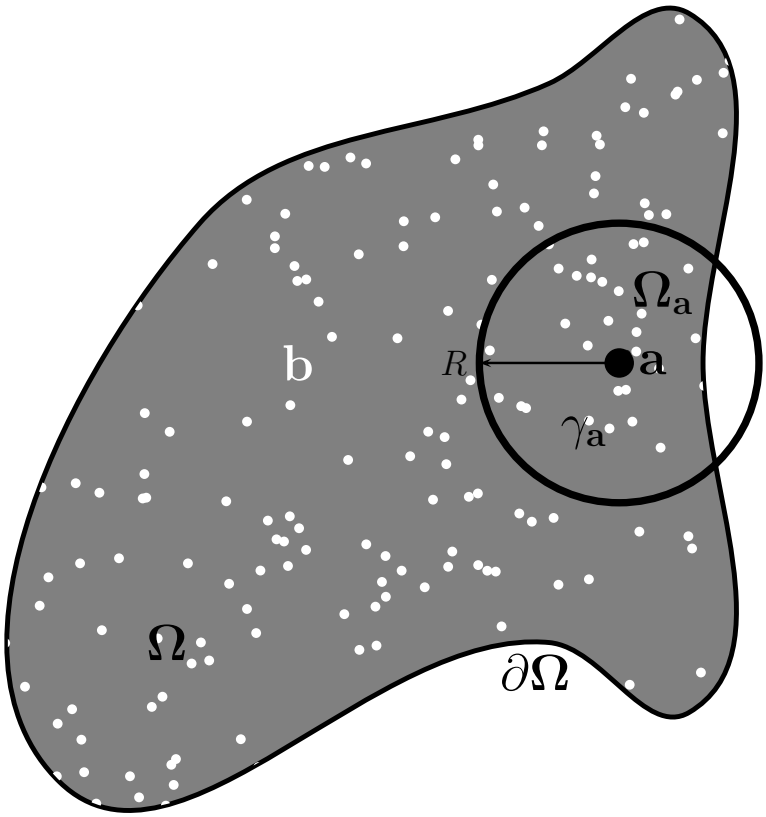

Figure 2.1: Kernel-boundary interaction.

Then the new continuity equation is rewritten by deriving (2.1) :

$$\frac{\mathrm{d}\rho_a}{\mathrm{d}t} = \frac{1}{\gamma_a}\sum_{b\,\in\,\mathcal{F}} m_b \boldsymbol{\nabla} w_{ab}.\mathbf{u}_{ab} - \frac{\rho_a}{\gamma_a}\boldsymbol{\nabla}\gamma_a.\mathbf{u}_a \tag{2.3}$$

to be compared with (1.1).

$\boldsymbol{\nabla}\gamma_a$ is defined by:

$$\boldsymbol{\nabla}\gamma_a \equiv \int_{\Omega\cap\Omega_a} \boldsymbol{\nabla}_a w\left(\mathbf{r}-\mathbf{r}_a\right)\mathrm{d}\mathbf{r} \tag{2.4}$$

Since we are working with kernels with compact supports, we can transform the volume integral into a surface integral using the Gauss theorem:

$$\boldsymbol{\nabla}\gamma_a \quad = \quad \int_{\partial\Omega\cap\Omega_a} w\left(\mathbf{r}-\mathbf{r}_a\right)\mathbf{n}\mathrm{d}S \tag{2.5}$$

where $\mathbf{n}$ is the inward boundary normal.

In order to evaluate the new internal forces and contact forces, Kulasegaram *et al.* [15] derive the internal energy (see Appendix A.2) and obtain:

$$\begin{aligned}
\mathbf{F}_a^{int} &= \mathbf{F}_a^p + \mathbf{F}_a^B \\
\mathbf{F}_a^p &\equiv -m_a\sum_{b\,\in\,\mathcal{F}} m_b\left(\frac{p_a}{\gamma_a\rho_a^2}+\frac{p_b}{\gamma_b\rho_b^2}\right)\boldsymbol{\nabla} w_{ab} \\
\mathbf{F}_a^B &\equiv m_a\frac{p_a}{\gamma_a\rho_a}\boldsymbol{\nabla}\gamma_a
\end{aligned} \tag{2.6}$$

where $\mathbf{F}_a^p$ is the renormalised internal force due to the pressure and $\mathbf{F}_a^B$ is a repulsive force due to the boundary.

Remark about operators

The correction of Kulasegaram *et al.* can be expressed in terms of new compatible (in a variational sense) gradient and divergence operators. Indeed, one can define:

$$\begin{aligned}
\widetilde{\mathbf{Grad}}_a\{A_b\} &\equiv \rho_a\sum_{b\,\in\,\mathcal{F}} m_b\left(\frac{A_a}{\gamma_a\rho_a^2}+\frac{A_b}{\gamma_b\rho_b^2}\right)\boldsymbol{\nabla} w_{ab} - \frac{A_a}{\gamma_a}\boldsymbol{\nabla}\gamma_a \\
\widetilde{\mathrm{Div}}_a\{\mathbf{A}_b\} &\equiv -\frac{1}{\gamma_a\rho_a}\sum_{b\,\in\,\mathcal{F}} m_b\mathbf{A}_{ab}.\boldsymbol{\nabla} w_{ab} + \frac{1}{\gamma_a}\mathbf{A}_a.\boldsymbol{\nabla}\gamma_a
\end{aligned} \tag{2.7}$$

Thus the operators (2.7) verify the property (1.9) (see Appendix A.3) and the variational calculus (1.11a) holds, thus proving the consistency between the momentum equation and the continuity equation.

2.1.2 Correction of the operators to account for boundary conditions

General shape of the boundary

We approximate the shape of the boundary $\partial\Omega$ of the domain Ω with straight segments in $2D$ denoted by the subscript $(.)_s$ which have a normal $\mathbf{n}_s$ and a surface area S_s (see Figure 2.3). The set containing all the segments is denoted by $\mathcal{S}$. Each segment is defined by two edge points denoted by the subscript $(.)_{e1}$ and $(.)_{e2}$ which have an initial volume V_e given by $V_e = \frac{m_e}{\rho_0}$. The initial volume of edge particles is a fraction of the initial volume of fluid particles V_f. For instance, for a plane $V_e = \frac{1}{2}V_f$. More generally, for an edge particle on a wedge with an angle θ displayed on the Figure 2.2, $V_e = \frac{\theta}{2\pi}V_f$. In $3D$ this volume would use the solid angle of the wedge.

The set containing all the edge particles is denoted by $\mathcal{E}$. These edge particles (also called semi particles in this report) are of particular interest for recording the pressure field at the solid boundary (and hence for fluid and structure coupling for example). They are also useful to improve accuracy of the continuity equation, as

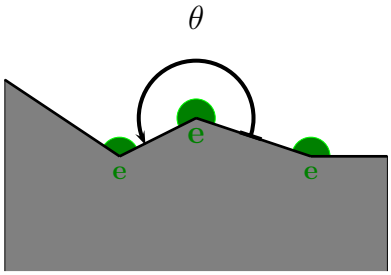

Figure 2.2: Sketch of the volume of an edge particle.

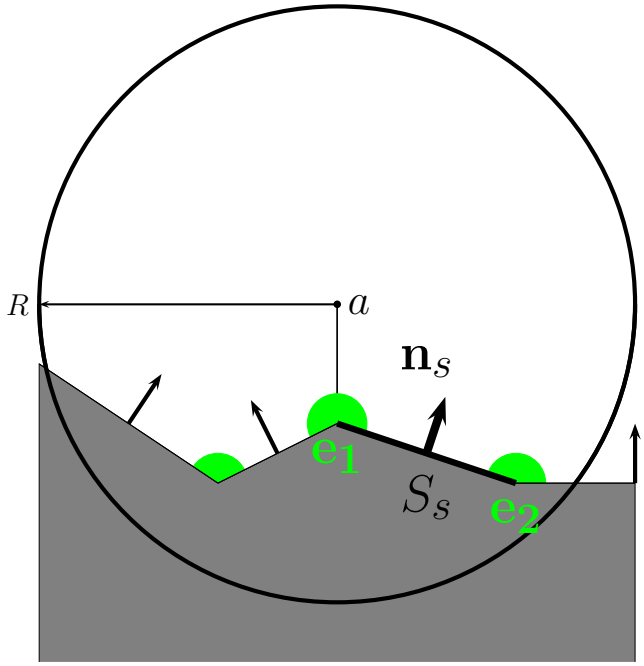

Figure 2.3: Sketch of the shape of the boundary with edge *semi* particles e (in green) and with segments s which have a surface S_s and an inward normal $\mathbf{n}_s$.

they mimic a wet wall. It is important to notice that they are taken into account in the continuity equation and in the momentum equation (*i.e.* $\mathcal{E} \subset \mathcal{F}$), even if they are Eulerian particles, that is to say they are fixed if the wall is motionless and does not depend on the momentum equation.

Next we define the contribution of the segment s in the value of $\boldsymbol{\nabla}\gamma_a$ to be:

$$\boldsymbol{\nabla}\gamma_{as} \equiv \left(\int_{\mathbf{r}_{e1}}^{\mathbf{r}_{e2}} w\left(r\right) \mathrm{d}l \right) \mathbf{n}_s \tag{2.8}$$

and then $\boldsymbol{\nabla}\gamma_a$ can be decomposed in:

$$\boldsymbol{\nabla}\gamma_a = \sum_{s \,\in\, \mathcal{S}} \boldsymbol{\nabla}\gamma_{as} \tag{2.9}$$

The description of the boundary geometry can be extended to $3D$ by substituting the segments by triangles.

Approach of De Leffe *et al.*

The main disadvantage of the Kulasegaram's method is that the *gradient* operator defined by (2.7) is not accurate near a boundary or the free-surface. Indeed, we can see that *gradients* of constants are non zero: if we simulate uniform overpressure in a periodic pipe without any body force, the *gradient* (2.7) of the pressure is not zero everywhere and particles rearrange themselves (see Figure 2.4(a)). To correct that, as did De Leffe [7], we can go back to the continuous interpolation of an arbitrary integrable function f at a point $\mathbf{r}$:

$$\left\langle f \right\rangle \left(\mathbf{r}\right) \;=\; \frac{1}{\gamma\left(\mathbf{r}\right)} \int_{\Omega \cap \Omega_r} f\left(\mathbf{r}'\right) w\left(\tilde{r}\right) \mathrm{d}\mathbf{r}' \tag{2.10}$$

where $\tilde{r} \equiv |\mathbf{r} - \mathbf{r}'|$ and Ω_r is the kernel support centred in $\mathbf{r}$. By interpolating the gradient of the function f in the same way, it becomes:

$$\begin{aligned} \left\langle \boldsymbol{\nabla} f \right\rangle \left(\mathbf{r}\right) \;=\; & -\frac{1}{\gamma\left(\mathbf{r}\right)} \int_{\Omega \cap \Omega_r} f\left(\mathbf{r}'\right) \boldsymbol{\nabla} w\left(\tilde{r}\right) \mathrm{d}\mathbf{r}' \\ & -\frac{1}{\gamma\left(\mathbf{r}\right)} \int_{\partial\Omega \cap \Omega_r} f\left(\mathbf{r}'\right) w\left(\tilde{r}\right) \mathbf{n} \mathrm{d}\mathbf{r}' \end{aligned} \tag{2.11}$$

where the right-hand-side is obtained by an integration by parts and $\mathbf{n}$ is here the inward normal. So we can see that the boundary conditions appear naturally through the second integral of (2.11).

Moreover, if we consider that the gradient defined by (1.7) is a discrete approximation of the continuous gradient $\boldsymbol{\nabla} f \equiv \rho \boldsymbol{\nabla} \frac{f}{\rho} + \frac{f}{\rho} \boldsymbol{\nabla} \rho$, we obtain:

$$\begin{aligned} \left\langle \boldsymbol{\nabla} f \right\rangle \left(\mathbf{r}\right) \;&=\; \left\langle \rho \boldsymbol{\nabla} \frac{f}{\rho} + \frac{f}{\rho} \boldsymbol{\nabla} \rho \right\rangle \left(\mathbf{r}\right) \\ &=\; -\frac{1}{\gamma\left(\mathbf{r}\right)} \int_{\Omega \cap \Omega_r} \left[\frac{f}{\rho}\left(\mathbf{r}'\right) \rho\left(\mathbf{r}\right) + \frac{f}{\rho}\left(\mathbf{r}\right) \rho\left(\mathbf{r}'\right) \right] \boldsymbol{\nabla} w\left(\tilde{r}\right) \mathrm{d}\mathbf{r}' \\ &\quad -\frac{1}{\gamma\left(\mathbf{r}\right)} \int_{\partial\Omega \cap \Omega_r} \left[\frac{f}{\rho}\left(\mathbf{r}'\right) \rho\left(\mathbf{r}\right) + \frac{f}{\rho}\left(\mathbf{r}\right) \rho\left(\mathbf{r}'\right) \right] w\left(\tilde{r}\right) \mathbf{n} \mathrm{d}\mathbf{r}' \end{aligned} \tag{2.12}$$

Once again the boundary conditions appear naturally, and we can now set the following discrete operator *gradient* for an arbitrary field $\{A_b\}$ as:

$$\widetilde{\mathbf{Grad}}_a\{A_b\} \;\equiv\; \frac{\rho_a}{\gamma_a} \sum_{b \,\in\, \mathcal{F}} m_b \left(\frac{A_a}{\rho_a^2} + \frac{A_b}{\rho_b^2} \right) \boldsymbol{\nabla} w_{ab} - \frac{\rho_a}{\gamma_a} \sum_{s \,\in\, \mathcal{S}} \left(\frac{A_a}{\rho_a^2} + \frac{A_s}{\rho_s^2} \right) \rho_s \boldsymbol{\nabla} \gamma_{as} \tag{2.13}$$

where $\boldsymbol{\nabla}\gamma_{as}$ can be approximated by $\boldsymbol{\nabla}\gamma_{as} \simeq w_{as} S_s \mathbf{n}_s$ or computed analytically (see §2.3 for more details). The method to compute ρ_s and A_s will be investigated in the next paragraph on dynamic boundary conditions. The discrete gradient (2.13) has to be compared with the Kulasegaram *et al.*'s one defined by (2.7). We can notice that the two operators differ only next to a boundary.

If we assume that the fields $\{A_b\}$ and $\{\rho_b\}$ are such that $\frac{\partial A}{\partial n}=0$ and $\frac{\partial \rho}{\partial n}=0$ (and hence, at the first order $A_s=A_a$ and $\rho_s=\rho_a$) then the *gradient* operator can be rewritten as:

$$\widetilde{\mathbf{Grad}}_a\{A_b\} \simeq \frac{\rho_a}{\gamma_a}\sum_{b\in\mathcal{F}} m_b\left(\frac{A_a}{\rho_a^2}+\frac{A_b}{\rho_b^2}\right)\boldsymbol{\nabla} w_{ab} - 2\frac{A_a}{\gamma_a}\boldsymbol{\nabla}\gamma_a \tag{2.14}$$

The previous form shows why the discrete operator defined by Kulasegaram *et al.* is not accurate for a uniform field next to a boundary, since the boundary term should have a factor 2 for instance.

We may notice that the variational consistency of the operators *gradient* and *divergence* are not *a priori* fulfilled.

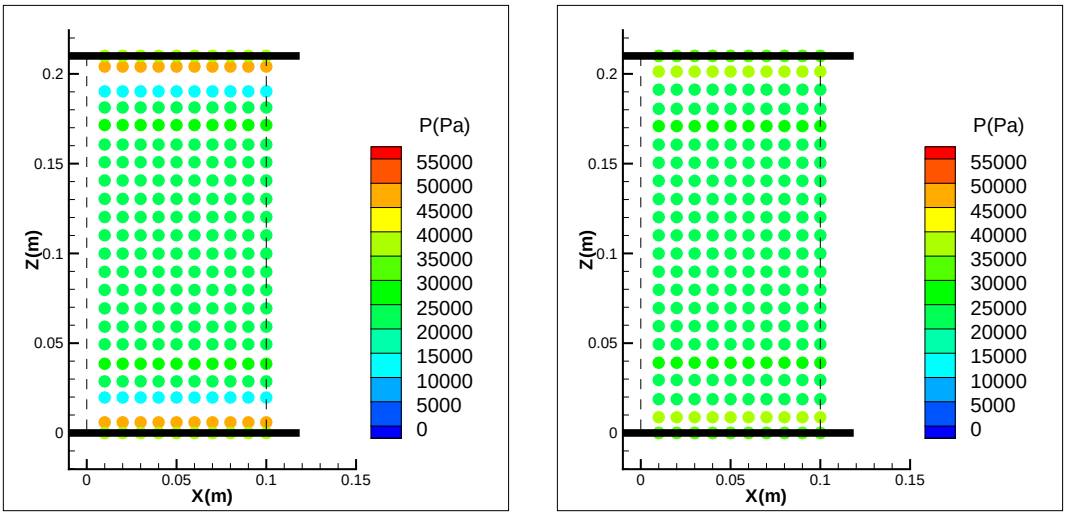

(a) Kulasegaram *et al.*'s *gradient* operator (2.7) is unable to maintain uniform pressure field. Particles move to an non-physical equilibrium.

(b) The present *gradient* operator (2.13) is able to almost maintain uniform pressure field as an equilibrium.

Figure 2.4: Comparison of gradient operators (2.7) and (2.13) in an over-pressurized periodic pipe.

Dynamic boundary conditions

The *gradient* operator (2.13) applied to the pressure field gives:

$$\widetilde{\mathbf{Grad}}_a\{p_b\} \equiv \frac{\rho_a}{\gamma_a}\sum_{b\in\mathcal{F}} m_b\left(\frac{p_a}{\rho_a^2}+\frac{p_b}{\rho_b^2}\right)\boldsymbol{\nabla} w_{ab} - \frac{\rho_a}{\gamma_a}\sum_{s\in\mathcal{S}}\left(\frac{p_a}{\rho_a^2}+\frac{p_s}{\rho_s^2}\right)\rho_s\boldsymbol{\nabla}\gamma_{as} \tag{2.15}$$

Hence, we are left to compute the pressure p_s and the density ρ_s at the wall. A robust way of doing this is to deduce these values from a dynamic condition such that $\frac{\partial \rho}{\partial n}=0$. We can notice that the condition $\frac{\partial \rho}{\partial n}=0$ is consistent with the renormalization done with the equation (2.1). This condition implies to first order $\rho_s=\rho_a$. In the presence of gravity and motion the analogous condition on the pressure field is written as:

$$\frac{\partial}{\partial n}\left(\frac{p^\star}{\rho}+\frac{u^2}{2}\right) = 0 \tag{2.16}$$

where $p^\star \equiv p-\rho\mathbf{g}.\mathbf{r}$ and u is the magnitude of the velocity (see [33] for further details).

Hence we can replace ρ_s and $\frac{p_s}{\rho_s}$ in (2.15) by:

$$\begin{aligned}\rho_s &= \rho_a \\ \frac{p_s}{\rho_s} &= \frac{p_a}{\rho_a} - \mathbf{g}.\mathbf{r}_{as} + \frac{u_a^2-u_s^2}{2}\end{aligned} \tag{2.17}$$

The main advantage of this approach is that for a fluid particle a interacting with the boundary, the pressure of the wall is defined only with quantities of the particle a itself, and then is well defined even if the particle a is alone.

The main disadvantage of that method is the lack of accuracy, especially for confined flows. Indeed, if we consider a periodic channel flow, a small variation of the density in the stream-wise direction will lead to a variation of the repulsive forces in the same direction, and then cause particles to oscillate next to the boundary and diffuse too much of momentum, however the results are not shown in the present report.

Another way to compute the pressure and the density at the wall is to use an *SPH* interpolation for the edge particles in $\mathcal{E}$ in the same way as previously, but the choice made is to average in space to give a wall value:

$$\begin{aligned} \rho_e &= \frac{1}{\alpha_e} \sum_{b \in \mathcal{F} \setminus \mathcal{E}} V_b \rho_b w_{be} \\ \frac{p_e}{\rho_e} &= \frac{1}{\alpha_e} \sum_{b \in \mathcal{F} \setminus \mathcal{E}} V_b \left(\frac{p_b}{\rho_b} - \mathbf{g}.\mathbf{r}_{be} + \frac{u_b^2 - u_e^2}{2} \right) \end{aligned} \tag{2.18}$$

where the set $\mathcal{F} \setminus \mathcal{E}$ denotes all fluid particles $\mathcal{F}$, particles in $\mathcal{E}$ excepted and where α_e is defined by:

$$\alpha_e \equiv \sum_{b \in \mathcal{F} \setminus \mathcal{E}} V_b w_{be} \tag{2.19}$$

Further description of the Shepard filter α_e is given in §2.2 (see Equation 2.34)).

Here, we should notice that the interpolation done is based on fluid particles in $\mathcal{F}$ which do not belong to the set of edge particles $\mathcal{E}$. Then we define the density and the pressure at the wall elements s to be:

$$\begin{aligned} \rho_s &= \frac{\rho_{e1} + \rho_{e2}}{2} \\ \frac{p_s}{\rho_s} &= \frac{p_{e1}/\rho_{e1} + p_{e2}/\rho_{e2}}{2} \end{aligned} \tag{2.20}$$

where the edge particles $e1$ and $e2$ are defined in §2.1.2. This strategy to evaluate quantities at the wall will be reused to compute the wall shear stress in §2.4 and also the wall value of a scalar transported by the flow in §2.5.3.

2.2 Conservation issues: time integration for the continuity equation

Let us focus on the temporal scheme used in the version 1.2 *SPARTACUS-2D*:

$$\left\{ \begin{array}{lcl} \mathbf{u}_a^{n+1} &=& \mathbf{u}_a^n - \dfrac{\delta t}{\rho_a^n} \mathbf{Grad}_a^n \{p_b^n\} + \mathbf{g} \\ \mathbf{r}_a^{n+1} &=& \mathbf{r}_a^n + \delta t \mathbf{u}_a^{n+1} \\ \rho_a^{n+1} &=& \rho_a^n + \delta t \displaystyle\sum_{b \in \mathcal{F}} m_b \boldsymbol{\nabla}^n w_{ab}.\mathbf{u}_{ab}^{n+1} \end{array} \right. \tag{2.21}$$

where the superscript $(.)^n$ refers to the time step n and to the time $t = \displaystyle\sum_{i=1}^{n} \delta t$ (with have to bear in mind that δt can vary between two time steps).

We can see that the velocities are explicit, whereas the positions are implicit. In the continuity equation, positions are explicit whereas the velocities are implicit; for this reason we do not write the *r.h.s.* of Equation (2.21) as $\rho_a \mathrm{Div}\{\mathbf{u}_b\}$. This time integration scheme is called semi-implicit and is symplectic (that is to say reversible in time, for more information see [21]).

A first attempt to integrate in time the continuity equation

To adapt the previous time integration scheme to the method of Kulasegaram *et al.* and the present modified one, naturally we can try the following scheme:

$$\left\{\begin{array}{rcl} \mathbf{u}_a^{n+1} & = & \mathbf{u}_a^n - \dfrac{\delta t}{\rho_a^n}\widetilde{\mathbf{Grad}}_a^n\{p_b^n\} + \mathbf{g} \\ \mathbf{r}_a^{n+1} & = & \mathbf{r}_a^n + \delta t \mathbf{u}_a^{n+1} \\ \rho_a^{n+1} & = & \rho_a^n + \dfrac{\delta t}{\gamma_a^n}\left[\displaystyle\sum_{b\in\mathcal{F}} m_b \boldsymbol{\nabla}^n w_{ab}.\mathbf{u}_{ab}^{n+1} - \rho_a^n \boldsymbol{\nabla}^n \gamma_a.\mathbf{u}_a^{n+1}\right] \end{array}\right. \tag{2.22}$$

where the operator $\widetilde{\mathbf{Grad}}_a$ is either (2.7) or (2.13).

On the one hand, this approach seems to give satisfactory results in the sense that the basin in a dam break case is kept impermeable with a relatively small time step (see later in Figure 2.9).

On the other hand, we can notice that when we run long-time simulations in a channel with a relatively large time step, particles near the wall are slowly moving down and end up passing through the wall as we see in Figure 2.5(a) (note, we can set a relatively big time step by increasing the numerical speed of sound c_0).

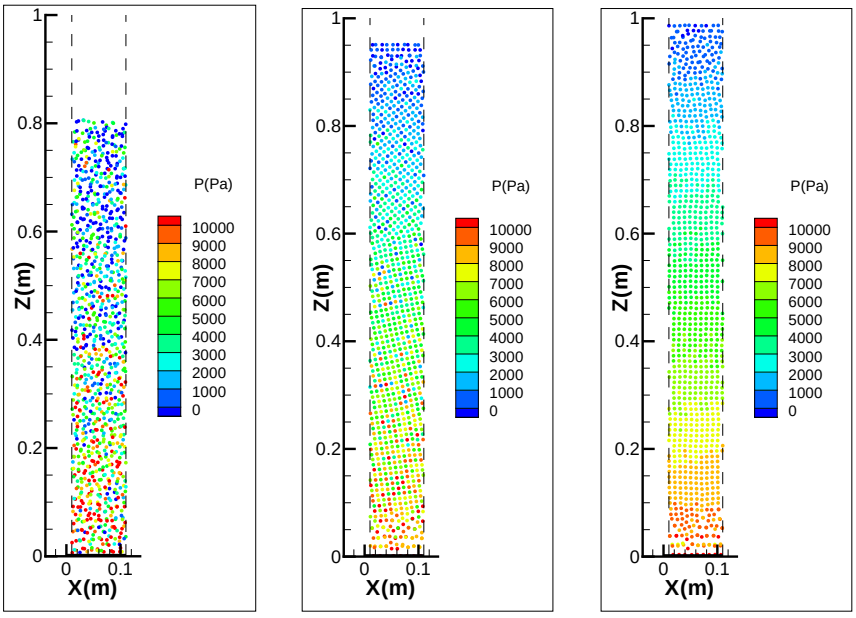

(a) Previous time scheme (2.22) with $c_0 = 20m.s^{-1}$.

(b) Previous time scheme (2.22) with $c_0 = 100m.s^{-1}$.

(c) New time scheme (2.26) with $c_0 = 20m.s^{-1}$.

Figure 2.5: Comparison of the pressure field and the water depth in a periodic open channel flowing from left to right for two different time schemes after the same physical time.

This is evidence that the time integration scheme (2.22) is responsible for density decrease.

The problem is caused by the continuity equation: when particles near the boundary are oscillating, *ie* moving back and forth (*e.g.* during an initialization phase, or it can be produced by the space discretization of the wall which can mimic a roughness), their densities decrease, and then the pressure, related to the density by the equation of state, becomes insufficient to create a repulsive force to balance the other forces.

The origin of this phenomenon is the term $\frac{\delta t}{\gamma_a^n}\rho_a^n \boldsymbol{\nabla}^n \gamma_a.\mathbf{u}_a^{n+1}$ in the time discretized continuity equation (2.22). Indeed, if we consider a single particle moving towards the wall between the times t_n and t_{n+1} (from

the distance z_n to z_{n+1}), the exact variation of the density from Equation (2.3) reads:

$$\rho_a^{n+1} - \rho_a^n = \int_n^{n+1} \mathrm{d}\rho_a = -\int_n^{n+1} \frac{\rho_a}{\gamma_a} \boldsymbol{\nabla}\gamma_a . \mathrm{d}\mathbf{r}_a \tag{2.23}$$

whereas the discrete variation is:

$$\rho_a^{n+1} - \rho_a^n = \int_n^{n+1} \mathrm{d}\rho_a = -\left(\frac{\rho_a}{\gamma_a} \boldsymbol{\nabla}\gamma_a\right)^n . \left(\mathbf{r}_a^{n+1} - \mathbf{r}_a^n\right) \tag{2.24}$$

Then, if we let the particle return back to its initial position between the times t_{n+1} and t_{n+2} (from the distance z_{n+1} to the distance $z_{n+2} = z_n$), then it is clear from Figure 2.6 that we have lost the amount of density in the zebra area of density: the exact variation of the density of the total transformation between t^n and t^{n+2} is zero whereas the discrete one is always strictly negative.

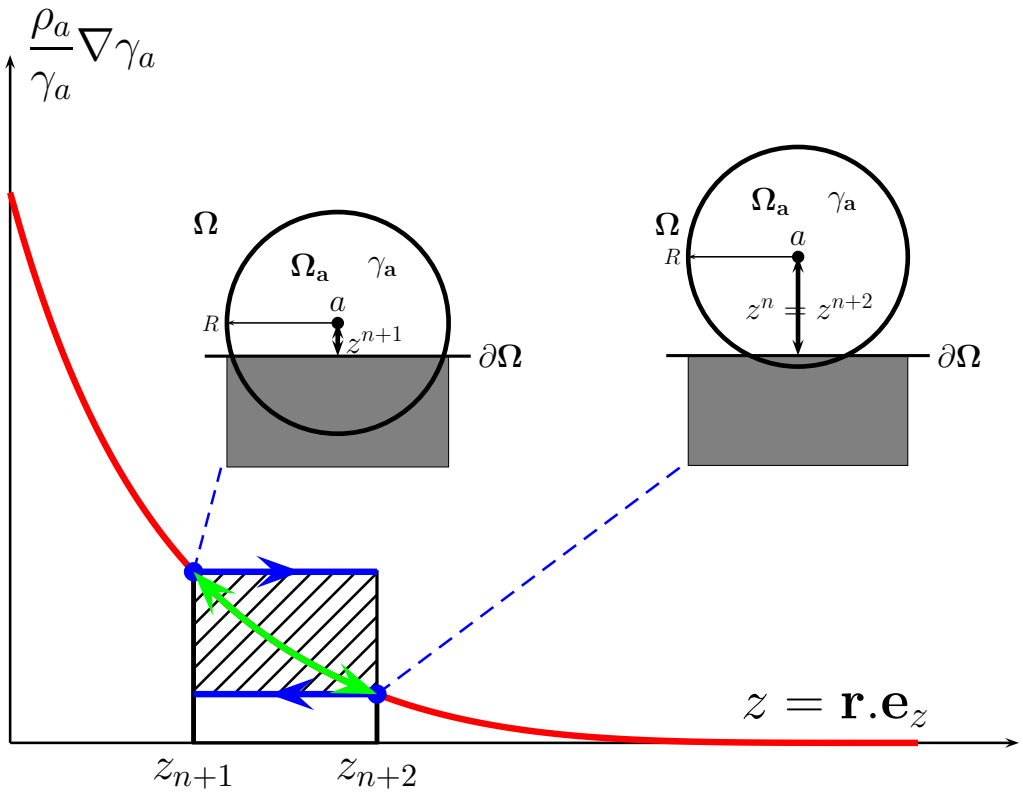

Figure 2.6: Error made by time integration of the continuity equation between t^n and t^{n+2}.

This systematic error of the time discretization of the continuity equation is hazardous because the density should depend only on the particles' positions (here, there is only one particle).

Many other integration time schemes can be considered, such as a leap-frog time scheme, which would reduce the errors in the integration of the continuity equation. The choice made in the present work is to go back to an equation which gives the density explicitly as a function of the positions. This is a more robust approach, especially if there is a wall repulsive force function of the pressure field (and hence of the density field in compressible flows).

A completely position-dependent way to compute the density

If we go back to the main idea of Kulasegaram *et al.* [15], we can see that the corrected continuity equation comes from:

$$\begin{array}{rcl} \dfrac{\mathrm{d}\left(\gamma_a\rho_a\right)}{\mathrm{d}t} & = & \dfrac{\mathrm{d}}{\mathrm{d}t}\left(\displaystyle\sum_{b\,\in\,\mathcal{F}} m_b w_{ab}\right) \\ \| & & \| \\ \gamma_a\dfrac{\mathrm{d}\rho_a}{\mathrm{d}t} + \rho_a\dfrac{\mathrm{d}\gamma_a}{\mathrm{d}t} & = & \displaystyle\sum_{b\,\in\,\mathcal{F}} m_b \boldsymbol{\nabla} w_{ab}.\mathbf{u}_{ab} \end{array} \tag{2.25}$$

Vila [32] already mentioned that the continuity equation (1.1) is strictly equivalent to $\dfrac{\mathrm{d}\rho_a}{\mathrm{d}t} = \dfrac{\mathrm{d}}{\mathrm{d}t}\left(\displaystyle\sum_{b\,\in\,\mathcal{F}} m_b w_{ab}\right)$ if time is considered a continuous variable. Equation (2.25) gives us a way to integrate exactly in time the quantity $\gamma_a\rho_a$ if the particles' positions move from $\{\mathbf{r}_b^n\}$ to $\{\mathbf{r}_b^{n+1}\}$. This prevents systematic time integration errors, and makes ρ_a^n depend only on the positions of particles at the same time (this property, together with simplectic time-stepping, ensure the conservation of a certain energy, see [12] for details).

This leads to the following time integration scheme:

$$\begin{cases} \mathbf{u}_a^{n+1} = \mathbf{u}_a^n - \dfrac{\delta t}{\rho_a^n}\widetilde{\mathbf{Grad}}_a^{\,n}\{p_b^n\} + \mathbf{g} \\ \mathbf{r}_a^{n+1} = \mathbf{r}_a^n + \delta t\mathbf{u}_a^{n+1} \\ \left(\gamma_a\rho_a\right)^{n+1} = \left(\gamma_a\rho_a\right)^n + \displaystyle\sum_{b\,\in\,\mathcal{F}} m_b\left(w_{ab}^{n+1} - w_{ab}^n\right) \end{cases} \tag{2.26}$$

To validate the proposed scheme, we can compare in Figure 2.5 the result we obtain by reducing the time-discretization (and hence the systematic error in the density equation) in the time scheme (2.22) with the result we obtain with the time-scheme (2.26) with a larger time step[1]. By doing so, we have forced the scheme (2.22) to be stable and to converge but it is clear that we have lost density during the stabilisation time: the water depth has decreased (see 2.5(b)) whereas it is not the case on the Figure 2.5(c) with the new scheme. A wider description of this test case is presented in §3.1.1.

More accurate time scheme: Finally, we can build a second-order scheme (Störmer-Verlet scheme, see Monaghan [26]), which can here be written as (keeping the idea that the quantity $\gamma_a\rho_a$ should be exactly conserved):

This leads to the following time integration scheme:

$$\begin{cases} \mathbf{r}_a^{n+\frac{1}{2}} & = & \mathbf{r}_a^n + \dfrac{1}{2}\delta t\mathbf{u}_a^n \\ \gamma_a^{\,n+\frac{1}{2}}\rho_a^{n+\frac{1}{2}} & = & \gamma_a^{\,n-\frac{1}{2}}\rho_a^{n-\frac{1}{2}} + \displaystyle\sum_{b\,\in\,\mathcal{F}} m_b\left(w_{ab}^{n+\frac{1}{2}} - w_{ab}^{n-\frac{1}{2}}\right) \\ \mathbf{u}_a^{n+1} & = & \mathbf{u}_a^n - \dfrac{\delta t}{\rho_a^{n+\frac{1}{2}}}\widetilde{\mathbf{Grad}}_a^{\,n+\frac{1}{2}}\{p_b^{n+\frac{1}{2}}\} + \mathbf{g} \\ \mathbf{r}_a^{n+1} & = & \mathbf{r}_a^n + \dfrac{1}{2}\delta t\mathbf{u}_a^{n+1} \end{cases} \tag{2.27}$$

However, we will not use it in the simulations, given that a first-order scheme give satisfactory results.

[1] We have reduced the time step by setting the speed of sound at $100m.s^{-1}$ instead of $20m.s^{-1}$.

Initialization of the density field: The time-scheme (2.26) requires initial values for the density field. Many choices are possible. First of all a particle a can have the reference density ρ_0 as initial value, *i.e.*

$$\rho_a^0 = \rho_0 \tag{2.28}$$

That is what was done previously with the continuity equation of (2.21). The advantage is that the continuity equation only measures the variation of density and not the initial disorder of the particles. But the main drawback is that precisely, we introduce an inhomogeneity between particles, and it could lead to non-physical behaviour.

Indeed, the continuity equation of the system (2.26) can be rewritten for an arbitrary time:

$$(\gamma_a \rho_a) = (\gamma_a \rho_a)^0 - \sum_{b \in \mathcal{F}^0} m_b w_{ab}^0 + \sum_{b \in \mathcal{F}} m_b w_{ab} \tag{2.29}$$

where $\mathcal{F}_0$ is the set of fluid particles at time 0. Then, for instance, if a particle a initially next to the free-surface (*i.e.* $\sum_{b \in \mathcal{F}^0} m_b w_{ab}^0 \simeq \frac{\rho_0}{2}$) is forced to move inside the fluid (where $\sum_{b \in \mathcal{F}^0} m_b w_{ab}^0 \simeq \rho_0$) because of a wave break for instance, and if moreover we assume that the particle a stays far from the walls (*i.e.* $\gamma_a = 1$) then its density given by (2.29) becomes:

$$\rho_a \simeq \frac{3}{2}\rho_0 \tag{2.30}$$

This phenomenon is illustrated on the Figure 2.7 where some particles repulse the others after a wave break. This is only due to the Equation (2.28).

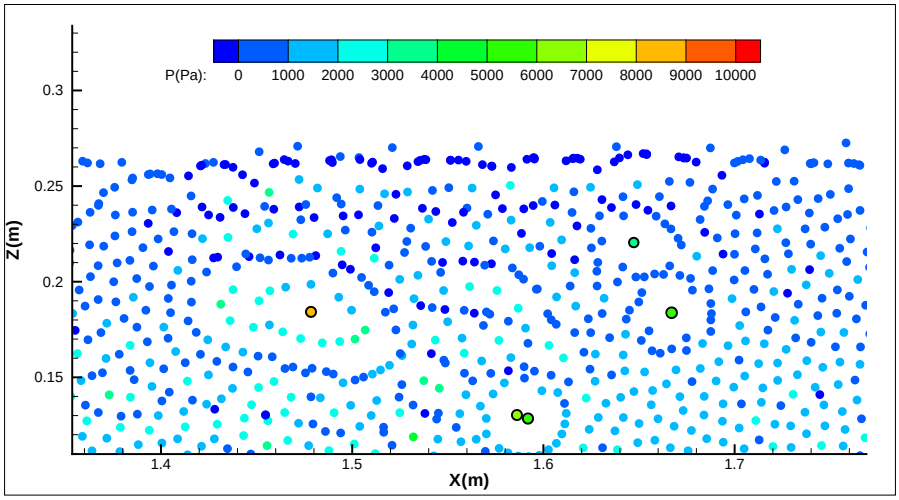

Figure 2.7: Pressure field of a free-surface flow after a wave break: circled particles originally at the free-surface have a too big density and then repulse the other particles.

The second possibility is to initialize the field $\{\rho_a^0\}$ such that:

$$\rho_a^0 = \frac{1}{\gamma_a^0} \sum_{b \in \mathcal{F}^0} m_b w_{ab}^0 \tag{2.31}$$

This initialization has the advantage to keep homogeneity between particles, but requires a free-surface correction.

Free-surface correction: The γ correction presented in this report does not take into account any free-surface correction. The variable $\tilde{\rho}_a \equiv \sum_{b \in \mathcal{F}} m_b w_{ab}$ depends only on the particles positions which is useful for conservation properties. The problem is that $\tilde{\rho}_a$ measures two different quantities:

(*i*) if the particles are approaching or going away, which is the quantity of interest, and

(*ii*) if a particle has a void in its kernel support.

Option (*i*) is what we want to measure whereas (*ii*) is corrected with γ_a next to a wall, but not next to the free-surface. Thus, we use the following Shepard filter:

$$\alpha(\mathbf{r}) = \sum_{b \in \mathcal{F}} \frac{m_b}{\rho_b} w(\mathbf{r} - \mathbf{r}_b) \tag{2.32}$$

So, for a fluid particle $a \in \mathcal{F} \setminus \mathcal{E}$ we have

$$\alpha_a \equiv \sum_{b \in \mathcal{F}} \frac{m_b}{\rho_b} w_{ab} \tag{2.33}$$

For an edge particle $e \in \mathcal{E}$ and for the middle of a segment $s \in \mathcal{S}$ we define:

$$\begin{aligned} \alpha_e &\equiv \sum_{b \in \mathcal{F} \setminus \mathcal{E}} \frac{m_b}{\rho_b} w_{eb} \\ \alpha_s &\equiv \sum_{b \in \mathcal{F} \setminus \mathcal{E}} \frac{m_b}{\rho_b} w_{sb} \end{aligned} \tag{2.34}$$

because α_e and α_s are used to evaluate quantities such as the density or the pressure at the wall so we have chosen not to take into account edge particles and have explicit interpolation on Lagrangian fluid particles of the physical quantities (such as the density ρ or the pressure p) at the walls (see §2.1.2).

We want to apply the Shepard filter (2.33) on the density field at each time step but only next to the free-surface. We also have to bear in mind that we must not correct the density field everywhere with α_a since if we do so, the walls are not Eulerian anymore and will not be kept impermeable (see §2.3).

We propose the following continuous mix to correct the continuity equation in the vicinity of a free-surface:

$$\rho_a \left[\beta \gamma_a + (1 - \beta)\, \alpha_a\right] = \tilde{\rho}_a = \sum_{b \in \mathcal{F}} m_b w_{ab} \tag{2.35}$$

where

$$\beta = \exp\left[-K \left(\min\left\{\frac{\alpha_a}{\gamma_a}; 1\right\} - 1\right)^2\right] \tag{2.36}$$

and K is taken to be an arbitrary high value of 30000, so that $\beta \simeq 1$ when $\frac{\alpha_a}{\gamma_a} < 0.99$. Note β is in fact surface-marker: inside the fluid its value is almost one whereas it tends to zero as we approach the free-surface.

Another choice, non-continuous but simpler to compute, could be:

$$\begin{cases} \beta = 1 \quad \text{if} & \dfrac{\alpha_a}{\gamma_a} > 0.99 \\ \beta = 0 \quad \text{otherwise} & \end{cases} \tag{2.37}$$

The latter definition of β is not used in the present work.

2.3 Computation of the renormalization terms

The formal definitions of the geometrical quantities γ_a and $\boldsymbol{\nabla}\gamma_a$ for a particle a are:

$$\begin{aligned} \gamma_a &\equiv \int_{\Omega \cap \Omega_a} w(\mathbf{r} - \mathbf{r}_a)\, \mathrm{d}\mathbf{r} \\ \boldsymbol{\nabla}\gamma_a &\equiv \int_{\Omega \cap \Omega_a} \boldsymbol{\nabla}_a w(\mathbf{r} - \mathbf{r}_a)\, \mathrm{d}\mathbf{r} = \int_{\partial\Omega \cap \Omega_a} w(\mathbf{r} - \mathbf{r}_a)\, \mathbf{n} \mathrm{d}S \end{aligned} \tag{2.38}$$

We recall that the second formula for $\boldsymbol{\nabla}\gamma_a$ in (2.38) is obtained using Gauss' theorem. It shows that $\boldsymbol{\nabla}\gamma_a$ represents an approximation of the normal to the wall for a particle located at the position $\mathbf{r}_a$.

Two main different methods are proposed in the literature to compute these terms:

- Kulasegaram *et al.* [15] use a polynomial approximation for the intersection of the kernel support with a plane. They generalised it to more complex geometries using bilinear combinations. De Leffe *et al.* also use polynomial approximation. This method has the advantage to be efficient to compute, but can be difficult to define for complex geometries.
- Feldman and Bonet [9] use an analytical solution for computing both γ_a and its *gradient*, which is then accurate but computationally more expensive.
- Marongiu *et al.* [20] use a discrete summation over boundary points, which is easy but less accurate.

Here, we propose different methods using discrete approximations of (2.38). Some use fictitious particles and have been mainly developed for investigation. We advocate to compute the renormalization term of the kernel support near a solid with a time integration scheme, thereby more easily accounting for any shape of boundaries presented in §2.1.2.

First approach

In this first approach to compute the value of γ_a and $\boldsymbol{\nabla}\gamma_a$, we consider a domain with a boundary as defined in Figure 2.3. We also discretize the outside volume using particles denoted by a subscript f (for fictitious) with a volume V_f (see Figure 2.8(a)). The set containing all the fictitious particles is denoted by $\mathcal{G}$ (stands for *ghost*).

These particles do not belong to the domain, but are only used to compute approximations of the quantities γ_a and $\boldsymbol{\nabla}\gamma_a$ as follows:

$$\left\{\begin{array}{rcl} \gamma_a &=& 1 - \displaystyle\sum_{f\,\in\,\mathcal{G}\cup\mathcal{E}} V_f w_{af} \\ \boldsymbol{\nabla}\gamma_a &=& -\displaystyle\sum_{f\,\in\,\mathcal{G}\cup\mathcal{E}} V_f \boldsymbol{\nabla} w_{af} \end{array}\right. \tag{2.39a}$$

or

$$\left\{\begin{array}{rcl} \gamma_a &=& 1 - \displaystyle\sum_{f\,\in\,\mathcal{G}\cup\mathcal{E}} V_f w_{af} \\ \boldsymbol{\nabla}\gamma_a &=& \displaystyle\sum_{s\,\in\,\mathcal{S}} S_s w_{as} \mathbf{n}_s \end{array}\right. \tag{2.39b}$$

Recall that $\mathcal{F}$ is the set of fluid particles, $\mathcal{E}$ is the set of edge particles and $\mathcal{S}$ is the set of the surface elements.

We can observe that the equation of $\boldsymbol{\nabla}\gamma_a$ in (2.39b) consists of the following approximation:

$$\boldsymbol{\nabla}\gamma_{as} \simeq w_{as} S_s \mathbf{n}_s \tag{2.40}$$

that is to say, the value of the kernel is assumed to be constant on a segment s.

Moreover, we can notice that if the edge particles are regularly spaced at a distance δr, then S_s is nothing but δr (in $2D$). The result is shown in Figure 2.9. The main disadvantage of this method is that we use fictitious particles which can be problematic to define, especially in $3D$ and for complex geometries.

Second approach

An easier way of computing γ_a and its gradient is by using the correction of the kernel given by Bonet *et al.* [2]. It gives us a kernel which is zero consistent everywhere, but leads to problems because γ_a does not depend only on the geometry of the walls:

$$\left\{\begin{array}{rcl} \gamma_a &=& \alpha_a = \displaystyle\sum_{b\,\in\,\mathcal{F}} V_b w_{ab} \\ \boldsymbol{\nabla}\gamma_a &=& \displaystyle\sum_{s\,\in\,\mathcal{S}} S_s w_{as} \mathbf{n}_s \end{array}\right. \tag{2.41}$$

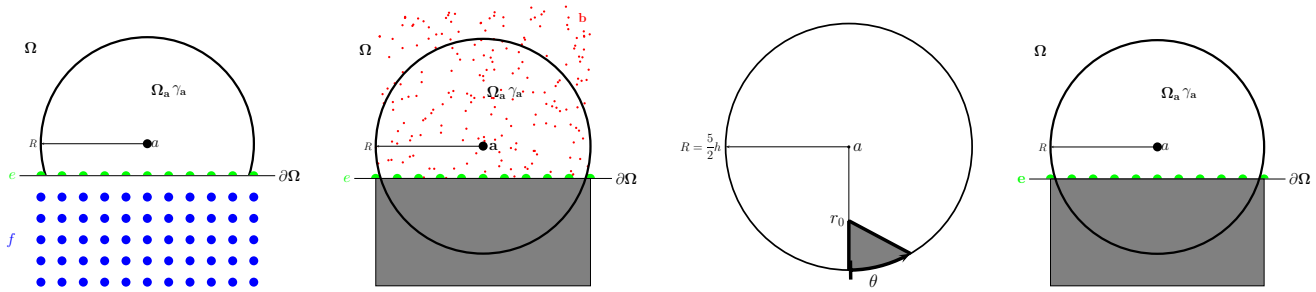

(a) First approach (b) Second approach (c) Domain where we compute analytically γ_a (d) Present approach

Figure 2.8: Illustrations of methods to compute the value of γ_a and $\boldsymbol{\nabla}\gamma_a$ with or without fictitious particles. In green the edge particles, in blue the fictitious particles and in red the fluid particles.

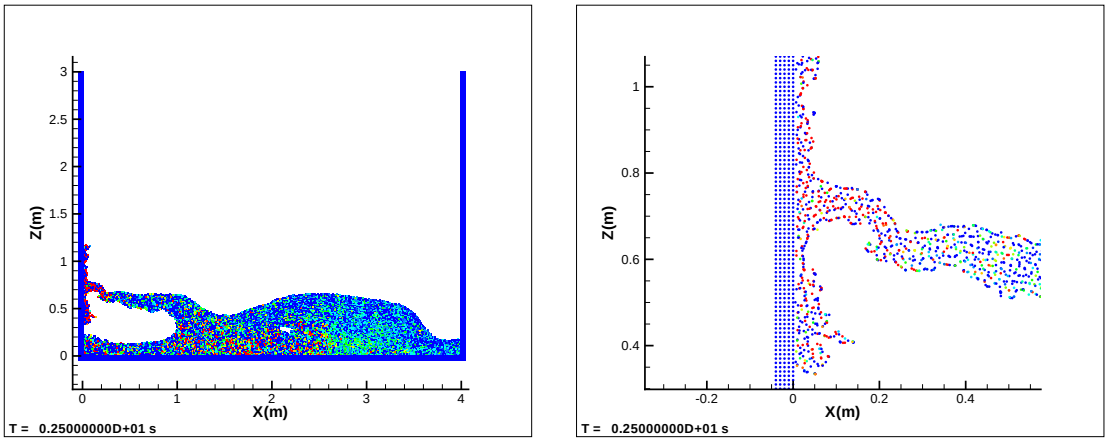

(a) Overview of the dam break (b) Zoom of the jet near the boundary

Figure 2.9: First approach to compute γ_a with the equation (2.39b) in the dam break test case.

In this method, we do not use fictitious particles anymore, only the "particles" of the edge remain, and we should say "points" as they are just a location for storing a normal and a surface (see Figure 2.8(b)). We can see in Figure 2.10 that this approach does not prevent particles from penetrating the wall, whereas the first one does (see Figure 2.9). As mentioned by De Leffe *et al.* [7], this is not the proper way to deal with solid boundaries.

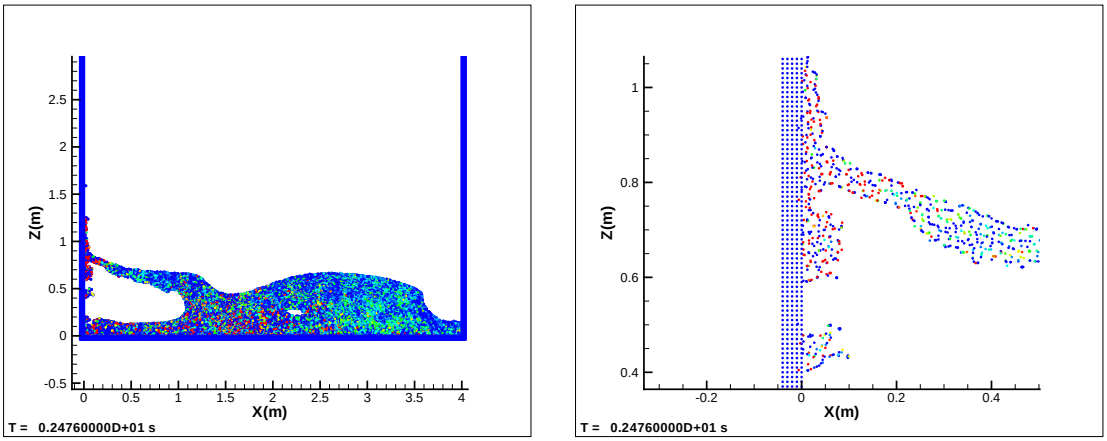

(a) Overview of the dam break

(b) Zoom of the jet near the boundary

Figure 2.10: Second approach to compute γ_a with the equation (2.41) in the dam break test case.

Analytical values

Analytical value of γ_a: We can in fact compute an analytical value of the function γ_a for the case represented in Figure 2.8(c). The integral of the kernel function of the grey domain is:

$$\begin{aligned} \gamma_a &= \int_{\Omega} w\left(\mathbf{r}\right) \mathrm{d}\Omega \\ &= \int_{r_0}^{R} r\, w\left(r\right) \left[\theta - \arcsin\left(\frac{r_0}{r}\sin\theta\right)\right] \mathrm{d}r \end{aligned} \tag{2.42}$$

In particular, for $\theta = \frac{\pi}{2}$ (we can then compute the value of γ_a for any plane boundary) and for the Wendland kernel defined by (1.24):

$$\gamma_a = \frac{1}{12\pi} \left\{ \begin{array}{l} \left(-22\left(\frac{r_0}{R}\right) + 60\left(\frac{r_0}{R}\right)^3 + 97\left(\frac{r_0}{R}\right)^5\right)\sqrt{1-\left(\frac{r_0}{R}\right)^2} \\ -\left(\frac{r_0}{R}\right)^5\left(15\left(\frac{r_0}{R}\right)^2 + 126\right)\ln\left(\dfrac{1+\sqrt{1-\left(\frac{r_0}{R}\right)^2}}{\left(\frac{r_0}{R}\right)}\right) \\ +6\arctan\left(\dfrac{\sqrt{1-\left(\frac{r_0}{R}\right)^2}}{\left(\frac{r_0}{R}\right)}\right) \end{array} \right\} \tag{2.43}$$

We can easily see that the value of γ_a tends to $\frac{1}{4}$ as r_0 tends to 0, which is consistent. We do not present here the formula obtained for an arbitrary angle θ which is much more complex.

Analytical value of $\nabla\gamma_a$: Recall that we assume here that in $2D$, the boundary of the domain is composed of segments denoted with the subscript $(.)_s$. Each segment has an inward normal $\mathbf{n}_s$, a beginning point $\mathbf{r}_{e1}$ and

an ending point $\mathbf{r}_{e2}$ (see Figure 2.3). Then we can compute the analytical value of the contribution $\boldsymbol{\nabla}\gamma_{as}$:

$$\boldsymbol{\nabla}\gamma_{as} \equiv \left(\int_{\mathbf{r}_{e1}}^{\mathbf{r}_{e2}} w\left(r\right) \mathrm{d}l\right) \mathbf{n}_s$$

with for the quintic kernel defined by (1.24):

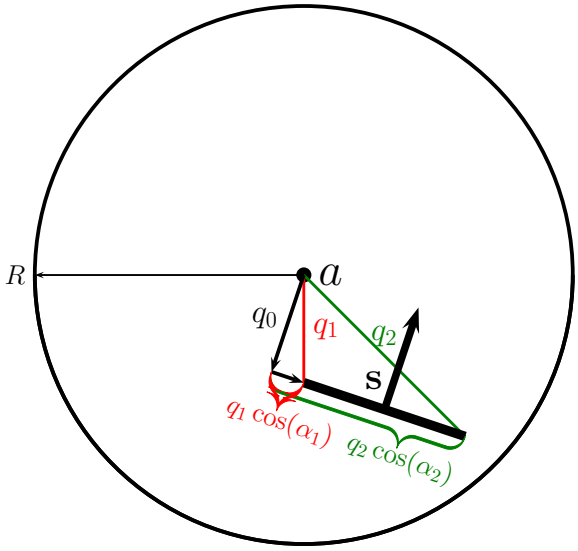

Figure 2.11: Schema showing the definitions of the geometrical parameters used to compute the analytical value of $\boldsymbol{\nabla}\gamma_{as}$ with (2.44).

$$\begin{aligned}\int_{\mathbf{r}_{e1}}^{\mathbf{r}_{e2}} w\left(r\right) \mathrm{d}l \quad &= \quad \frac{\left(q_2 \cos\alpha_2\right)}{\pi} P_{q_0}\left(q_2\right) - \frac{\left(q_1 \cos\alpha_1\right)}{\pi} P_{q_0}\left(q_1\right) \\ &\quad + \frac{q_0^4}{\pi}\left(\frac{105}{64} + \frac{35}{512} q_0^2\right) \left[\begin{array}{l} \mathtt{sign}\left(q_2 \cos\alpha_2\right) \ln\left(\dfrac{q_2 + \left|q_2 \cos\alpha_2\right|}{\left|q_0\right|}\right) \\ -\mathtt{sign}\left(q_1 \cos\alpha_1\right) \ln\left(\dfrac{q_1 + \left|q_1 \cos\alpha_1\right|}{\left|q_0\right|}\right) \end{array}\right]\end{aligned} \tag{2.44}$$

where:

$$\begin{aligned} P_{q_0}\left(q\right) \quad &= \quad \frac{7}{192} q^5 - \frac{21}{64} q^4 + \frac{35}{32} q^3 - \frac{35}{24} q^2 + \frac{7}{4} \\ &\quad + q_0^2 \left(\frac{35}{768} q^3 - \frac{7}{16} q^2 + \frac{105}{64} q - \frac{35}{12}\right) \\ &\quad + q_0^4 \left(\frac{35}{512} q - \frac{7}{8}\right) \end{aligned} \tag{2.45}$$

where q_0, $q_1 \cos\alpha_1$ and $q_2 \cos\alpha_2$ are defined in Figure 2.11.

These analytical values are of interest to compare the different approaches and estimate the error due to the approximations. In Figure 2.12 we compare the analytical and the approximate values of γ_a and $\boldsymbol{\nabla}\gamma_a$ against the distance to plan wall. The discrete approximation used is given by (2.39b), the kernel is the 4^{th} order spline-based kernel (1.22) and the ratio $\dfrac{\delta r}{h} = 1.5$ where we recall that δr is the initial distance between two fluid particles and h is the smoothing length. We define the absolute errors to be:

$$\begin{aligned} \epsilon_{\gamma_a} \quad &= \quad \frac{\left|\gamma_a^{\text{analytical}} - \gamma_a^{\text{discrete}}\right|}{\gamma_a^{\text{analytical}}} \\ \epsilon_{\boldsymbol{\nabla}\gamma_a} \quad &= \quad \frac{\left|\nabla\gamma_a^{\text{analytical}} - \nabla\gamma_a^{\text{discrete}}\right|}{\nabla\gamma_a^{\text{analytical}}} \end{aligned} \tag{2.46}$$

(We consider only the component of $\boldsymbol{\nabla}\gamma_a$ orthogonal to the wall). We observe that the error done by the discretization for $\boldsymbol{\nabla}\gamma_a$ is very good for such a poor discretization ratio $\frac{\delta r}{h}$ for a plane wall (less than 0.1%) whereas the discretization makes a systematic error for the approximation of the value of γ_a of the order of 3%.

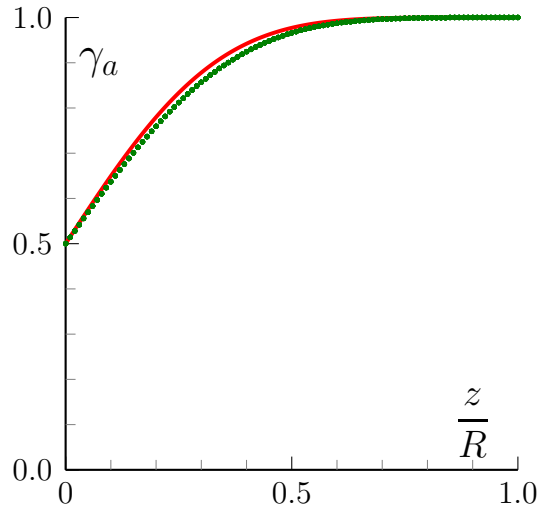

(a) Values of the γ_a function against the distance of the wall.

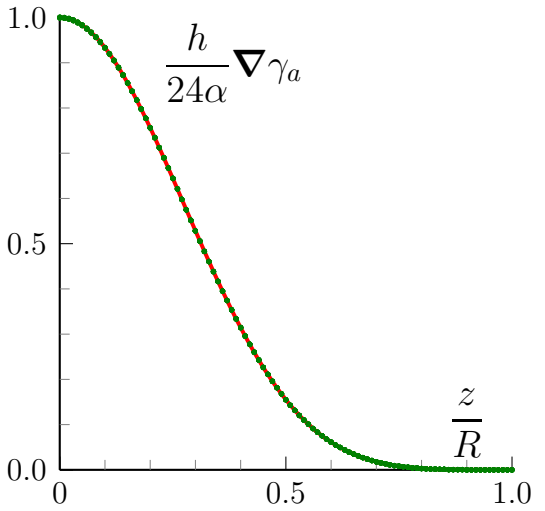

(b) Values of the $\boldsymbol{\nabla}\gamma_a$ function against the distance of the wall.

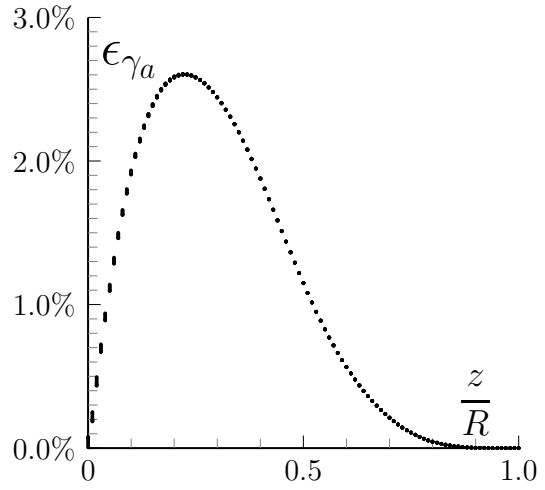

(c) Values of the error function ϵ_{γ_a} against the distance of the wall.

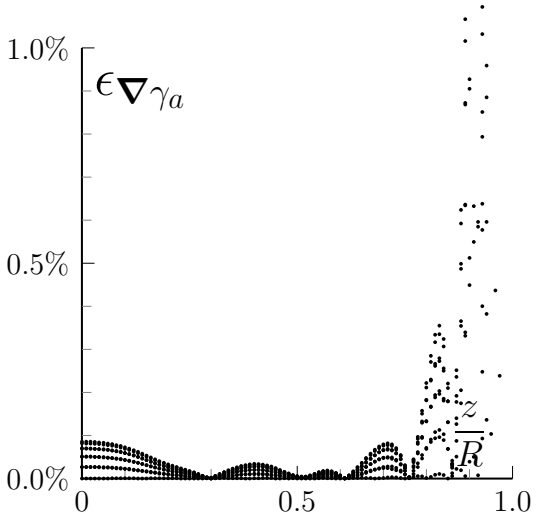

(d) Values of the error function $\epsilon_{\boldsymbol{\nabla}\gamma_a}$ against the distance of the wall.

Figure 2.12: First approach. Analytical in red and computed values in green of the functions against the distance to a plane wall.

If we investigate the error due to the discretization for $\boldsymbol{\nabla}\gamma_a$ in the presence of a wedge (see §3.2 for the total description of the test case), we observe that a bigger error is done. Moreover, the error is systematic, in the sense that we always underestimate the magnitude of $\boldsymbol{\nabla}\gamma_a$. This leads to non-physical behaviour: particles slide towards the wedge in a still water test case because the gravity is not totally balanced by the wall repulsive force proportional to $\boldsymbol{\nabla}\gamma_a$ as we can be convinced by Figure 2.13.

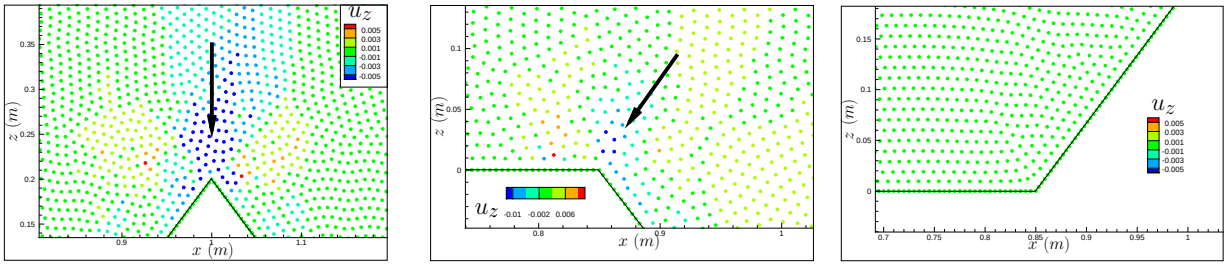

(a) Particles keep moving towards the wedge at the steady state.

(b) Particles keep moving towards this other wedge at the steady state.

(c) For this shape, particles remain fixed. The gravity is well balanced by the wall force.

Figure 2.13: Plot of the vertical velocity field in a tank with gravity for different geometries. The approximation to compute $\boldsymbol{\nabla}\gamma_a$ leads to spurious re-circulations in the direction of a wedge.

Indeed, if we would plot the value of $\boldsymbol{\nabla}\gamma_a$ given by the sum approximation (2.39b) against the distance to a wedge, we could see that we systematically underestimate its value. Thus, the repulsive forces, which is proportional to $\boldsymbol{\nabla}\gamma_a$, is not able to balance the gravity field.

New approach

In this report, we will use a method to compute γ_a for a particle a near a solid boundary without fictitious particles and much simpler than an analytic computation. The main idea of the present method is to use a governing equation of γ_a. First of all we have:

$$\begin{cases} \dfrac{\mathrm{d}\gamma_a}{\mathrm{d}t} &= \boldsymbol{\nabla}\gamma_a.\mathbf{u}_a \\ \gamma_a &= 1 \qquad \text{if } \partial\Omega \cap \Omega_a = \emptyset \end{cases} \tag{2.47}$$

This equation is nothing else but the definition of the *gradient* combined with the fact that $\dfrac{\mathrm{d}\mathbf{r}_a}{\mathrm{d}t} = \mathbf{u}_a$. An other way to consider this equation is to remark that (2.47) is equivalent to:

$$\begin{cases} \dfrac{\partial\gamma_a}{\partial t} &= 0 \\ \gamma_a &= 1 \quad \text{if } \partial\Omega \cap \Omega_a = \emptyset \end{cases} \tag{2.48}$$

This means that the γ_a field does not depend on the time[2], but just on the position, and is therefore an Eulerian field. So it gives us a means to compute γ_a to be coherent with $\boldsymbol{\nabla}\gamma_a$ which is easier to compute, since it can be expressed as a surface integral.

We can extend the relation (2.47) to the case of a moving wall. Indeed, if the wall is rigid and if we denote $\mathbf{u}_a^{\mathcal{R}}$ the velocity of the particle a in the referential $\mathcal{R}$ linked to the wall [3], then (2.47) becomes:

$$\begin{cases} \dfrac{\mathrm{d}\gamma_a}{\mathrm{d}t} &= \boldsymbol{\nabla}\gamma_a.\mathbf{u}_a^{\mathcal{R}} \\ \gamma_a &= 1 \qquad \text{if } \partial\Omega \cap \Omega_a = \emptyset \end{cases} \tag{2.49}$$

[2] if the wall does not move.

[3] for instance, if the wall is translating with a velocity $\mathbf{u}_w$, then $\mathbf{u}_a^{\mathcal{R}} = \mathbf{u}_a - \mathbf{u}_w$. More generally, if the wall is rotating with a rotating angle $\boldsymbol{\Omega}_s$ around the point $\mathbf{r}_s$ moving at the speed $\mathbf{u}_s$, then we have $\mathbf{u}_a^{\mathcal{R}} = \mathbf{u}_a - \mathbf{u}_s - \boldsymbol{\Omega}_s \times (\mathbf{r}_a - \mathbf{r}_s)$

Recall that the boundary defined by Figure 2.3, then, if we have a deformable wall (in the sense that each segment or triangle composing the wall is moving with its velocity) we obtain the following formula:

$$\begin{cases} \dfrac{\mathrm{d}\gamma_a}{\mathrm{d}t} &= \displaystyle\sum_{s\,\in\,\mathcal{S}} \boldsymbol{\nabla}\gamma_{as}.\mathbf{u}_a^{\mathcal{R}_s} \\ \gamma_a &= 1 \qquad\qquad\qquad \text{if } \partial\Omega \cap \Omega_a = \emptyset \end{cases} \tag{2.50}$$

where $\mathbf{u}_a^{\mathcal{R}_s}$ is the velocity of the particle a in a reference frame $\mathcal{R}_s$ where the segment s is fixed.

It is important to remark that the function γ_a is well defined if for all positions $\mathbf{r}_a$ in Ω, the set $\Omega \cap \Omega_a$ is connex. That is for example not the case on the Figure 2.14.

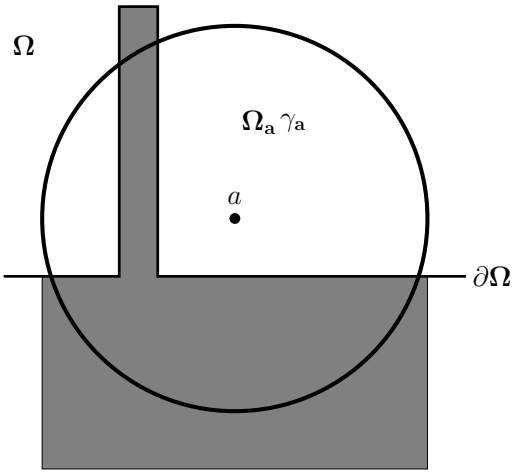

Figure 2.14: Schema of a case where γ_a is ambiguously defined.

Initialization of the γ_a field: The initialization step of γ_a^0 is done by imaging a virtual transformation. For each particle initially next to a solid wall (a criterion is $\left|\boldsymbol{\nabla}\gamma_a^0\right| > 0$), we move it from its position $(x_0,\, z_0)$ to an area where the function $\gamma\,(\mathbf{r}) \equiv 1$. For instance:

$$\begin{aligned} x &= x_0 + l\frac{\nabla\gamma_{a,x}^0}{|\boldsymbol{\nabla}\gamma_a^0|} \\ z &= z_0 + l\frac{\nabla\gamma_{a,z}^0}{|\boldsymbol{\nabla}\gamma_a^0|} \end{aligned} \tag{2.51}$$

where the length l is taken to be $2R$, where we recall that R is the radius of the compact kernel support. We notice that Equation (2.51) can be rewritten in a vector form as: $\mathbf{r}_a = \mathbf{r}_a^0 + l\dfrac{\boldsymbol{\nabla}\gamma_a^0}{|\boldsymbol{\nabla}\gamma_a^0|}$.

A sketch of the proposed method is displayed in Figure 2.15. For example, the green circled particle on the Figure 2.15(b) is put behind the dashed line where the value of γ is 1, and we move it be back to its initial position along the path of the large black arrow updating the value of γ_a with respect to the governing Equation (2.50).

Note that we discretize in time the equation of γ_a with a second-order time integration scheme to prevent systematic integration errors (see §2.6), leading to:

$$\left\{ \gamma_a^{n+1} = \gamma_a^n + \frac{1}{2}\left(\boldsymbol{\nabla}^n\gamma_a + \boldsymbol{\nabla}^{n+1}\gamma_a\right).\left(\mathbf{r}_a^{n+1} - \mathbf{r}_a^n\right) \right. \tag{2.52}$$

if the solid boundary is motionless.

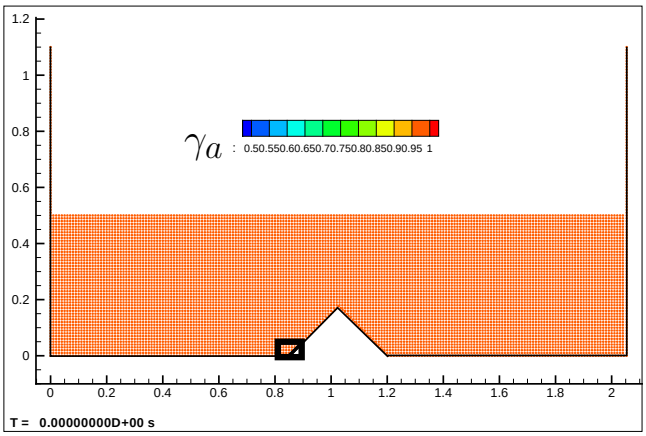

(a) Overview of the domain before the initialization of γ_a, the black box is zoomed in the twin figure.

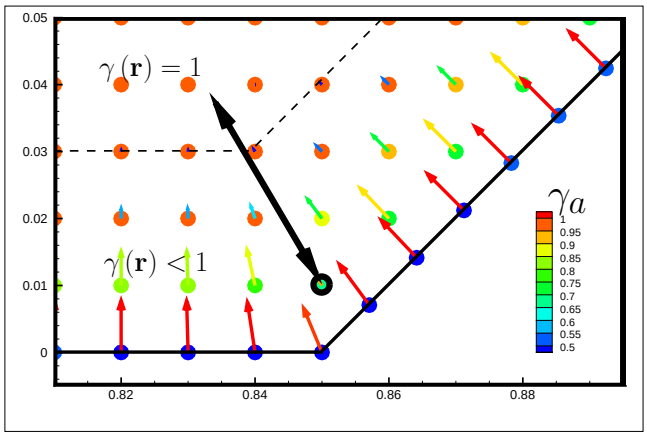

(b) Zoom of an area where we have initialized the value of γ. The coloured vectors represent $\boldsymbol{\nabla}\gamma$

Figure 2.15: Sketch of the initialization of the γ field next to a solid wall.

The general formula for a moving deformable wall is:

$$\left\{ \quad \gamma_a^{n+1} \quad = \quad \gamma_a^n + \frac{\delta t}{2} \sum_{s \in \mathcal{S}} \left(\boldsymbol{\nabla}^n \gamma_{as} + \boldsymbol{\nabla}^{n+1} \gamma_{as} \right) . \left(\mathbf{u}_a^{\mathcal{R}_s} \right)^{n+1} \tag{2.53}$$

At this stage, we can add a condition on the time step, to be accurate in the integration of γ_a:

$$\delta t \quad \leq \quad C_{t,\gamma} \frac{1}{\max\limits_{a \in \mathcal{F}} \{ | \boldsymbol{\nabla}^n \gamma_a . \mathbf{u}_a^n | \}} \tag{2.54}$$

where $C_{t,\gamma} = 0.01$.

This is a natural condition, in the sense that we decrease the time step when particles are splashing against a wall in order to be more accurate.

An analogous condition could be written if we deal with a deformable moving wall:

$$\delta t \quad \leq \quad \tilde{C}_{t,\gamma} \frac{1}{\max\limits_{a \in \mathcal{F}; s \in \mathcal{S}} \left\{ \left| \boldsymbol{\nabla}^n \gamma_{as} . \left(\mathbf{u}_a^{\mathcal{R}_s} \right)^n \right| \right\}} \tag{2.55}$$

where $\tilde{C}_{t,\gamma} = 0.005$, from numerical experience.

2.4 Wall shear stress and renormalization

Recall that the two main models in *SPARTACUS-2D* for computing the viscous term $\frac{1}{\rho}\boldsymbol{\nabla}.\left(\mu\boldsymbol{\nabla}\,\mathbf{u}\right)$ are:

$$\frac{1}{\rho_a}\boldsymbol{\nabla}.\left(\mu\boldsymbol{\nabla}\,\mathbf{u}\right)_a = \sum_{b\,\in\,\mathcal{F}} m_b \frac{\mu_a+\mu_b}{\rho_a\rho_b}\frac{\mathbf{u}_{ab}}{r_{ab}^2}\mathbf{r}_{ab}.\boldsymbol{\nabla}w_{ab} \tag{2.56a}$$

$$\frac{1}{\rho_a}\boldsymbol{\nabla}.\left(\mu\boldsymbol{\nabla}\mathbf{u}\right)_a = 2(n+2)\sum_{b\,\in\,\mathcal{F}} m_b \frac{\mu_a+\mu_b}{\rho_a\rho_b}\frac{\mathbf{u}_{ab}.\mathbf{r}_{ab}}{r_{ab}^2}\boldsymbol{\nabla}w_{ab} \tag{2.56b}$$

Both of them can be seen as discrete approximations of continuous Laplacian operators. We recall that the continuous interpolation is defined by (2.10). For instance, if we consider the Morris' formula (2.56a), we can notice from the Equation (1.17) that the divergence operator $\mathbf{Div}_a\left\{\rho_b\nu_b\boldsymbol{\nabla}\mathbf{u}_b\right\}$ defined is nothing else but a discrete form of:

$$\begin{aligned}\left\langle\boldsymbol{\nabla}.\mu\boldsymbol{\nabla}\mathbf{u}\right\rangle(\mathbf{r}) &= \left\langle\boldsymbol{\nabla}_{r'}.\left[\left(\mu\boldsymbol{\nabla}\mathbf{u}\right)(\mathbf{r})+\left(\mu\boldsymbol{\nabla}\mathbf{u}\right)(\mathbf{r}')\right]\right\rangle(\mathbf{r})\\ &= -\frac{1}{\gamma(\mathbf{r})}\int_{\Omega\cap\Omega_r}\left[\left(\mu\boldsymbol{\nabla}\mathbf{u}\right)(\mathbf{r})+\left(\mu\boldsymbol{\nabla}\mathbf{u}\right)(\mathbf{r}')\right]\boldsymbol{\nabla}w\left(\mathbf{r}-\mathbf{r}'\right)\mathrm{d}\mathbf{r}'\\ &\quad -\frac{1}{\gamma(\mathbf{r})}\int_{\partial\Omega\cap\Omega_r}\left[\left(\mu\boldsymbol{\nabla}\mathbf{u}\right)(\mathbf{r})+\left(\mu\boldsymbol{\nabla}\mathbf{u}\right)(\mathbf{r}')\right].\mathbf{n}w\left(\mathbf{r}-\mathbf{r}'\right)\mathrm{d}\mathbf{r}'\end{aligned} \tag{2.57}$$

As in §2.1.2, the second line is provided by an integration by parts so that the boundary terms appear naturally. Let us recall that in that calculus $\mathbf{n}$ is the inward normal of the domain at the position $\mathbf{r}'$. If the particle a is far from the boundary, the last integral vanishes. But if we are close to a boundary, we can try to take into account this term.

The boundary terms are treated using the friction velocity u_τ. By definition we have:

$$\mu\frac{\partial\mathbf{u}}{\partial\mathbf{n}}\bigg|_{wall} \equiv \rho u_\tau\mathbf{u}_\tau \tag{2.58}$$

which represents the shear stress at the wall. By convention, $\mathbf{u}_\tau$ is chosen to have the same direction as the local velocity field. Then we could replace $\left(\rho\nu\boldsymbol{\nabla}\mathbf{u}\right)(\mathbf{r}').\mathbf{n}$ in the boundary integral of (2.57). For the other term, we invoke the continuity of the stress which states that the stress tensor $\boldsymbol{\sigma}$ verifies that $\boldsymbol{\sigma}.\mathbf{n}$ is a continuous vector field for every single normal vector $\mathbf{n}$. Thus we assume:

$$\left(\rho\nu\boldsymbol{\nabla}\mathbf{u}\right)(\mathbf{r}).\mathbf{n} \simeq \rho u_\tau\mathbf{u}_\tau(\mathbf{r}') \tag{2.59}$$

Then the boundary integral becomes:

$$\frac{1}{\gamma(\mathbf{r})}\int_{\partial\Omega\cap\Omega_r}\left[\left(\rho\nu\boldsymbol{\nabla}\mathbf{u}\right)(\mathbf{r})+\left(\rho\nu\boldsymbol{\nabla}\mathbf{u}\right)(\mathbf{r}')\right].\mathbf{n}w\left(\mathbf{r}-\mathbf{r}'\right)\mathrm{d}\mathbf{r}' \simeq \frac{2}{\gamma(\mathbf{r})}\int_{\partial\Omega\cap\Omega_r}\left(\rho u_\tau\mathbf{u}_\tau\right)(\mathbf{r}')w\left(\mathbf{r}-\mathbf{r}'\right)\mathrm{d}\mathbf{r}' \tag{2.60}$$

Eventually, we can discretize the continuous Laplacian operator and obtain a corrected one for the Morris formula:

$$\frac{1}{\rho_a}\boldsymbol{\nabla}.\left(\mu\boldsymbol{\nabla}\,\mathbf{u}\right)_a = \frac{1}{\gamma_a}\sum_{b\,\in\,\mathcal{F}} m_b\frac{\mu_a+\mu_b}{\rho_a\rho_b}\frac{\mathbf{u}_{ab}}{r_{ab}^2}\mathbf{r}_{ab}.\boldsymbol{\nabla}w_{ab} - \frac{2}{\gamma_a\rho_a}\sum_{s\,\in\,\mathcal{S}}\left|\boldsymbol{\nabla}\gamma_{as}\right|\rho_s u_{\tau s}\mathbf{u}_{\tau s} \tag{2.61}$$

We can notice that the factor 2 in front of the boundary term was also obtained by (2.14). It principally comes from the fact we use a symmetric version of the operators Laplacian or *gradient*.

Remark on the correction of other Laplacian operators

We can also calculate corrected formulae for the other models presented in §1.2.2. The main fact to observe is:

$$\boldsymbol{\nabla}\mathbf{u}^T.\mathbf{n}\big|_{wall} = 0 \tag{2.62}$$

because of the impermeability condition $\mathbf{u}.\mathbf{n}|_{wall} = 0$. Then, the theoretical boundary term of each Laplacian operator is the same as previously. Thus we obtain for the Monaghan model:

$$\frac{1}{\rho_a}\boldsymbol{\nabla}.\left(\mu\boldsymbol{\nabla}\mathbf{u}\right)_a = \frac{2(n+2)}{\gamma_a}\sum_{b\,\in\,\mathcal{F}} m_b \frac{\mu_a+\mu_b}{\rho_a\rho_b}\frac{\mathbf{u}_{ab}.\mathbf{r}_{ab}}{r_{ab}^2}\boldsymbol{\nabla}w_{ab} - \frac{2}{\gamma_a\rho_a}\sum_{s\,\in\,\mathcal{S}}\left|\boldsymbol{\nabla}\gamma_{as}\right|\rho_s u_{\tau s}\mathbf{u}_{\tau s} \tag{2.63}$$

and for the model (1.15):

$$\begin{aligned}\frac{1}{\rho_a}\boldsymbol{\nabla}.\left[\mu\left(\boldsymbol{\nabla}\mathbf{u}+\boldsymbol{\nabla}\mathbf{u}^T\right)\right]_a &= \frac{1}{\gamma_a}\sum_{b\,\in\,\mathcal{F}} m_b \frac{\frac{\mu_a+\mu_b}{2}}{\rho_a\rho_b}\left[(n+2)\frac{\mathbf{u}_{ab}.\mathbf{r}_{ab}}{r_{ab}^2}\boldsymbol{\nabla}w_{ab} + \frac{\boldsymbol{\nabla}w_{ab}.\mathbf{r}_{ab}}{r_{ab}^2}\mathbf{u}_{ab}\right] \\ &\quad -\frac{2}{\gamma_a\rho_a}\sum_{s\,\in\,\mathcal{S}}\left|\boldsymbol{\nabla}\gamma_{as}\right|\rho_s u_{\tau s}\mathbf{u}_{\tau s}\end{aligned} \tag{2.64}$$

2.4.1 Computation of the friction velocity in a laminar case

The friction velocity $\mathbf{u}_\tau$ is a quantity defined at the boundary. To compute it in a Computational Fluid Dynamic (*CFD*) code, instead of using its definition, we usually take the advantage of knowing the physical behaviour of the velocity field in the vicinity of the boundary. For example, in a laminar test case, the velocity profile is expected to be linear close to the wall and then the following relationship between distance to the wall z and velocity along the wall $\mathbf{u}$ holds:

$$u_\tau\mathbf{u}_\tau = \lim_{z\to 0}\frac{\nu\mathbf{u}}{z} \tag{2.65}$$

The main advantage is that we do not need to compute the derivative of the velocity field next to the wall, where it is difficult to compute. Another advantage is that we can extend the definition of the friction velocity in the area where particles interfere with the boundary, that is, when the kernel support intersects the walls. Hence, we define:

$$u_{\tau a}\mathbf{u}_{\tau a} = \frac{\nu\mathbf{u}_a}{z_a} \tag{2.66}$$

where z_a is the distance to the wall for a particle a.

Eventually, to evaluate $\rho_s u_{\tau s}\mathbf{u}_{\tau s}$ we use again the continuity of stresses (2.59) to establish:

$$\rho_e u_{\tau e}\mathbf{u}_{\tau e} = \frac{1}{\alpha_e}\sum_{b\,\in\,\mathcal{F}\setminus\mathcal{E}} V_b\rho_b u_{\tau b}\mathbf{u}_{\tau b}w_{be} \tag{2.67}$$

and

$$\rho_s u_{\tau s}\mathbf{u}_{\tau s} = \frac{\rho_{e1}u_{\tau e1}\mathbf{u}_{\tau e1} + \rho_{e2}u_{\tau e2}\mathbf{u}_{\tau e2}}{2} \tag{2.68}$$

where the edge particles $e1$ and $e2$ and α_e are defined in §2.1.2. These formulae are similar to (2.20).

2.4.2 Implicit treatment of the wall shear stress

The wall shear stress is a dissipative process which prevents the fluid from flowing too fast next a wall. Physically, the larger the velocity along a wall is, the larger the friction velocity is, and the shear stress acts in the opposite direction to the velocity. In *CFD*, a general rule to ensure stability of the scheme is to make all dissipative terms implicit. The Equation (2.66) allows us to tackle this in a straightforward manner:

$$\begin{aligned}\frac{\mathbf{u}_a^{n+1}-\mathbf{u}_a^n}{\Delta t} &= -\frac{1}{\rho_a}\widetilde{\mathbf{Grad}}_a^n\{p_b\} \\ &\quad +\frac{1}{\gamma_a}\sum_{b\,\in\,\mathcal{F}} m_b\left(\frac{\mu_a+\mu_b}{\rho_a\rho_b}\frac{\mathbf{u}_{ab}}{r_{ab}^2}\mathbf{r}_{ab}.\boldsymbol{\nabla}w_{ab}\right)^n - \frac{2\nu\mathbf{u}_a^{n+1}}{(\gamma_a)^n}\sum_{s\,\in\,\mathcal{S}}\frac{|\boldsymbol{\nabla}\gamma_{as}^n|}{\delta r_{as}^n}\end{aligned} \tag{2.69}$$

where δr_{as} is the distance for the particle a to the wall element s (*i.e.* z_a in (2.66)), more precisely:

$$\delta r_{as} = \max\left(\mathbf{r}_{as}.\mathbf{n}_s;\ \delta r\right) \tag{2.70}$$

we have added a physical limit to prevent a division by 0.

2.5 Boundary conditions for turbulence modelling in *SPH*

A large range of flows are governed by the Navier-Stokes equation (*NS*) where the fluid is expected to be Newtonian, *i.e.* such that the deviatoric part of the stress tensor is aligned with the strain rate tensor $\mathbf{s}$ defined by:

$$\mathbf{s} \equiv \frac{1}{2}\left(\boldsymbol{\nabla}\mathbf{u} + \boldsymbol{\nabla}\mathbf{u}^T\right) \tag{2.71}$$

Thus, the stress tensor is decomposed in:

$$\boldsymbol{\sigma} = p\mathbf{Id} + 2\mu\mathbf{s} \tag{2.72}$$

The *NS* momentum equation then reads:

$$\frac{\partial \mathbf{u}}{\partial t} + \underbrace{\mathbf{u}.\boldsymbol{\nabla}\mathbf{u}}_{\text{Convective part}} = \frac{1}{\rho}\boldsymbol{\nabla}p + \frac{2}{\rho}\boldsymbol{\nabla}.(\mu\mathbf{s}) + \mathbf{g} \tag{2.73}$$

When the convective part of the *NS* Equation (2.73), which is non-linear with respect to the velocity, is relatively large compared to the viscous part, instabilities occur. That phenomenon can be measured by the Reynolds number:

$$Re \equiv \frac{\mathcal{U}\mathcal{D}}{\nu} \tag{2.74}$$

where $\mathcal{U}$ and $\mathcal{D}$ are respectively a characteristic scale of velocity (*e.g.* the mean velocity of the field) and a characteristic scale of length (*e.g.*, if we consider a flow in a pipe, the diameter of the pipe). Usually, when the Reynolds number Re becomes larger than 3000, the flow is said to be turbulent and is complex to study, composed of many spins with different scales.

The flow can then be seen from a statistical point of view: Reynolds decomposition splits the velocity field $\mathbf{u}$ in two (see for instance Pope [30]): (*i*) the mean part denoted by $\overline{\mathbf{u}}$ and (*ii*) the fluctuating one $\mathbf{u}'$.

Mathematically speaking, $\mathbf{u}$ is assumed to be stochastic, so that $\overline{\mathbf{u}}$ is its expectation and $\mathbf{u}'$ is nothing else but $\mathbf{u} - \overline{\mathbf{u}}$ (see Pope [30] for further details). Physically speaking, we can consider the field to be evolving in time, hence $\overline{\mathbf{u}}$ is obtained by reproducing the same experiment many times and computing the mean velocity field (it is an application of the strong law of the large numbers). The mean operator is denoted by the over-bar.

The *NS* equation can be rewritten using some properties of the mean operator as follows:

$$\frac{\mathrm{D}\overline{\mathbf{u}}}{\mathrm{D}t} = \frac{1}{\rho}\boldsymbol{\nabla}\overline{p} + \frac{1}{\rho}\boldsymbol{\nabla}.(2\mu\mathbf{S} - \rho\mathbf{R}) + \mathbf{g} \tag{2.75}$$

where the derivative $\dfrac{\mathrm{D}}{\mathrm{D}t} \equiv \dfrac{\partial}{\partial t} + \overline{\mathbf{u}}.\boldsymbol{\nabla}$, $\mathbf{S} \equiv \overline{\mathbf{s}}$ and where the Reynolds' stress tensor $\mathbf{R}$ is defined by:

$$\mathbf{R} \equiv \overline{\mathbf{u}' \otimes \mathbf{u}'} \tag{2.76}$$

This symmetric tensor is the covariance matrix of the stochastic velocity field, in other words it is the second order momentum term. It is a new unknown and appears once we want to obtain the transport equation of the first order moment $\overline{\mathbf{u}}$. It is also possible to derive a transport equation of $\mathbf{R}$. The system cannot be closed exactly from the *NS* equations because the transport equation obtained has new unknowns such as the third order moment of the velocity field. We can then model either $\mathbf{R}$ (which is for instance the aim of the so called mixing length model, see [33]) and that is called a first-order closure (the second-order moment $\mathbf{R}$ is expressed as a function of first-order quantities such as the gradient of the mean velocity), or model the transport equation of the $\mathbf{R}$ which is a second-order closure. One important invariant of the Reynolds stress tensor $\mathbf{R}$ is its trace, the turbulent kinetic energy k defined by:

$$k \equiv \frac{1}{2}\mathbf{R} : \mathbf{I} = \frac{\overline{u'u'} + \overline{v'v'} + \overline{w'w'}}{2} \tag{2.77}$$

The same decomposition could be introduced on the density field $\rho = \overline{\rho} + \rho'$. It should be pointed out immediately that density fluctuates only in the case of a compressible fluid, which will *a priori* be the case with the fluid flows modelled by *SPH*, as quasi-incompressible conditions are being considered. Nevertheless, fluctuations in density remain very small owing to the high value of the speed of sound appearing in the equation

of state (1.4). We shall therefore consider these fluctuations to be negligible, which means setting $\overline{\rho} = \rho$. The averaged continuity equation therefore remains identical to the initial equation, apart from the fact that it is based on the average velocity field:

$$\frac{\mathrm{D}\rho}{\mathrm{D}t} = -\rho \boldsymbol{\nabla}.\{\overline{\mathbf{u}}\} \tag{2.78}$$

The $k-\epsilon$ model developed by Launder *et al.* [16] models the trace of the transport equation of $\mathbf{R}$ and its dissipation ϵ. Like the mixing length model, the $k-\epsilon$ model is combined with the Boussinesq closure hypothesis, which assumes that the Reynolds stress tensor $\mathbf{R}$ is aligned with the strain tensor of the mean velocity $\mathbf{S}$:

$$\mathbf{R} = \frac{2k}{3}\mathbf{I} + 2\nu_T \mathbf{S} \tag{2.79}$$

Equation (2.79) can be seen as the definition of the turbulent viscosity ν_T for an incompressible flow. Unlike the molecular viscosity, previously denoted by ν and now denoted by ν_0 to distinguish the turbulent from the laminar part, ν_T depends only on the characteristics of the flow and not on the fluid; ν_T can vary in space. Note, by analogy, we define the turbulent dynamic viscosity μ_T to be $\rho\nu_T$.

The mixing length model is based on a scale of the length L_m which can vary in space, and the turbulent viscosity is then given by:

$$\nu_T = L_m^2 S \tag{2.80}$$

The $k-\epsilon$ model consists in linking ν_T to the turbulent kinetic energy k and its dissipation ϵ:

$$\nu_T = C_\mu \frac{k^2}{\epsilon} \tag{2.81}$$

where the constant C_μ is defined in the Table 2.1. Two equations are added to close the system:

$$\begin{aligned}
\frac{\mathrm{D}k}{\mathrm{D}t} &= \underbrace{\frac{1}{\rho}\boldsymbol{\nabla}.\left[\left(\mu + \frac{\mu_T}{\sigma_k}\right)\boldsymbol{\nabla}k\right]}_{\text{Diffusion term}} + \underbrace{P}_{\substack{\text{Production}\\ \text{term}}} - \underbrace{\epsilon}_{\substack{\text{Dissipation}\\ \text{term}}} \\
\frac{\mathrm{D}\epsilon}{\mathrm{D}t} &= \underbrace{\frac{1}{\rho}\boldsymbol{\nabla}.\left[\left(\mu + \frac{\mu_T}{\sigma_\epsilon}\right)\boldsymbol{\nabla}\epsilon\right]}_{\text{Diffusion term}} + \frac{\epsilon}{k}\left(C_{\epsilon 1}P - C_{\epsilon 2}\epsilon\right)
\end{aligned} \tag{2.82}$$

The constants σ_k, σ_ϵ, $C_{\epsilon 1}$ and $C_{\epsilon 2}$ are displayed in the Table 2.1.

C_μ	$C_{\epsilon 1}$	$C_{\epsilon 2}$	σ_k	σ_ϵ
0.09	1.44	1.92	1.0	1.3

Table 2.1: Constants of the $k-\epsilon$ model [16].

The production term P is defined by:

$$P \equiv -\mathbf{R} : \mathbf{S} \tag{2.83}$$

Then, using (2.79) and assuming the flow incompressible (*i.e.* $\mathrm{div}\,(\overline{\mathbf{u}}) = 2\mathbf{S} : \mathbf{I} = 0$), we obtain:

$$P = \nu_T S^2 \tag{2.84}$$

where

$$S^2 \equiv 2\mathbf{S} : \mathbf{S} \tag{2.85}$$

2.5.1 State-of-the-art turbulence modelling in $2D$ *SPH*

The major work to discretize in the *SPH* form turbulent models was done by Violeau and Issa [34]. The Equation (2.82) of the $k-\epsilon$ model are considered to be a transport equation of a scalar, and then the diffusion part is descretize as follows:

$$\frac{1}{\rho_a}\boldsymbol{\nabla}.\left(B\boldsymbol{\nabla}\,A\right)_a = \sum_{b\,\in\,\mathcal{F}} m_b \frac{B_a+B_b}{\rho_a\rho_b}\frac{A_{ab}}{r_{ab}^2}\mathbf{r}_{ab}.\boldsymbol{\nabla}w_{ab} \tag{2.86}$$

where the scalar fields $\{A_b\}$ and $\{B_b\}$ can be respectively k or ϵ and μ_T/σ_k or μ_T/σ_ϵ. We can notice that this formula is nothing else but the Morris model (2.56a) applied to a scalar field.

Then the original version of the Reynolds Equation (2.75) and the $k-\epsilon$ Equations (2.82) read:

$$\begin{aligned}
\frac{\mathrm{D}\overline{\mathbf{u}}_a}{\mathrm{D}t} &= \frac{1}{\rho}\boldsymbol{\nabla}_a\left(p+\rho\tfrac{2}{3}k\right) + \sum_{b\,\in\,\mathcal{F}} m_b \frac{\mu_a+\mu_{Ta}+\mu_b+\mu_{Tb}}{\rho_a\rho_b}\frac{\overline{\mathbf{u}}_{ab}}{r_{ab}^2}\mathbf{r}_{ab}.\boldsymbol{\nabla}w_{ab} + \mathbf{g} \\
\frac{\mathrm{D}k_a}{\mathrm{D}t} &= \sum_{b\,\in\,\mathcal{F}} m_b \frac{2\mu+\mu_{Ta}/\sigma_k+\mu_{Tb}/\sigma_k}{\rho_a\rho_b}\frac{k_{ab}}{r_{ab}^2}\mathbf{r}_{ab}.\boldsymbol{\nabla}w_{ab} + P_a - \epsilon_a \\
\frac{\mathrm{D}\epsilon_a}{\mathrm{D}t} &= \sum_{b\,\in\,\mathcal{F}} m_b \frac{2\mu+\mu_{Ta}/\sigma_\epsilon+\mu_{Tb}/\sigma_\epsilon}{\rho_a\rho_b}\frac{\epsilon_{ab}}{r_{ab}^2}\mathbf{r}_{ab}.\boldsymbol{\nabla}w_{ab} + \frac{\epsilon_a}{k_a}\left(C_{\epsilon 1}P_a - C_{\epsilon 2}\epsilon_a\right)
\end{aligned} \tag{2.87}$$

We can apply the same wall correction of the diffusion term of the momentum equation as the laminar one, noticing that $(\mu+\mu_T)\,\mathbf{S}.\mathbf{n} \simeq \rho u_\tau \mathbf{u}_\tau$ in the vicinity of a wall[4]. Unlike the Equation (2.66) which links friction velocity to the mean velocity, in the turbulent case, we need another wall function. The viscosity is not constant anymore, and is supposed to be linear in the vicinity a wall[5]. Then it can be shown that the velocity profile in that area as a logarithmic shape: this zone is called the log layer. If we consider the particle a to be in the log layer of a smooth wall, u_τ can be obtained from the following wall law, with an iterative algorithm:

$$\frac{\overline{\mathbf{u}}_a}{u_{\tau a}} = \frac{1}{\kappa}\ln\left(\frac{z_a u_{\tau a}}{\nu}\right) + 5.2 \tag{2.88}$$

To be valid, the Equation (2.88) must verify that the non-dimensional distance to the wall $\frac{z_a u_{\tau a}}{\nu}$ is greater than 11. We could also use log laws for rough walls, or use laws which hold both in the laminar and the log layer such as Reichards' law, but then the $k-\epsilon$ model (2.82) must also be modified for low Reynolds effects. For more information see [30].

For the Equations of k and ϵ, an analogous work on diffusion terms has to be done. The gradient of the mean velocity used to compute the production of kinetic energy k also has to be wall corrected. This will be done in the next sections.

2.5.2 Correction of the strain rate

The strain rate of the mean flow plays a key role in the $k-\epsilon$ model because it is responsible for the production of kinetic energy. Given the fact that in a channel flow the strain rate is the biggest in the vicinity of the boundary, it is of a great interest to be accurate in this area.

Two models exists to compute it: (*i*) a model based on the tensor gradient of the mean velocity field $\{\overline{\mathbf{u}}_a\}$, (*ii*) another one based on the conservation of energy developed by Violeau [33]. Both of them require to be corrected with respect to the boundaries.

A *SPH* form of the velocity gradient is:

$$\boldsymbol{\nabla}_a\overline{\mathbf{u}} = -\frac{1}{\rho_a}\sum_{b\,\in\,\mathcal{F}} m_b\overline{\mathbf{u}}_{ab}\otimes\boldsymbol{\nabla}w_{ab} \tag{2.89}$$

[4]Formally, at a wall $k=0$ and then $\nu_T=0$ so that we recover the laminar case. However, the viscous sub-layer where the laminar viscosity is more important than the turbulent one is usually, for environmental flows, very thin so that we do not enforce k to be zero at a wall.

[5]In a channel flow, this assumption is well verified in 10% of the channel depth

This formula tends to underestimate the strain rate next to a wall (see Figure 2.16). To correct that we propose in a similar way as (2.13):

$$\boldsymbol{\nabla}_a \overline{\mathbf{u}} = -\frac{1}{\gamma_a \rho_a} \sum_{b \in \mathcal{F}} m_b \overline{\mathbf{u}}_{ab} \otimes \boldsymbol{\nabla} w_{ab} + \frac{1}{\gamma_a} \sum_{s \in \mathcal{S}} \overline{\mathbf{u}}_{as} \otimes \boldsymbol{\nabla} \gamma_{as} \tag{2.90}$$

Then the strain rate S is computed according to its definition (2.85).

Violeau [33] developed a model to compute the production of the kinetic energy based on the balance between dissipated energy and production which reads as follows:

$$\nu_{Ta} S_a^2 = -\frac{1}{2} \sum_{b \in \mathcal{F}} m_b \frac{\mu_{Ta} + \mu_{Tb}}{\rho_a \rho_b} \frac{\overline{u}_{ab}^2}{r_{ab}^2} \mathbf{r}_{ab}.\boldsymbol{\nabla} w_{ab} \tag{2.91}$$

If we want to take walls into account, we must also consider the energy dissipated by the friction against the wall, which leads to the following model:

$$\nu_{Ta} S_a^2 = -\frac{1}{2\gamma_a} \sum_{b \in \mathcal{F}} m_b \frac{\mu_{Ta} + \mu_{Tb}}{\rho_a \rho_b} \frac{\overline{u}_{ab}^2}{r_{ab}^2} \mathbf{r}_{ab}.\boldsymbol{\nabla} w_{ab} - \frac{2}{\gamma_a} \sum_{s \in \mathcal{S}} u_{\tau s}^2 \overline{u}_{as} \left| \boldsymbol{\nabla} \gamma_{as} \right| \tag{2.92}$$

Both (2.90) and (2.92) will be tested hereafter to compute the shear stress.

Computation of the strain rate in a laminar case To validate these formulae, we can investigate a laminar case, where there is no influence of the strain rate on the flow itself because the viscosity is supposed to be constant. Thus, such a test case allows us to compare the value of the computed strain rate to its analytical value. The simulation presented in §3.1.2 has a Reynolds number of $Re = 10$ and a laminar viscosity of $\nu = 1.10^{-1} m^2.s^{-1}$. The analytical profile of velocity is:

$$u_x(z) = 4\, Re \frac{\nu\, z}{D^2} \left(1 - \frac{z}{D}\right) \tag{2.93}$$

which leads to the following analytical value of S:

$$S(z) = 4\, Re \frac{\nu}{D^2} \left| 2\frac{z}{D} - 1 \right| \tag{2.94}$$

We notice in Figure 2.16 that in this theoretical test case, both corrected methods (2.90) and (2.92) give a satisfactory reproduction of the shear stress next to the wall unlike did the previous methods.

Remark on the velocity at the wall: We observe in the formulae (2.90) and (2.92) that the velocity at the wall $\overline{\mathbf{u}}_s$ is considered in the boundary term. Formally, the no-slip condition would impose that the velocity at the wall is the velocity of the wall itself (*i.e.* 0 for a motionless wall). This is what we impose for a laminar flow. In the turbulent case, it is preferable to not do so: the slope of the velocity profile is much larger at the wall than in the log layer where fluid particles are assumed to be. Thus if we want to evaluate accurately S_a next to the wall, we need to interpolate the velocity at the wall. To do so, we let the velocity $\overline{\mathbf{u}}_e$ of edge particles balance the viscous and friction terms:

$$\frac{\mathrm{D}\overline{\mathbf{u}}_e}{\mathrm{D}t} = \underbrace{\frac{1}{\gamma_e} \sum_{b \in \mathcal{F}} m_b \frac{\mu_{Te} + \mu_{Tb}}{\rho_e \rho_b} \frac{\overline{\mathbf{u}}_{eb}}{r_{eb}^2} \mathbf{r}_{eb}.\boldsymbol{\nabla} w_{eb}}_{\text{viscous term}} \underbrace{- \frac{2 u_{\tau e} \mathbf{u}_{\tau e}}{\gamma_e} \sum_{s \in \mathcal{S}} \left| \boldsymbol{\nabla} \gamma_{es} \right|}_{\text{friction term}} \tag{2.95}$$

We notice here that the Equation (2.95) is nothing else but the momentum equation applied to an edge particle without neither gravity nor pressure *gradient*. And we define $\overline{\mathbf{u}}_s$ to be interpolated between:

$$\overline{\mathbf{u}}_s = \frac{\overline{\mathbf{u}}_{e1} + \overline{\mathbf{u}}_{e2}}{2} \tag{2.96}$$

Wall particles $e1$ and $e2$ are defined in §2.1.2. This tactic to allow a kind of "slip" velocity at the wall in an high Reynolds number simulation is also used in many *CFD* codes such as *TELEMAC-3D* (see Hervouet [13]). Results are displayed in §3.1.3. Eventually, we have to bear in mind that the edge particles in $\mathcal{E}$ are in fact Eulerian points and do not move with the velocity $\overline{\mathbf{u}}_e$ but with the wall velocity. That is to say we only use the velocity $\overline{\mathbf{u}}_e$ to update viscous forces of fluid particles interacting with the wall, and to compute the strain rate S.

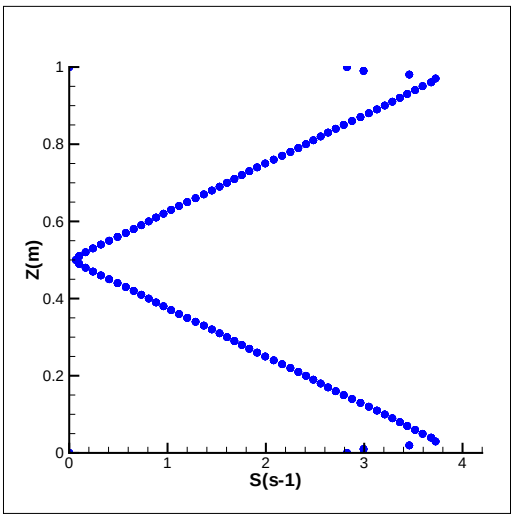

(a) Violeau's model (2.91)

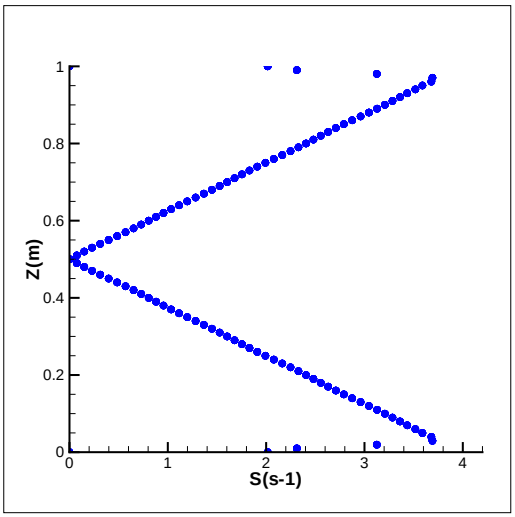

(b) Standard model (2.89)

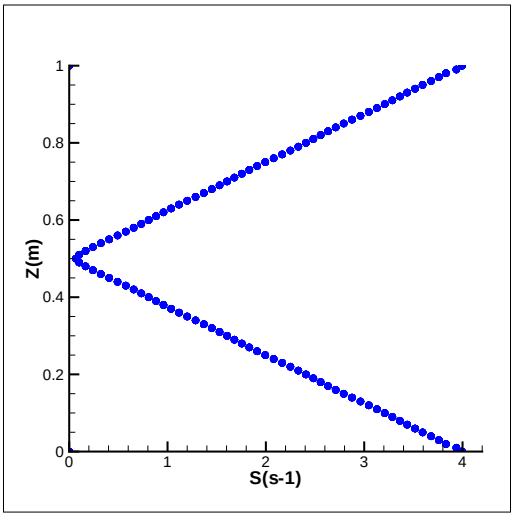

(c) Correction of Violeau's model (2.92)

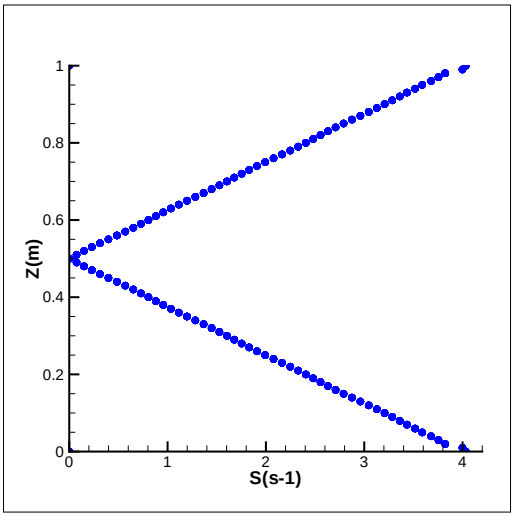

(d) Correction of Standard model (2.90)

Figure 2.16: Comparison of the strain rate for different models in a laminar channel flow.

2.5.3 Wall renormalization and flux conditions on $k-\epsilon$

As mentioned previously, the $k-\epsilon$ model is nothing else but coupled equations of transport of two scalar quantities k and ϵ with large source terms as the production P. The diffusion term requires particular attention, as the viscous term in the momentum equation needed to be corrected. Once again, the formula (2.86) of the diffusion of a scalar suffer from a lack of accuracy next to a wall. If we see it as the spatially discretized form of the continuous interpolation defined by (2.10), we propose the following wall-corrected operator:

$$\frac{1}{\rho_a}\boldsymbol{\nabla}.\left(B\boldsymbol{\nabla}\,A\right)_a = \frac{1}{\gamma_a}\sum_{b\,\in\,\mathcal{F}} m_b \frac{B_a+B_b}{\rho_a\rho_b}\frac{A_{ab}}{r_{ab}^2}\mathbf{r}_{ab}.\boldsymbol{\nabla}w_{ab} - \frac{2}{\gamma_a\rho_a}\sum_{s\,\in\,\mathcal{S}}\left|\boldsymbol{\nabla}\gamma_{as}\right| B_s\frac{\partial A_s}{\partial n_s} \tag{2.97}$$

As for the Equation (2.61), we have assumed here that $B_a\dfrac{\partial A_a}{\partial n_s} \simeq B_s\dfrac{\partial A_s}{\partial n_s}$, and we need to give it a value.

We can notice here that this approach can be used to solve the Poisson problem for the pressure field in an incompressible version of *SPH* (see Lee [17] or Xu [37]). Indeed, the Poisson problem is:

$$\begin{aligned} \Delta p &\equiv \boldsymbol{\nabla}.\boldsymbol{\nabla}p = f\left(\nu,\,\mathbf{u}\right) \\ p &= 0 \text{ at the free-surface} \\ \frac{\partial p}{\partial n} &= 0 \text{ at a wall} \end{aligned} \tag{2.98}$$

The formulation of the Laplacian operator (2.97) allows us to take into account the wall condition, as we did for the pressure field in the present report.

Flux conditions on the kinetic energy

The Laplacian operator (2.97) applied to the turbulent kinetic energy reduces to:

$$\frac{1}{\rho_a}\boldsymbol{\nabla}.\left[\left(\mu+\frac{\mu_T}{\sigma_k}\right)\boldsymbol{\nabla}\,k\right]_a = \frac{1}{\gamma_a}\sum_{b\,\in\,\mathcal{F}} m_b \frac{2\mu+\mu_{Ta}/\sigma_k+\mu_{Tb}/\sigma_k}{\rho_a\rho_b}\frac{k_{ab}}{r_{ab}^2}\mathbf{r}_{ab}.\boldsymbol{\nabla}w_{ab} \tag{2.99}$$

because it is assumed that there is no flux of k from the boundary, *i.e.* $\dfrac{\partial k}{\partial n}=0$ at the wall. The physical meaning is that the turbulent kinetic energy is only created by the flow. Moreover, instead of specifying boundary conditions **at** the wall, the "wall function" approach describes the balance of terms in the vicinity of the wall where it is assumed that $P=\epsilon$: this implies that the condition $\dfrac{\partial k}{\partial n}=0$ is valid not only at the wall, but in the whole vicinity of the solid boundary.

If we assume the flow to be highly turbulent, that is to say, with a really thin viscous sub-layer, we can use high Reynolds number laws for $k-\epsilon$. In fact we do not solve the $k-\epsilon$ model up to the wall, where k is theoretically expected to be 0, but up to a small distance δ from the wall, where the turbulence is fully established ($\nu_T \gg \nu$). The main advantage of the present Lagrangian approach compared to an Eulerian one is that all the Lagrangian fluid particles in $\mathcal{F}\setminus\mathcal{E}$ are always to be at least at a distance of the order of δr far from any wall. It is one of the main advantages compared to the mesh-based methods where the boundary elements are supposed to be at a virtual distance to the actual wall, here we only focus on particles which are affectively at a non-zero distance from the walls.

In order to estimate k at the wall we can evaluate as we did for the density, the pressure or the wall shear stress:

$$k_e = \frac{1}{\alpha_e}\sum_{b\,\in\,\mathcal{F}\setminus\mathcal{E}} V_b k_b w_{be} \tag{2.100}$$

We notice that this approximation is consistent with the assumption $\dfrac{\partial k}{\partial n}=0$. Finally:

$$k_s = \frac{k_{e1}+k_{e2}}{2} \tag{2.101}$$

Flux conditions on the dissipation of kinetic energy

The Laplacian operator (2.97) applied to ϵ requires the value for $\partial\epsilon/\partial n$. Once again, if we assume that the flow is highly turbulent, then every single particle in the area of influence of a wall (*i.e.* $\exists s \in \mathcal{S}/\,|\boldsymbol{\nabla}\gamma_{as}| > 0$) is in the log layer where[6]:

$$\begin{aligned} k &\simeq \frac{u^{\star 2}}{\sqrt{C_\mu}} \\ \epsilon &= \frac{u^{\star 3}}{\kappa z} \\ \nu_T &= \kappa u^\star z \end{aligned} \tag{2.102}$$

where z is the distance to the wall (if a particle a is interacting with a surface s, we recall that $z = \delta r_{as} = \max(\mathbf{r}_{as}.\mathbf{n}_s;\, \delta r)$), κ is the Von Karman constant with the value of 0.41 and $u^\star$ is a friction velocity measuring the turbulence:

$$u_s^\star = \frac{\sqrt{k_s}}{C_\mu^{\frac{1}{4}}} \tag{2.103}$$

Then, from Equation (2.102) we can deduce a value for the flux of ϵ:

$$\frac{\nu_{Ta}}{\sigma_\epsilon}\frac{\partial \epsilon_a}{\partial n_s} = -\frac{2u_s^{\star 4}}{\sigma_\epsilon \kappa \delta r_{as}} \tag{2.104}$$

The factor 2 is provided by a first-order approximation (*i.e* the flux is evaluate at the distance $\frac{\delta r_{as}}{2}$). This accuracy is especially needed here because ϵ is supposed to vary in $\frac{1}{z}$ where z is the distance to the wall.

Thus the Laplacian (2.97) becomes:

$$\frac{1}{\rho_a}\boldsymbol{\nabla}.\left[\left(\mu + \frac{\mu_T}{\sigma_\epsilon}\right)\boldsymbol{\nabla}\,\epsilon\right]_a = \frac{1}{\gamma_a}\sum_{b\,\in\,\mathcal{F}} m_b \frac{2\mu + \mu_{Ta}/\sigma_\epsilon + \mu_{Tb}/\sigma_\epsilon}{\rho_a\rho_b}\frac{\epsilon_{ab}}{r_{ab}^2}\mathbf{r}_{ab}.\boldsymbol{\nabla}w_{ab} + \frac{4}{\gamma_a\rho_a}\sum_{s\,\in\,\mathcal{S}}|\boldsymbol{\nabla}\gamma_{as}|\,\rho_s\frac{u_s^{\star 4}}{\sigma_\epsilon\kappa\delta r_{as}} \tag{2.105}$$

Remark on the kinetic friction velocity $u^\star$: In this report, we have presented a numerical turbulent model based on two different friction velocities:

(*i*) $\mathbf{u}_\tau$ which is computed thanks to the mean velocity field $\{\overline{\mathbf{u}}_b\}$ assuming that next to a solid wall, the velocity profile is logarithmic,

(*ii*) $u^\star$ which is computed with the turbulence intensity next to a wall.

Physically speaking, these two scales of friction velocity have no reason to coincide, except from certain theoretical test cases such as a fully developed channel flow. But for sake of simplicity, and for numerical robustness we will consider that:

$$u_s^\star = u_{\tau s} \tag{2.106}$$

which is enforced by setting:

$$\begin{aligned} k_e &= \frac{u_{\tau e}^2}{\sqrt{C_\mu}} \\ k_s &= \frac{u_{\tau s}^2}{\sqrt{C_\mu}} \end{aligned} \tag{2.107}$$

Many different choices can be made here, for more information see for instance the documentation [1] of *CODE_SATURNE*, a finite volume code developed by *EDF R&D*.

[6] All the Equations (2.102) can be derived from the equilibrium $P = \epsilon$.

Chapter 3

Test cases

3.1 Channel flow test case

First of all, an open-channel flow with gravity has been simulated using periodic conditions on the right and on the left boundaries of the studied domain: a flow-rate is imposed and the aim of such a basic test case is to compare the different time schemes presented in Chapter 2 and test the different pressure *gradients*. Secondly, we investigate a periodic Poiseuille flow in a closed- channel to validate the wall shear stress formulation.

3.1.1 Comparison of time integration schemes

Here, an open periodic channel flow is simulated with gravity and $1m$ initial depth. To validate the proposed scheme, we can compare in Figure 3.1 the result we obtain by reducing the time-discretization (and then the systematic error in the density equation) in the time scheme (2.22) with the result we obtain with the time-scheme (2.26) with a larger time step[1]. By doing so, we have forced the scheme (2.22) to be stable and to converge but it is obvious that we have lost density during the stabilisation time: the water depth has decreased (see 3.1(b)) whereas it is not the case on the Figure 3.1(c). Figure 3.1(d) represents the same simulation with the conservative time scheme (2.26) and the corrected pressure *gradient* (2.13): the pressure field is hydrostatic as expected.

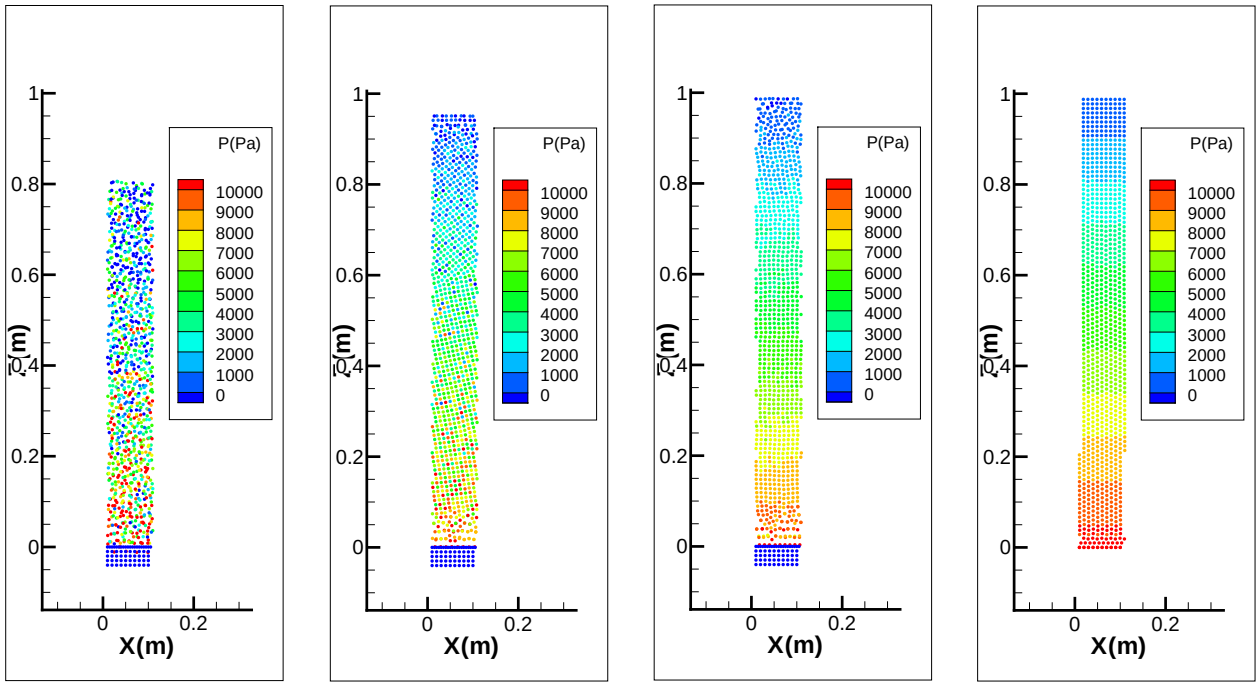

(a) Time scheme (2.22) with $c_0 = 20m.s^{-1}$.

(b) Time scheme (2.22) with $c_0 = 100m.s^{-1}$.

(c) Time scheme (2.26) with $c_0 = 20m.s^{-1}$ with Kulasegaram's *gradient* (2.7).

(d) Time scheme (2.26) with $c_0 = 20m.s^{-1}$ with *gradient* correction kernel (2.13).

Figure 3.1: Comparison of the pressure field and the depth for two different time schemes and different pressure *gradients* after the same physical time.

Hydrostatic pressure

The hydrostatic pressure field in an open channel flow is difficult to reproduce with the slightly compressible version of *SPH*, especially near the boundaries, without fictitious particles. The main reason is that discrete operators previously defined fail in the vicinity of a wall to give the correct value of a constant or a linear field.

[1] We have reduced the time step by setting the speed of sound at $100m.s^{-1}$ instead of $20m.s^{-1}$, see Equation (1.5).

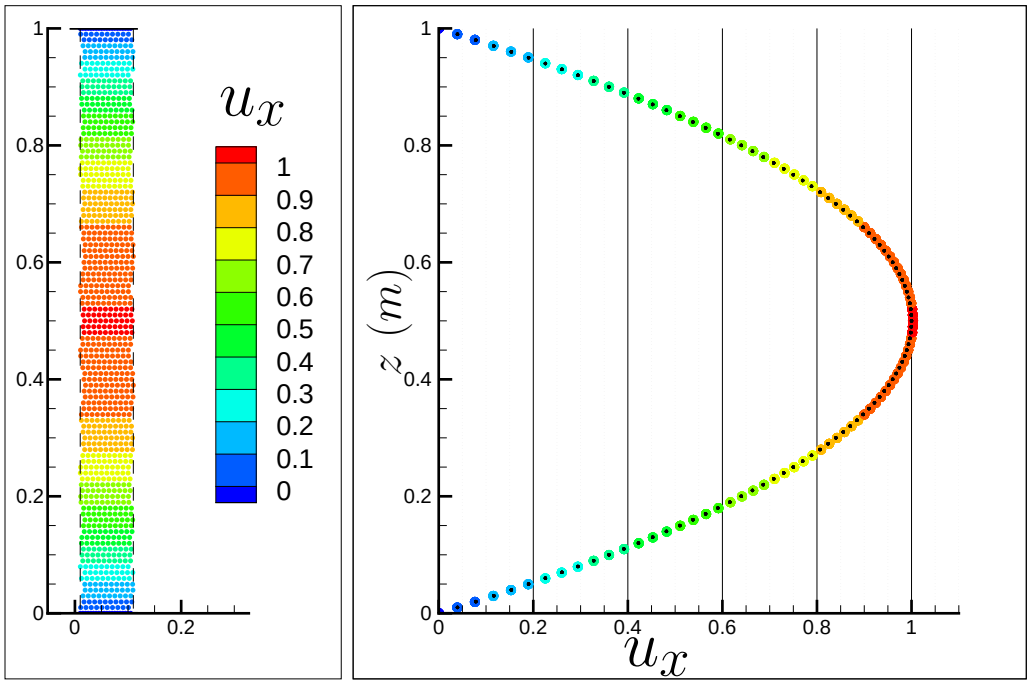

Figure 3.2: Poiseuille flow in a periodic pipe with a Reynolds number of 10. Coloured dots represent the velocity of particles at the steady state whereas the black dots • are the analytical profile (2.93).

Furthermore, due to its weakly compressible formulation there is a small but systematic compression in the water column. As we can see in Figure 3.1, a satisfactory pressure field is only obtained if we use the gradient operator (2.13). Although the Kulasegaram's method is fully conservative, the pressure field remains poor next to the bottom of the channel. Moreover, we notice that the integration in time of the continuity equation used in the Figures 3.1(c) and 3.1(d) allows to take a bigger time step and prevents from losing volume compared to Figure 3.1(b).

3.1.2 Laminar case

Here, we are going to test the friction terms in a closed channel in the laminar case. We simulate a Poiseuille flow in a periodic pipe with a diameter of $1m$ at a Reynolds number of 10. The viscosity ν is set at $10^{-1}m^2.s^{-1}$ and a body force in the x-direction is used to fix the Reynolds number. The viscous term is modelled with the wall-corrected model of Morris (2.61) combined with (2.66) to compute the friction velocity. We can observe on the Figure 3.2 that the horizontal velocity profile is in good agreement with the analytical solution (2.93) even in the vicinity of the wall, which means that the wall shear stress well balances the body force.

3.1.3 Turbulent case

We perform here the same simulation as in the previous section 3.1.2, but in a turbulent case. Indeed the diameter is still $1m$ and the body force in the x-direction is $8.10^{-3}m.s^{-2}$ whereas the laminar viscosity is $10^{-6}m^2.s^{-1}$. This corresponds to a Reynolds number of about 2.10^6. The wall modified $k-\epsilon$ model is in appendix A.1.1.

In Figure 3.3, we notice that the expected logarithmic region on the mean velocity next to the wall is well reproduced. The computation of S thanks to (2.90) and ϵ, which are expected to be both in $\frac{1}{z}$ are satisfactory reproduced next to the wall. However, the periodic flow in the pipe created density variation as we can notice in Figure 3.3 where the x-direction is stretched. This small variation in the density field produces a wave with a resonance mode. This wave implies vertical displacement of particles which is responsible for the large values of S in the middle of the pipe (where S is expected to be 0 because of symmetry reasons). Thus, the production

of P of kinematic energy k is overestimated in the middle of the Pipe.

If we compute S thanks to Equation (2.92) then the density wave still exists (see Figure 3.4), and so the strain strain is still perturbed in the middle of the channel even if the error is smaller. As recommended in the conclusions, more research should be conducted into this phenomenon.

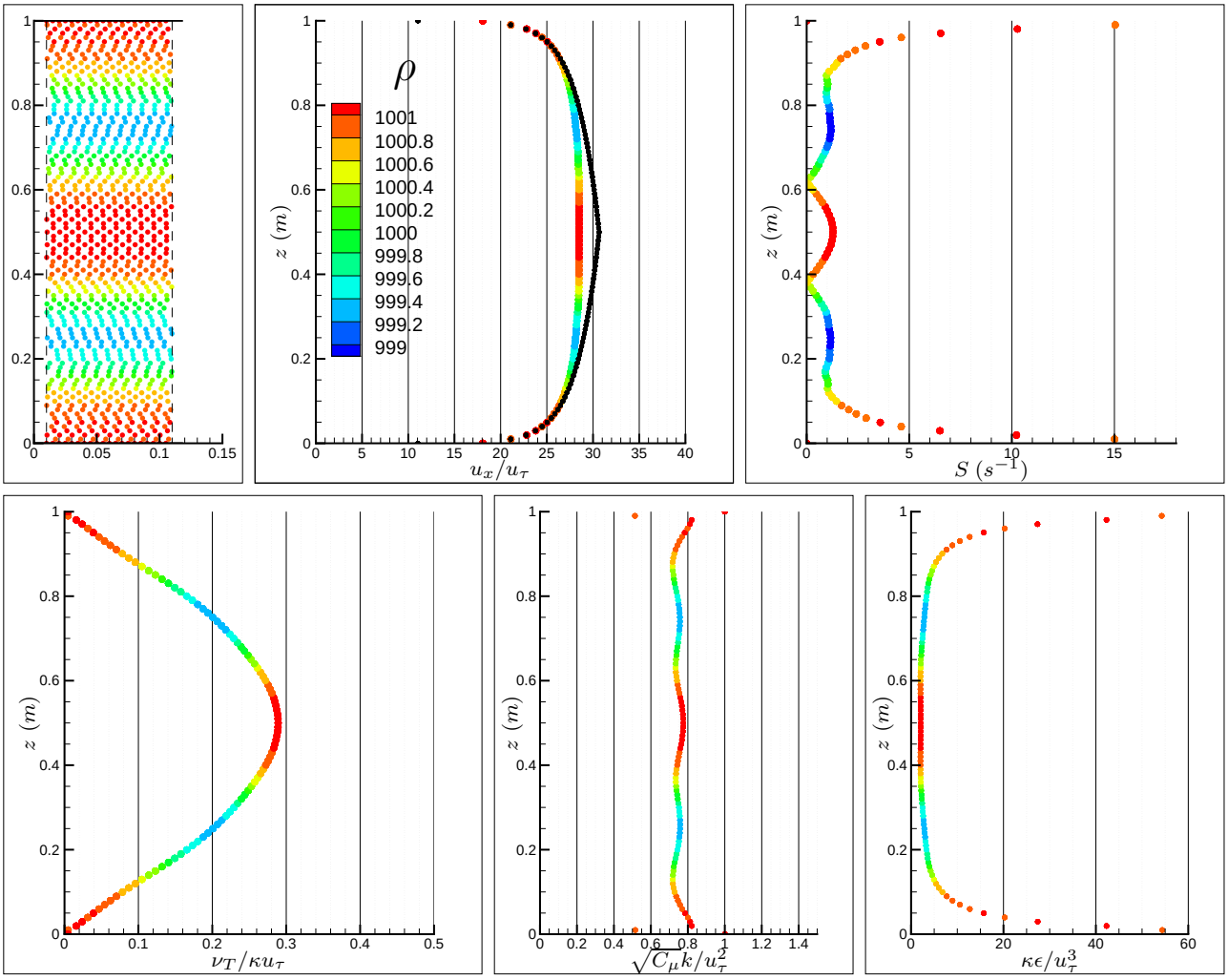

Figure 3.3: Various profiles in a turbulent pipe. The strain rate S computed thanks to (2.90) is perturbed by the density wave.

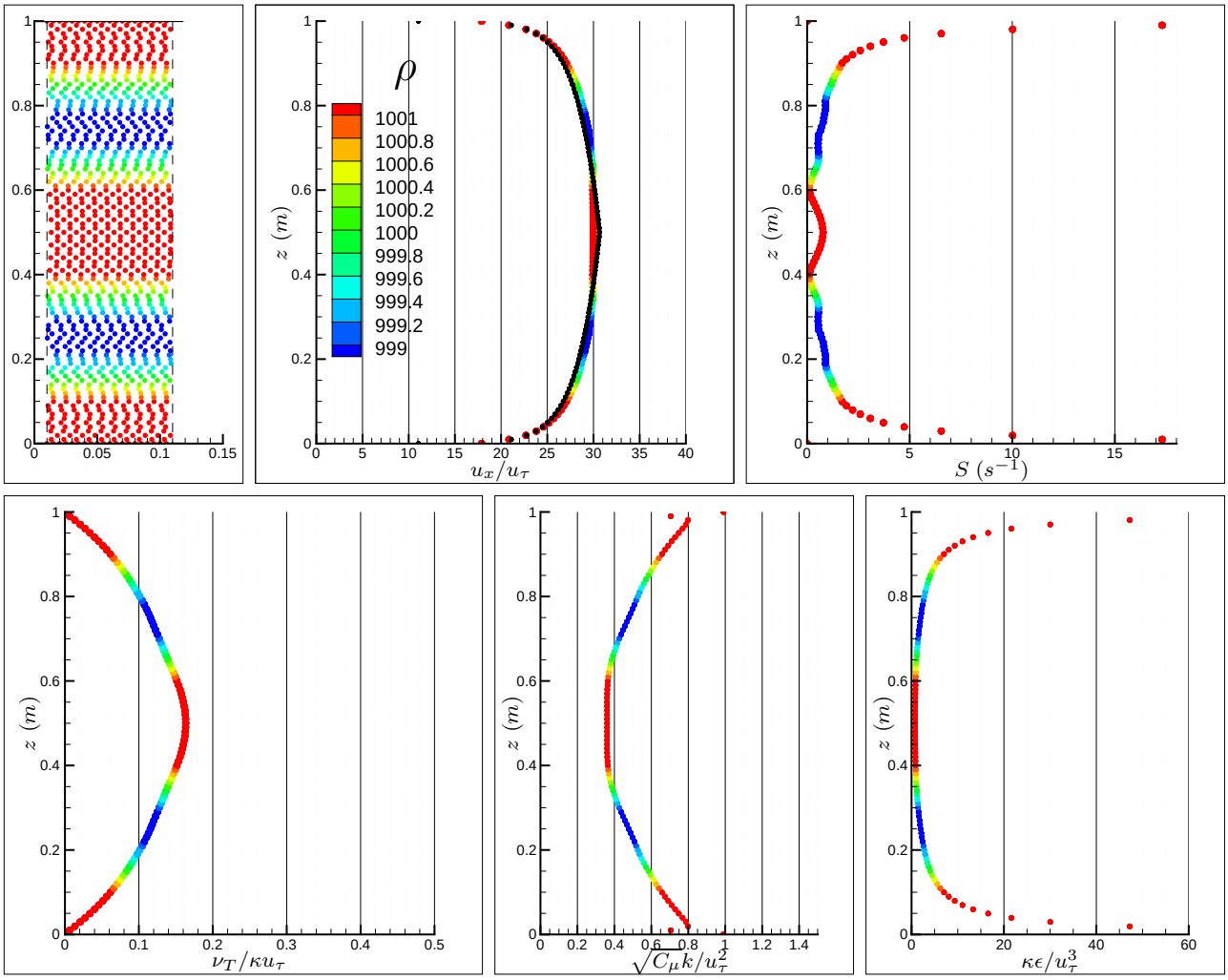

Figure 3.4: Various profiles in a turbulent pipe. The strain rate S computed thanks to (2.92) is still perturbed by the density wave.

3.2 Still water and dam break in a tank with a wedge

In this section, we focus on a more complex geometry: a basin of approximately $2m$ length and $1m$ height with a wedge of $\frac{\pi}{2}\,rad$ angle and $\frac{\sqrt{2}}{8}m$ of height in the bottom middle of the tank. A comparison is made between different models in a still water case and a dynamic case.

3.2.1 Still water case

Some of the developments to treat the solid boundaries suffer from an inability to reproduce correctly a still water case. Here we compare the results obtained when the basin is filled with $0.5m$ of water for the Lennard-Jones repulsive forces (see Monaghan [24]), the fictitious particles method (see Violeau and Issa [34]) and our method. As expected, the repulsive forces give the worst results (see the Figures 3.5(b)) in the sense that particles keep sliding along vertical wall. That is due to the fact that the missing area in the kernel support is not compensated, and thus the gravity is not balanced sufficiently. The plot of the pressure of particles against the depth is therefore noisy and badly reproduced next to the bottom. The fictitious particles method (see Figure 3.5(a)) gives better results, but the condition (2.16) is not ensured and so the pressure profile is still noisy. Moreover this approach is problematic to describe in complex geometries and requires additive particles to mimic the boundary, which increase the computation cost. The present method gives superior results: a linear pressure profile even near the bottom and a zero velocity field.

3.2.2 Dynamic case

A simulation of a dam break with the same specific shape of the boundary has been performed for the two methods previously described and the present one. The water is initially a column of $1m$ height and $0.5m$ width on the left side of the basin. We can notice on the Figure 3.6 that all ensure impermeable boundaries, but both of repulsive forces method and fictitious particles method give a noisier pressure field. Furthermore, a refinement has been computed by doubling the number of particles (and dividing the initial space between two particles from $\delta r = \frac{1}{100}$ to $\frac{\delta r}{2}$). Snapshots of the pressure field at the same physical time are plotted on the Figure 3.6.

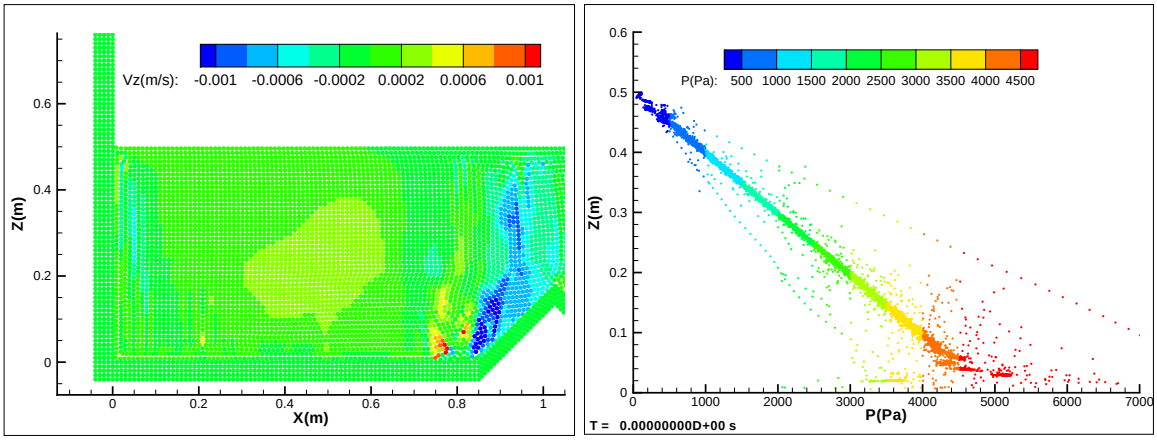

(a) Fictitious particles.

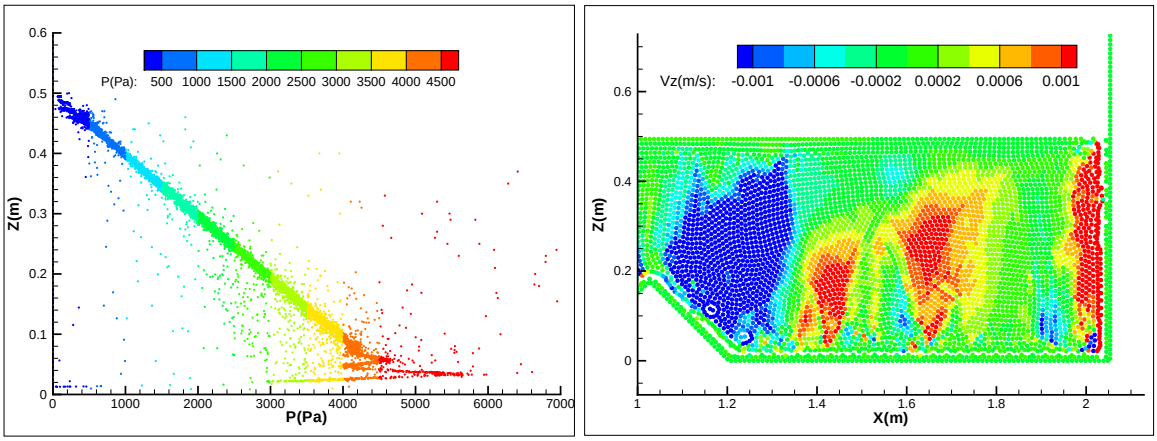

(b) Lennard-Jones type repulsive force.

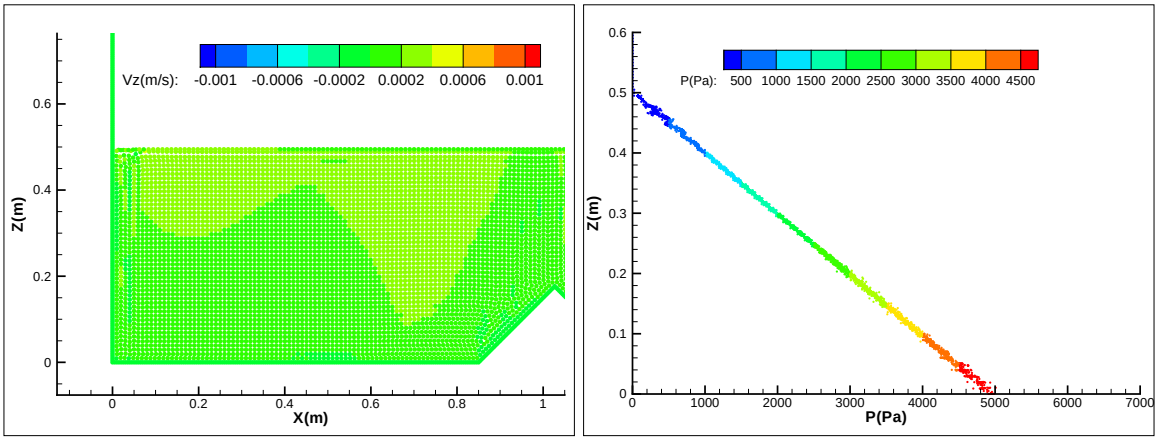

(c) Present method.

Figure 3.5: Comparison of the vertical velocity for still water in a tank with a wedge for different boundary conditions after 20s.

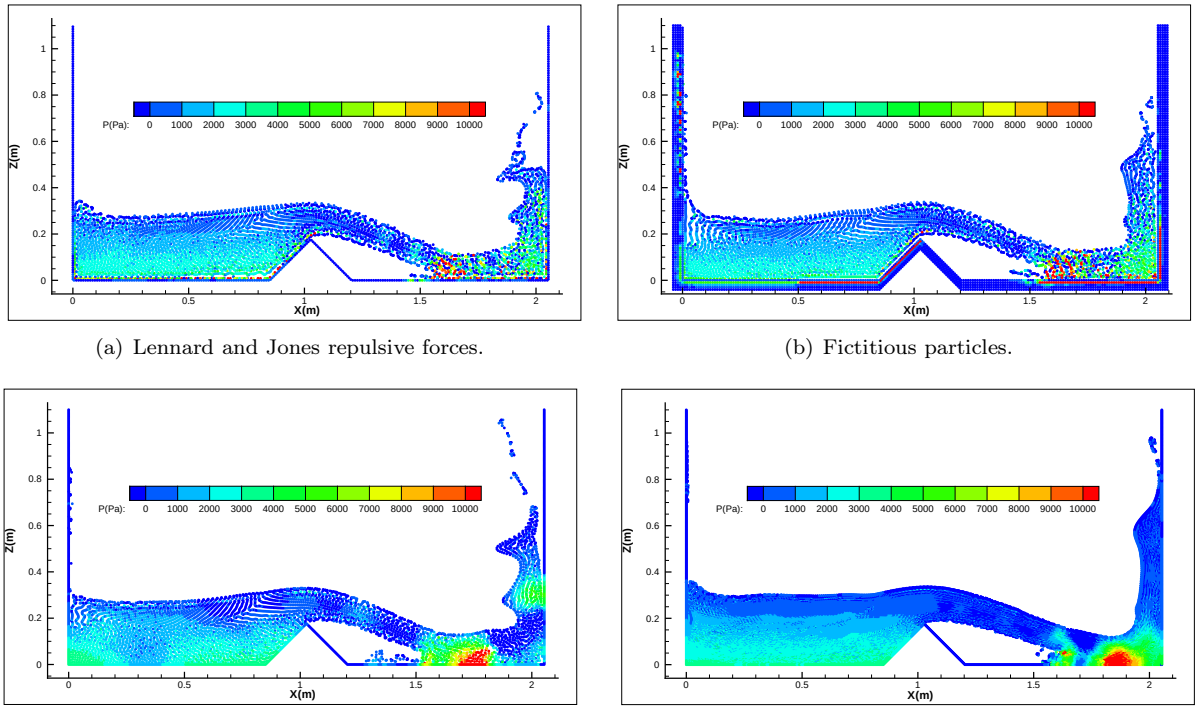

(a) Lennard and Jones repulsive forces.

(b) Fictitious particles.

(c) Present method.

(d) Present method with a twice smaller space discretization.

Figure 3.6: Comparison of the pressure field for a dam break test case in a tank with a wedge for different boundary conditions.

3.3 $2D$ Flow around a moving square inside a rectangular box

We have tested the present method with the *SPHERIC* benchmark $2D$ *Incompressible flow around a moving square inside a rectangular box* (see [3]). A square cylinder with sides of one meter is moving in a basin with a length of $10m$ and a width of $5m$. The velocity of the moving square is progressively forced to be $1m.s^{-1}$. In Figure 3.7, the magnitude of the velocity field is compared to a Finite Differences simulation at different instants with a good agreement. The method for taking into account the shear stress at the wall is not presented here.

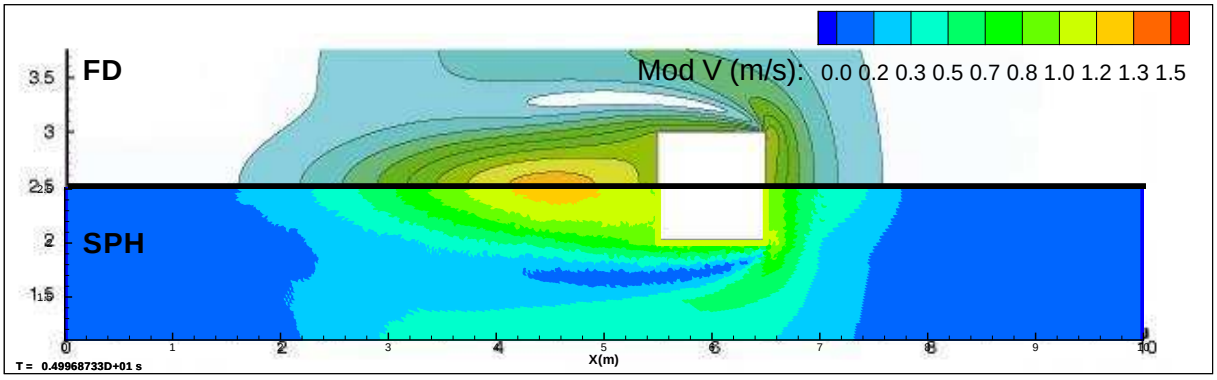

(a) Comparison after $5s$.

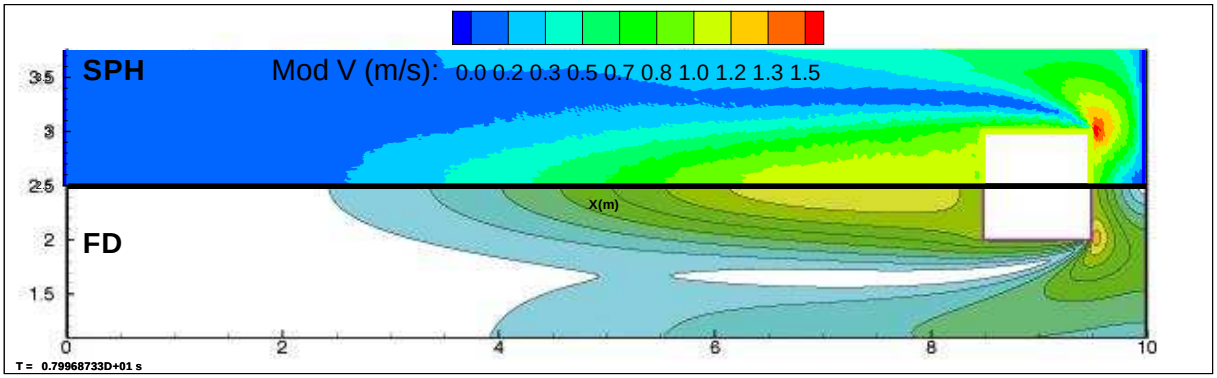

(b) Comparison after $8s$.

Figure 3.7: Comparison of the velocity magnitude field for a moving square cylinder in a basin between a finite differences code and the present *SPH* formulation for a Reynolds number of $Re = 50$. The spatial discretization is 400×200 particles.

3.4 Simulation of a fish pass

Once a dam is built on a river, the continuity of the flow is disrupted and the migration of fishes is stopped. For some species such as some salmons, the cycle of life requires the fishes to migrate far upriver. To restore the migration process, fish passes are installed. They are composed of many blocs which could be compared to stairs. The dimensioning of these components requires a good knowledge of the turbulent flow within this construction, which can be assimilated as a periodic flow, making each element effectively identical. We need of course to know the current strength, a too large current would prevent fish to swim upstream. Hence, we must know how turbulence is established. Indeed, the size of the large eddies affects the fish's swim.

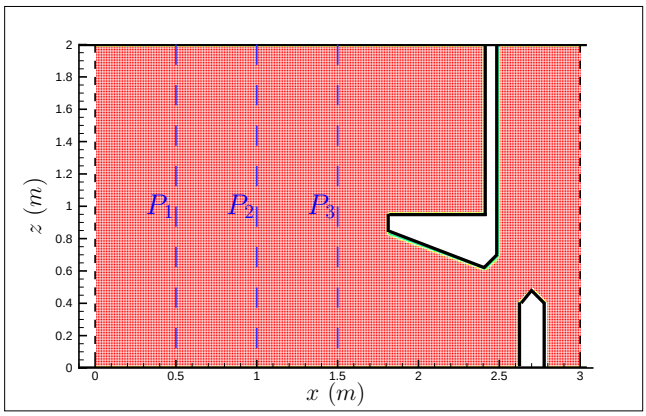

Figure 3.8: Sketch of the geometry of the periodic fish pass. In blue the three plans where measured are carried out.

Although the behaviour of the flow though a fish pass is a $3D$ free surface flow, we consider here $2D$ simulations where the vertical variation are assumed to be negligible. We repeat here the simulations presented in Violeau *et al.* [35]. The geometry of the $x-$periodic simulation is presented in Figure 3.8.

We have tested two different models: (i) a laminar viscosity $\nu = 0.03m^2.s^{-1}$, and (ii) a $k-\epsilon$ model with a laminar viscosity of $\nu = 1.10^{-6}m^2.s^{-1}$.

The reproduction of the velocity field compared to results obtained with *TELEMAC-2D* are satisfactory (see Figure 3.9).

The velocity profiles in P_1, P_2 and P_3 defined in Figure 3.8 and plotted in Figure 3.10 are comparable to those obtained by *CODE_SATURN* in [35]. We can notice that we better reproduce it with the $k-\epsilon$ model in the plan $P3$. The satisfactory point is that the mesh-based code gives results really next to the ones obtained with the present version of *SPARTACUS-2D*. Moreover, the profiles of turbulent kinetic energy presented in Figure 3.11 reinforce the the fact that both *SPARTACUS-2D* and *CODE_SATURN* give comparable results which are not in good agreement with the measurements.

If we investigate more carefully the result of the $k-\epsilon$ model presented in Figure 3.12, we can consider the use of a $2D$ version of the $k-\epsilon$ model to be probably irrelevant. Indeed, by using a $2D$ model, we implicitly assume that there is no variation of the mean velocity field in the span-wise direction (and then the strain rate in $2D$ is the same than in $3D$). However the fish pass is around $1m$ depth, and the velocity magnitude reach $3m.s^{-1}$ and the production of kinetic energy next to the bottom of the fish pass cannot be neglected. That is why the turbulent viscosity is not big enough in the area where $|\overline{\mathbf{u}}|$ is large and then the velocity profile in P_1 in Figure 3.10(a) is too sharp.

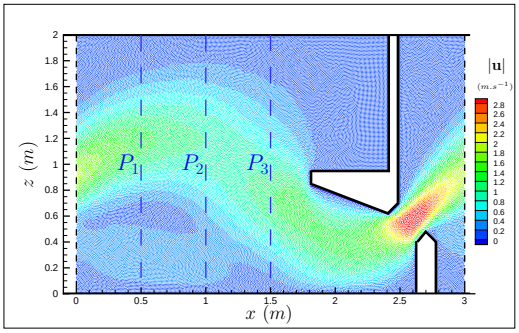

(a) Laminar viscosity $\nu = 0.03m^2.s^{-1}$ with *SPARTACUS-2D*.

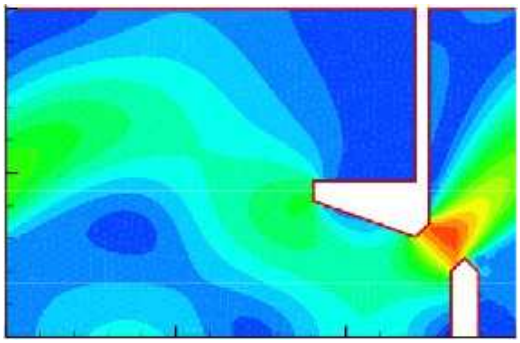

(b) $k-\epsilon$ model with *TELEMAC-3D* carried out by Violeau *et al.* [35].

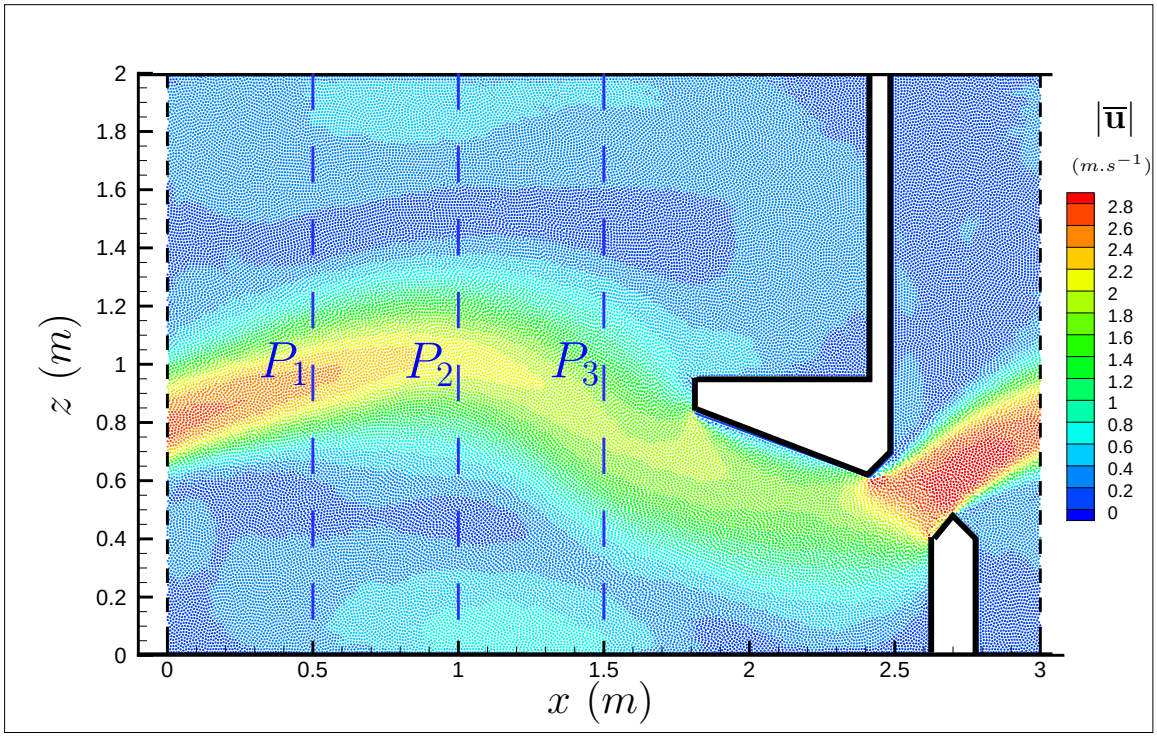

(c) Present version of the $k-\epsilon$ model with *SPARTACUS-2D*.

Figure 3.9: Velocity magnitude field in a fish pass: comparison between *TELEMAC-3D* and *SPARTACUS-2D*.

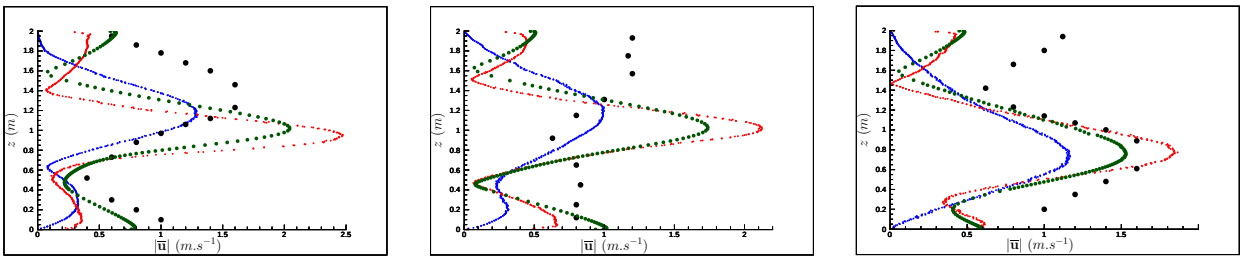

(a) Profiles in P_1. (b) Profiles in P_2. (c) Profiles in P_3.

Figure 3.10: Profiles of the velocity magnitude in three different plans in the fish pass.The $k-\epsilon$ model (2.82) in red, the constant viscosity model in blue and a $k-\epsilon$ model with *CODE_SATURN* in green whereas black dots represent the measures.

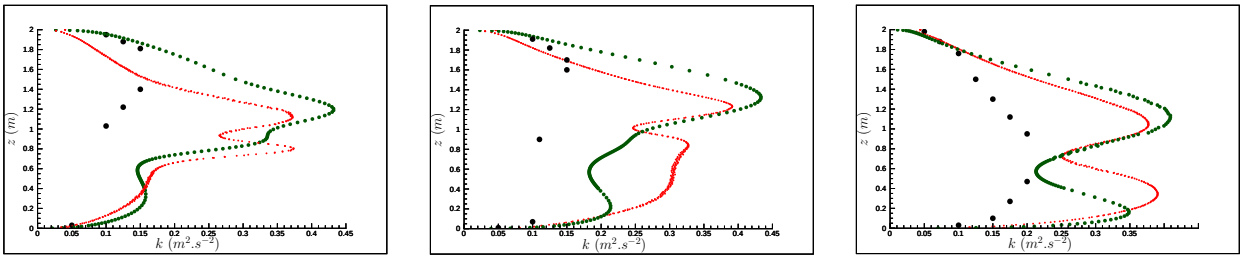

(a) Profiles in P_1. (b) Profiles in P_2. (c) Profiles in P_3.

Figure 3.11: Profiles of the turbulent kinetic energy k in three different plans in the fish pass.The $k-\epsilon$ model (2.82) in red and a $k-\epsilon$ model with *CODE_SATURN* in green whereas black dots represent the measures.

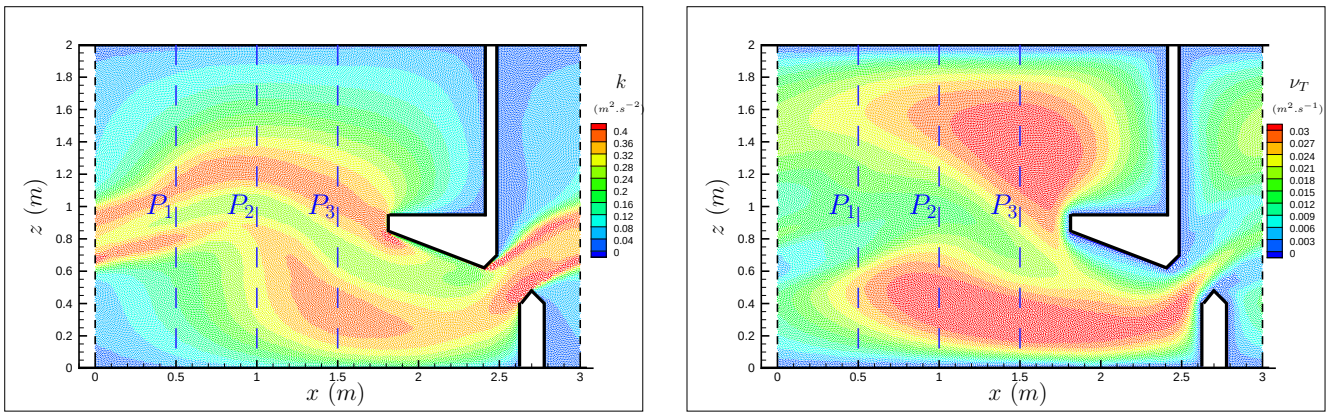

(a) Kinetic energy k . (b) Turbulent viscosity ν_T.

Figure 3.12: Kinetic energy and turbulent viscosity fields of the $k-\epsilon$ model with present version of *SPARTACUS-2D*.

Chapter 4

Conclusion and recommendations for future research

This report has presented a new approach to deal with solid boundary conditions which is both simple and robust. The simplicity lies in the manner we compute the Eulerian renormalization term γ_a with an integration in time which only requires the computation of its gradient $\boldsymbol{\nabla}\gamma_a$. The robustness is due to the integration in time of the continuity equation which makes the density field depend only on the particles' positions. This allows long time simulations with a relatively larger time step and is a major advantage for conservation properties.

The definition of new boundary corrected *gradient* and *laplacian* operators gives us the opportunity to fix boundary conditions and fluxes on the pressure field, the wall shear stress and even the scalar fields such as k and ϵ in a turbulence model.

However, numerous issues still require investigation and development, namely:

(*i*) Validate the present formulation on different test cases such as a periodic turbulent bump.

(*ii*) Adapt the wall renormalization to $3D$; the main challenge is to find an analytical formula for the computation of the contribution of a surface element s over the value of $\boldsymbol{\nabla}\gamma_a$ of a fluid particle a (which is denoted by $\boldsymbol{\nabla}\gamma_{as}$), or a way to compute accurately an approximated value of it.

(*iii*) Study the theoretical conservation (or non-conservation) of momentum and angular momentum, and especially in periodic cases.

(*iv*) Combine the present approach with non-periodic entrance conditions.

Appendix A

Appendices

A.1 Modifications in *SPARTACUS-2D*

This section aims at listing all the modifications done in *SPARTACUS2D* to code the present approach to compute every terms of the renormalization.

The routines created or modified are classified in three subsections: the new routines, the widely adapted routines and finally routines where occur just few changes.

A.1.1 Reminder of equations solved in *SPARTACUS-2D*

The following are the equations solved by *SPARTACUS-2D*. They concern only the turbulent case, as the laminar case is formally identical, with average variables that coincide with the real variables, while the eddy viscosity is constant and equal to the molecular kinematic viscosity. Furthermore the Lagrangian derivative $\frac{\mathrm{D}}{\mathrm{D}t} \equiv \frac{\partial}{\partial t} + \overline{\mathbf{u}}.\boldsymbol{\nabla}$ would be replaced by $\frac{\mathrm{d}}{\mathrm{d}t} \equiv \frac{\partial}{\partial t} + \mathbf{u}.\boldsymbol{\nabla}$.

Continuity equation

$$\rho_a \left[\beta\gamma_a + (1-\beta)\,\alpha_a\right] = \tilde{\rho}_a = \sum_{b\,\in\,\mathcal{F}} m_b w_{ab} \tag{2.35}$$

where

$$\beta = \exp\left[-K\left(\min\left\{\frac{\alpha_a}{\gamma_a};\,1\right\} - 1\right)^2\right] \tag{2.36}$$

and $K = 30000$. β could be 1 everywhere for confined flows.

Shepard filter α

$$\alpha_a \equiv \sum_{b\,\in\,\mathcal{F}} \frac{m_b}{\rho_b} w_{ab} \tag{2.33}$$

$$\begin{aligned} \alpha_e &\equiv \sum_{b\,\in\,\mathcal{F}\setminus\mathcal{E}} \frac{m_b}{\rho_b} w_{eb} \\ \alpha_s &\equiv \sum_{b\,\in\,\mathcal{F}\setminus\mathcal{E}} \frac{m_b}{\rho_b} w_{sb} \end{aligned} \tag{2.34}$$

Governing equation for γ

$$\begin{aligned} \frac{\mathrm{D}\gamma_a}{\mathrm{D}t} &= \sum_{s\,\in\,\mathcal{S}} \boldsymbol{\nabla}\gamma_{as}.\mathbf{u}_a^{\mathcal{R}_s} \\ \gamma_a &= 1 \qquad\qquad \text{if } \partial\Omega \cap \Omega_a = \emptyset \end{aligned} \tag{2.50}$$

Analytical value of $\boldsymbol{\nabla}\gamma_{as}$ for the quintic kernel (1.24)

$$\boldsymbol{\nabla}\gamma_{as} \equiv \left(\int_{\mathbf{r}_{e1}}^{\mathbf{r}_{e2}} w\,(r)\,\mathrm{d}l\right)\mathbf{n}_s \tag{2.8}$$

with

$$\begin{aligned} \int_{\mathbf{r}_{e1}}^{\mathbf{r}_{e2}} w\,(r)\,\mathrm{d}l &= \frac{(q_2\cos\alpha_2)}{\pi} P_{q_0}\,(q_2) - \frac{(q_1\cos\alpha_1)}{\pi} P_{q_0}\,(q_1) \\ &\quad + \frac{q_0^4}{\pi}\left(\frac{105}{64} + \frac{35}{512}q0^2\right)\left[\begin{array}{l} \mathtt{sign}\,(q_2\cos\alpha_2)\ln\left(\dfrac{q_2 + |q_2\cos\alpha_2|}{|q0|}\right) \\ -\mathtt{sign}\,(q_1\cos\alpha_1)\ln\left(\dfrac{q_1 + |q_1\cos\alpha_1|}{|q0|}\right) \end{array}\right] \end{aligned} \tag{2.44}$$

where:

$$\begin{aligned} P_{q_0}(q) &= \frac{7}{192}q^5 - \frac{21}{64}q^4 + \frac{35}{32}q^3 - \frac{35}{24}q^2 + \frac{7}{4} \\ &\quad + q_0^2\left(\frac{35}{768}q^3 - \frac{7}{16}q^2 + \frac{105}{64}q - \frac{35}{12}\right) \\ &\quad + q_0^4\left(\frac{35}{512}q - \frac{7}{8}\right) \end{aligned} \tag{2.45}$$

Momentum equation

$$\begin{aligned} \frac{\mathrm{D}\overline{\mathbf{u}}_a}{\mathrm{D}t} &= -\frac{1}{\rho_a}\widetilde{\mathbf{Grad}}_a\{p_b + \tfrac{2}{3}k_b\} + \mathbf{g} \\ &\quad + \frac{1}{\rho_a}\boldsymbol{\nabla}.\left(\mu\boldsymbol{\nabla}\,\overline{\mathbf{u}}\right)_a \end{aligned} \tag{A.1}$$

Pressure *gradient*

$$\widetilde{\mathbf{Grad}}_a\{p_b\} \equiv \frac{\rho_a}{\gamma_a}\sum_{b\,\in\,\mathcal{F}} m_b\left(\frac{p_a}{\rho_a^2} + \frac{p_b}{\rho_b^2}\right)\boldsymbol{\nabla}w_{ab} - \frac{\rho_a}{\gamma_a}\sum_{s\,\in\,\mathcal{S}}\left(\frac{p_a}{\rho_a^2} + \frac{p_s}{\rho_s^2}\right)\rho_s\boldsymbol{\nabla}\gamma_{as} \tag{2.13}$$

Boundary pressure term

$$\begin{aligned} \rho_e &= \frac{1}{\alpha_e}\sum_{b\,\in\,\mathcal{F}\setminus\mathcal{E}} V_b\rho_b w_{be} \\ \frac{p_e}{\rho_e} &= \frac{1}{\alpha_e}\sum_{b\,\in\,\mathcal{F}\setminus\mathcal{E}} V_b\left(\frac{p_b}{\rho_b} - \mathbf{g}.\left(\mathbf{r}_b - \mathbf{r}_e\right) + \frac{u_{be}^2}{2}\right) \end{aligned} \tag{2.18}$$

$$\begin{aligned} \rho_s &= \frac{\rho_{e1} + \rho_{e2}}{2} \\ \frac{p_s}{\rho_s} &= \frac{p_{e1}/\rho_{e1} + p_{e2}/\rho_{e2}}{2} \end{aligned} \tag{2.20}$$

where the edge particles $e1$ and $e2$ are defined in §2.1.2.

Morris' viscous term

$$\frac{1}{\rho_a}\boldsymbol{\nabla}.\left(\mu\boldsymbol{\nabla}\,\overline{\mathbf{u}}\right)_a = \frac{1}{\gamma_a}\sum_{b\,\in\,\mathcal{F}} m_b\frac{\mu_a + \mu_b}{\rho_a\rho_b}\frac{\overline{\mathbf{u}}_{ab}}{r_{ab}^2}\mathbf{r}_{ab}.\boldsymbol{\nabla}w_{ab} - \frac{2u_{\tau a}\mathbf{u}_{\tau a}}{\gamma_a}\sum_{s\,\in\,\mathcal{S}}|\boldsymbol{\nabla}\gamma_{as}| \tag{A.2}$$

Velocity of wall particles for turbulent flows

$$\frac{\mathrm{D}\overline{\mathbf{u}}_e}{\mathrm{D}t} = \frac{1}{\gamma_e}\sum_{b\,\in\,\mathcal{F}} m_b\frac{\mu_{Te} + \mu_{Tb}}{\rho_e\rho_b}\frac{\overline{\mathbf{u}}_{eb}}{r_{eb}^2}\mathbf{r}_{eb}.\boldsymbol{\nabla}w_{eb} - \frac{2u_{\tau e}\mathbf{u}_{\tau e}}{\gamma_e}\sum_{s\,\in\,\mathcal{S}}|\boldsymbol{\nabla}\gamma_{es}| \tag{2.95}$$

$$\overline{\mathbf{u}}_s = \frac{\overline{\mathbf{u}}_{e1} + \overline{\mathbf{u}}_{e2}}{2} \tag{2.96}$$

Laminar friction velocity

$$u_{\tau a}\mathbf{u}_{\tau a} = \frac{\nu\mathbf{u}_a}{z_a} \tag{2.66}$$

Smooth turbulent friction velocity

$$\frac{\overline{\mathbf{u}}_a}{u_{\tau a}} = \frac{1}{\kappa}\ln\left(\frac{z_a u_{\tau a}}{\nu}\right) + 5.2 \tag{2.88}$$

Wall friction velocity

$$\rho_e u_{\tau e} \mathbf{u}_{\tau e} = \frac{1}{\alpha_e} \sum_{b \in \mathcal{F} \setminus \mathcal{E}} V_b \rho_b u_{\tau b} \mathbf{u}_{\tau b} w_{be} \tag{2.67}$$

$$\rho_s u_{\tau s} \mathbf{u}_{\tau s} = \frac{\rho_{e1} u_{\tau e1} \mathbf{u}_{\tau e1} + \rho_{e2} u_{\tau e2} \mathbf{u}_{\tau e2}}{2} \tag{2.68}$$

Equation of motion

$$\frac{\mathrm{D}\mathbf{r}_a}{\mathrm{D}t} = \overline{\mathbf{u}}_a \tag{A.3}$$

$$\begin{aligned} \frac{\mathrm{D}\mathbf{r}_e}{\mathrm{D}t} &= \text{velocity of the wall} \\ \frac{\mathrm{D}\mathbf{r}_s}{\mathrm{D}t} &= \text{velocity of the wall} \end{aligned} \tag{A.4}$$

Equation of state

$$p_a = \frac{\rho_0 c_0^2}{\gamma} \left[\left(\frac{\rho_a}{\rho_0} \right)^\gamma - 1 \right] \tag{1.4}$$

Eddy viscosity

$$\nu_T = C_\mu \frac{k^2}{\epsilon} \tag{2.81}$$

$k - \epsilon$ model

$$\begin{aligned} \frac{\mathrm{D}k_a}{\mathrm{D}t} &= \frac{1}{\rho_a} \boldsymbol{\nabla}_a . \left[\left(\mu + \frac{\mu_T}{\sigma_k} \right) \boldsymbol{\nabla} k \right] + P_a - \epsilon_a \\ \frac{\mathrm{D}\epsilon_a}{\mathrm{D}t} &= \frac{1}{\rho_a} \boldsymbol{\nabla}_a . \left[\left(\mu + \frac{\mu_T}{\sigma_\epsilon} \right) \boldsymbol{\nabla} \epsilon \right] + \frac{\epsilon_a}{k_a} \left(C_{\epsilon 1} P_a - C_{\epsilon 2} \epsilon_a \right) \end{aligned} \tag{2.82}$$

Diffusion terms

$$\frac{1}{\rho_a} \boldsymbol{\nabla} . \left[\left(\mu + \frac{\mu_T}{\sigma_k} \right) \boldsymbol{\nabla} k \right]_a = \frac{1}{\gamma_a} \sum_{b \in \mathcal{F}} m_b \frac{2\mu + \mu_{Ta}/\sigma_k + \mu_{Tb}/\sigma_k}{\rho_a \rho_b} \frac{k_{ab}}{r_{ab}^2} \mathbf{r}_{ab} . \boldsymbol{\nabla} w_{ab} \tag{2.99}$$

$$\frac{1}{\rho_a} \boldsymbol{\nabla} . \left[\left(\mu + \frac{\mu_T}{\sigma_\epsilon} \right) \boldsymbol{\nabla} \epsilon \right]_a = \frac{1}{\gamma_a} \sum_{b \in \mathcal{F}} m_b \frac{2\mu + \mu_{Ta}/\sigma_\epsilon + \mu_{Tb}/\sigma_\epsilon}{\rho_a \rho_b} \frac{\epsilon_{ab}}{r_{ab}^2} \mathbf{r}_{ab} . \boldsymbol{\nabla} w_{ab} + \frac{4}{\gamma_a \rho_a} \sum_{s \in \mathcal{S}} |\boldsymbol{\nabla} \gamma_{as}| \, \rho_s \frac{u_s^{\star 4}}{\sigma_\epsilon \kappa \delta_{as}} \tag{2.105}$$

Boundary terms

$$\begin{aligned} k_e &= \frac{u_{\tau e}^2}{\sqrt{C_\mu}} \\ k_s &= \frac{u_{\tau s}^2}{\sqrt{C_\mu}} \\ u_s^\star &= u_{\tau s} \end{aligned} \tag{2.107}$$

Production

$$P_a = \nu_{Ta} S_a^2 \tag{2.84}$$

Strain rate

$$S^2 \equiv 2\mathbf{S} : \mathbf{S} \tag{2.85}$$

with

$$\boldsymbol{\nabla}_a \overline{\mathbf{u}} = -\frac{1}{\gamma_a \rho_a} \sum_{b \in \mathcal{F}} m_b \overline{\mathbf{u}}_{ab} \otimes \boldsymbol{\nabla} w_{ab} + \frac{1}{\gamma_a} \sum_{s \in \mathcal{S}} \overline{\mathbf{u}}_{as} \otimes \boldsymbol{\nabla} \gamma_{as} \tag{2.90}$$

or

$$\nu_{Ta} S_a^2 = -\frac{1}{2\gamma_a} \sum_{b \in \mathcal{F}} m_b \frac{\mu_{Ta} + \mu_{Tb}}{\rho_a \rho_b} \frac{\overline{u}_{ab}^2}{r_{ab}^2} \mathbf{r}_{ab} . \boldsymbol{\nabla} w_{ab} - \frac{2}{\gamma_a} \sum_{s \in \mathcal{S}} u_{\tau s}^2 \overline{u}_{as} \, |\boldsymbol{\nabla} \gamma_{as}| \tag{2.92}$$

A.1.2 New routines

`alpha.f` **Aim:** Compute the Shepard filter α (see Equations (2.33; 2.34)). The renormalization matrix is also coded, if needed.

Called by: `SPARTACUS2D`

Remark: For edge particles and for the middle of boundary areas, the edge particles are not taken into account in the sum.

`gamma.f` **Aim:** Compute γ_a thanks to (2.50), $\boldsymbol{\nabla}\gamma_a$ and $\tilde{\rho}_a$ sorted respectively in the arrays `GAM_A`, `GGAM_AX` and `GGAM_AZ`, and `RHOMF`.

Called by: `CONTINUITE`, `INITGAMMA`

Call: `KERNEL4_VAL` or `KERNELW_VAL`, `INTKERNEL`

Remark: We use a second order integration in time for γ_a. For edge particles, $\tilde{\rho}_e$ does not take into account the other edge particles.

`impulsion_nu.f` **Aim:** Compute the forces due to the viscous forces (A.2).

Called by: `SPARTACUS2D`

Call: `FLUXVISQ` and `VISCTURB`.

Remark: Part of the old `impulsion.f` routine, this routine is used to separate the conservative forces to viscous forces to allow a temporal scheme where the viscous forces are semi-implicit. The acceleration takes the boundary terms and the renormalization into account.

`impulsion_p.f` **Aim:** Compute the forces due to the pressure and the body forces (2.13).

Called by: `SPARTACUS2D`

Call: `FORCPAROIS`, `FORCEXT` and `FLUXPRES`

Remark: Part of the old `impulsion.f` routine, this routine is used to separate the conservative forces to viscous forces to allow a temporal scheme where the viscous forces are semi-implicit. The acceleration takes the boundary terms and the renormalization into account.

`initgamma.f` **Aim:** Initialize the value of γ_a by imaging a virtual transformation (see §2.3).

Called by: `SPARTACUS2D`

Call: `TABLIEN` and `GAMMA`

Remark: The virtual sample path of the particles for which we compute the original value of γ_a is a segment. More complex sample path could be considered, but it is not coded.

`intbord.f` **Aim:** Compute the boundary terms of the gradient of pressure (2.13) thanks to (2.18) and (2.20) which are stored in the arrays `BP_AX`, `BP_AZ`, `BRHO_AX` and `BRHO_AX`.

Called by: `SPARTACUS2D`

Remark: Different ways to compute the pressure and the density at the wall could be done.

`intbordnu.f` **Aim:** Compute the boundary terms of viscous term (A.2) in the momentum equation which are stored in the arrays `BNU_AX`, `BNU_AZ`, and `BNU_A`.

Called by: `SPARTACUS2D`

Remark: The array `BNU_A` is used if we want to implicit the wall shear stress.

`intkernel.f` **Aim:** Compute the norm of $\boldsymbol{\nabla}\gamma_{as}$ for the quintic kernel (see Equation 2.44) stored in the double array `INTKER`.

Called by: `GAMMA`

Remark: If the particle `J=ILIEN(I,L)` is a boundary area point (*ie* `KPAR(J)=2`), then `INTKER(I,L)` stores the value of $|\boldsymbol{\nabla}\gamma_{I,J}|$.

`kernelw.f` **Aim:** Compute the *gradient* of the Wendland quintic kernel (see Equation (1.24)).

Called by: `KERNEL`

Remark: To chose the Wendlandl kernel, you have to give `KKERNEL` the value 4.

`kernelw_val.f` **Aim:** Compute the values of the Wendland quintic kernel (see Equation (1.24)).

Called by: `GAMMA` if `KKERNEL` is 4.

`position.f` **Aim:** Compute the updated positions of the particles with the Equation (A.3).

Called by: `SPARTACUS2D`.

Remark: Part of the old `mouvement.f` routine, this routine is used to separate the update of velocities and positions to test other temporal schemes. The velocity used to update positions is `VXMOB` and `VZMOB`, which is the same as `VX` and `VZ` for particles of type 1 but can be different for the other particles if the flow is turbulent (because then we make a difference between the velocity used to compute viscous forces and the velocity used to update positions of wall particles).

`vitesse.f` **Aim:** Compute the updated velocities of the particles.

Called by: `SPARTACUS2D`.

Remark: Part of the old `mouvement.f` routine, this routine is used to separate the update of velocities and positions to test other temporal schemes.

`vitesse_nu.f` **Aim:** Compute the updated velocities of the particles where the shear stress at walls could be implicit.

Called by: `SPARTACUS2D`.

Remark: Part of the old `mouvement.f` routine, this routine is used to separate the update of velocities and positions to test other temporal schemes and allows to implicit the shear stress at walls.

A.1.3 Highly modified routines

`continuite.f` **Changes:** The new temporal scheme is used to compute the density field, and then the main part of the algorithm is done by the subroutine `gamma.f`. A correction for the free surface is added (see Equation (2.35)).

Called by: `SPARTACUS2D`

Call: `GAMMA`

Remark: The free surface correction is based on the Shepard filter α_a (see Equation 2.36).

`epsilon.f` **Changes:** The diffusion term (2.105) is corrected and the *YAP* correction is added.

Called by: `KEQUATION`

Remark: The diffusion term (2.99) is corrected.

`etat.f` **Changes:** Computes the pressure of edge particles e and points s thanks to Equations (2.18) and (2.20).

Called by: `SPARTACUS2D`

Remark: Allows to take a background pressure, which can be useful for confined flows.

`forcparois.f` **Changes:** Also computes the present repulsive force due to the boundary term of the gradient of pressure (see Equation (2.13)).

Called by: `IMPULSION_P`

Remark: The present repulsive force is computed if and only if `KFPAR` is equal to 4.

`frottement.f` **Changes:** Computes u_τ and the shear stress at the wall for edge particles.

Called by: `SPARTACUS2D`

Remark: The friction velocity $u_{\tau s}$ is computed thanks to the continuity of the stresses (see Equation (2.68)).

`gradvit.f` **Changes:** Computes *gradient* of the velocity field taking boundaries into account (see Equation (2.90)).

Called by: `SPARTACUS2D`

Remark: The corrected formula seems to be not accurate enough for turbulent flows where the strain rate is expected to be proportional to $\frac{1}{z}$ where z is the distance to the wall.

`kequation.f` **Changes:** Computes the equation of the turbulent kinetic energy k taking boundary renormalization into account. The dissipative terms are implicit.

Called by: `VISCTURB`

Call: `EPSILON`

Remark: The condition $\frac{\mathrm{d}k}{\mathrm{d}n} = 0$ is assumed to cancel the boundary term.

`lecdon_spartacus2d.f` **Changes:** Allocate directly the values of the parameters without reading the file containing the parameters.

Called by: `SPARTACUS2D`

Remark: Modified because we do not have the program `DAMOCLE`.

`pastemps.f` **Changes:** Add the new condition on the time step (2.55).

Called by: `SPARTACUS2D`

Remark: The new condition is to ensure that the integration in time of the governing equation of γ_a (2.50) is accurate enough.

`tauxdef.f` **Changes:** Add a new formula to compute the strain rate and the production of kinetic turbulent energy P_a taking boundaries into account (see Equation (2.92)).

Called by: `VISCTURB`

A.1.4 Slightly modified routines

`ecrit.f` **Changes:** Allows to write new variables such as γ_a and the components of $\boldsymbol{\nabla}\gamma_a$ for instance.

`fluxpres.f` **Changes:** Take the new type of particles 4 (edge particles) into account.

`fluxvisc.f` **Changes:** Take the new type of particles 4 (edge particles) into account.

`initial.f` **Changes:** Initialize the mass of particles of type 4 (edge particles) to be a fraction of $\rho_0 \delta r^2$. Particles of type 2 (middle of boundary areas) has a zero mass.

`lecinit.f` **Changes:** Allocate directly the values of the inward normal components, also allocate the surface of the particle of type 2 (middle of boundary areas). Store the value of `THETA` for each particle: for particle of type 4 this value is the fractional volume occupied by the edge particle.

`paroimobile.f` **Changes:** Gives the velocity used to update positions to each particles. This velocity is zero for particles of type 2 or 4 belonging to a motionless wall.

`sorpar.f` **Changes:** Also update the values new variables such as γ_a and α_a in case we have deleted some particles.

A.2 Derivation of the repulsive from a Lagrangian

The classical formalism of the Lagrangian states:

$$\frac{\mathrm{d}}{\mathrm{d}t}\left(\frac{\partial L}{\partial \mathbf{u}_a}\right) - \left(\frac{\partial L}{\partial \mathbf{r}_a}\right) = 0 \tag{A.5}$$

where the Lagrangian is defined by:

$$L\left(\mathbf{r}_a,\, \mathbf{u}_a\right) = E_{ke}\left(\mathbf{u}_a\right) - E_{int}\left(\mathbf{r}_a\right) - E_{ext}\left(\mathbf{r}_a\right) \tag{A.6}$$

The energies E_{ke}, E_{int} and E_{ext} are respectively the kinetic energy, the internal energy and the external energy. The kinetic energy is given by (A.7a). If the external forces are due to the gravitational field $\mathbf{g}$ the external energy is given by (A.7b) and for an adiabatic reversible process, the internal energy can be written as (A.7c)

$$E_{ke} = \frac{1}{2}\sum_{b\,\in\,\mathcal{F}} m_b \mathbf{u}_b^2 \tag{A.7a}$$

$$E_{ext} = -\sum_{b} m_{b\,\in\,\mathcal{F}} \mathbf{r}_b.\mathbf{g} \tag{A.7b}$$

$$E_{int} = \sum_{b} m_{b\,\in\,\mathcal{F}}\, e_{int}\left(\rho_b\right) \tag{A.7c}$$

and the energy accumulated per unit of mass e_{int} varies with the density ρ according (A.8).

$$p = \rho^2 \frac{\mathrm{d}e_{int}}{\mathrm{d}\rho} \tag{A.8}$$

Finally we define the density to be :

$$\begin{aligned} \rho(\mathbf{r}) &= \frac{\displaystyle\int_{\Omega} \sum_{b\,\in\,\mathcal{F}} m_b \delta\left(\mathbf{r}' - \mathbf{r}_b\right)\, w\left(\mathbf{r} - \mathbf{r}'\right) \mathrm{d}\mathbf{r}'}{\displaystyle\int_{\Omega} w\left(\mathbf{r} - \mathbf{r}'\right) \mathrm{d}\mathbf{r}'} \\ &= \frac{\displaystyle\sum_{b\,\in\,\mathcal{F}} m_b\, w\left(\mathbf{r} - \mathbf{r_b}\right)}{\displaystyle\int_{\Omega\cap\Omega_r} w\left(\mathbf{r} - \mathbf{r}'\right) \mathrm{d}\mathbf{r}'} \end{aligned} \tag{A.9}$$

Hence it follows:

$$\gamma\left(\mathbf{r}\right)\, \rho\left(\mathbf{r}\right) = \sum_{b} m_b\, w\left(\mathbf{r} - \mathbf{r_b}\right) \tag{A.10}$$

which is a continuous function of the position $\mathbf{r}$ and gives us a way to compute the value of $\rho_a \equiv \rho\left(\mathbf{r}_a\right)$ if we know the positions of all particles.

Now we are able to derive the momentum equation from the equation of Lagrange (A.5) and obtain for each particle a:

$$m_a \frac{\mathrm{d}\mathbf{u}_a}{\mathrm{d}t} = \mathbf{F}_a^p + \mathbf{F}_a^B + m_a g \tag{A.11}$$

where the internal forces due to the pressure $\mathbf{F}_a^p$ and due to the boundary effect $\mathbf{F}_a^B$ are defined by (2.6).

Indeed we have:

$$\begin{aligned}\mathbf{F}_a^p + \mathbf{F}_a^B &= -\frac{\partial E_{int}}{\partial \mathbf{r}_a} \\ &= -\frac{\partial}{\partial \mathbf{r}_a}\left[\sum_{b\in\mathcal{F}} m_b\, e_{int}\left(\rho_b\right)\right] \\ &= -\sum_{b\in\mathcal{F}} m_b \frac{\mathrm{d}e_{int}}{\mathrm{d}\rho_b}\frac{\mathrm{d}\rho_b}{\mathrm{d}\mathbf{r}_a} \\ &= -\sum_{b\in\mathcal{F}} m_b \frac{p_b}{\rho_b^2}\frac{\mathrm{d}\rho_b}{\mathrm{d}\mathbf{r}_a}\end{aligned} \tag{A.12}$$

but we can derive the density using its definition (A.10):

$$\begin{aligned}\frac{\mathrm{d}\left(\gamma_b\rho_b\right)}{\mathrm{d}\mathbf{r}_a} &= \gamma_b\frac{\mathrm{d}\rho_b}{\mathrm{d}\mathbf{r}_a} + \rho_b\frac{\mathrm{d}\gamma_b}{\mathrm{d}\mathbf{r}_a} &&= \gamma_b\frac{\mathrm{d}\rho_b}{\mathrm{d}\mathbf{r}_a} + \delta_{ab}\rho_a\boldsymbol{\nabla}\gamma_a \\ &= \sum_{c\in\mathcal{F}} m_c\frac{\mathrm{d}w_{bc}}{\mathrm{d}\mathbf{r}_a} &&= m_a\boldsymbol{\nabla}_a w_{ab} + \delta_{ab}\sum_{c\in\mathcal{F}} m_c\,\boldsymbol{\nabla}_a w_{ac}\end{aligned}$$

and (A.12) becomes

$$\begin{aligned}\mathbf{F}_a^p + \mathbf{F}_a^B &= -\sum_{b\in\mathcal{F}} m_b\frac{p_b}{\rho_b^2}\frac{\mathrm{d}\rho_b}{\mathrm{d}\mathbf{r}_a} \\ &= -\sum_{b\in\mathcal{F}} m_b\frac{p_b}{\gamma_b\rho_b^2}\left[\boldsymbol{\nabla}_a w_{ab} + \delta_{ab}\left(\sum_{c\in\mathcal{F}} m_c\,\boldsymbol{\nabla}_a w_{ac}\right) - \delta_{ab}\rho_a\boldsymbol{\nabla}\gamma_a\right] \\ &= -\sum_{b\in\mathcal{F}} m_a m_b\left(\frac{p_b}{\gamma_b\rho_b^2} + \frac{p_a}{\gamma_a\rho_a^2}\right)\boldsymbol{\nabla}_a w_{ab} + \frac{m_a p_a}{\gamma_a\rho_a}\boldsymbol{\nabla}\gamma_a\end{aligned}$$

We can see these calculi that the density ρ and the function γ must be depends only on positions if we expect the correction to be effective. So we must use a a time discretisation where the variation of the quantity $\gamma_a\rho_a$ depends only on the variation of positions such as the temporal scheme (2.26). Such a scheme gives in fact at any time:

$$\gamma_a\rho_a = \left(\gamma_a^0\rho_a^0 - \sum_{b\in\mathcal{F}} m_b\, w_{ab}^0\right) + \sum_{b\in\mathcal{F}} m_b\, w_{ab} \tag{A.13}$$

If the field ρ_a^0 is initialised at such that $\gamma_a^0\rho_a^0 = \sum_{b\in\mathcal{F}} m_b\, w_{ab}^0$, the derivation from the Lagrangian holds, but the pressure field will be chaotic. If the field ρ_a^0 is initialised at a density reference, say, ρ_0 the pressure field will be smoother. But, doing so, we will engender distinctions between particles from a free surface and from the inner fluid for instance. Indeed, if a particle initially next to a free surface with the same density ρ_0 as an other particle in the fluid, is forced to go in the middle of the fluid (due to a wave break for example), his density will be multiplied by almost $\frac{3}{2}$. That is to say that we are setting a non-homogeneous fluid by initialising the density at ρ_0 to correct the error done by the interpolation (A.10).

A.3 Skew-adjoinction of the operators *gradient* and *divergence*

The goal of this appendix is to prove that the two operators *gradient* and *divergence* defined by the Kulasegaram *et al.* method are skew-adjoint. We recall that they are defined by:

$$\begin{aligned}\widetilde{\mathbf{Grad}}_a\{A_b\} &\equiv \rho_a\sum_{b\in\mathcal{F}} m_b\left(\frac{A_a}{\gamma_a\rho_a^2} + \frac{A_b}{\gamma_b\rho_b^2}\right)\boldsymbol{\nabla}w_{ab} - \frac{A_a}{\gamma_a}\boldsymbol{\nabla}\gamma_a \\ \widetilde{\mathrm{Div}}_a\{\mathbf{A}_b\} &\equiv -\frac{1}{\gamma_a\rho_a}\sum_{b\in\mathcal{F}} m_b\mathbf{A}_{ab}.\boldsymbol{\nabla}w_{ab} + \frac{1}{\gamma_a}\mathbf{A}_a.\boldsymbol{\nabla}\gamma_a\end{aligned} \tag{2.7}$$

for two arbitrary fields of scalar $\{A_b\}$ and of vector $\{\mathbf{B}_b\}$. We also recall that the skew-adjunction property means that the following property holds:

$$\left\langle \widetilde{\mathbf{Grad}}_b\{A_a\},\, \mathbf{B}_b \right\rangle = -\left(A_b,\, \widetilde{\mathrm{Div}}_b\{\mathbf{B}_a\}\right) \tag{1.9}$$

where the dot products are defined by:

$$\begin{aligned} \langle \mathbf{A}_b,\, \mathbf{B}_b \rangle &\equiv \sum_{b\,\in\,\mathcal{F}} V_b \mathbf{A}_b.\mathbf{B}_b \\ (A_b,\, B_b) &\equiv \sum_{b\,\in\,\mathcal{F}} V_b A_b B_b \end{aligned} \tag{1.10}$$

Thus, we have:

$$\begin{aligned} \left\langle \widetilde{\mathbf{Grad}}_b\{A_a\},\, \mathbf{B}_b \right\rangle &= \sum_{b\,\in\,\mathcal{F}} V_b \widetilde{\mathbf{Grad}}_b\{A_a\}.\mathbf{B}_b \\ &= \sum_{b\,\in\,\mathcal{F}} V_b \left[\rho_b \sum_{c\,\in\,\mathcal{F}} m_c \left(\frac{A_b}{\gamma_b \rho_b^2} + \frac{A_c}{\gamma_c \rho_c^2} \right) \boldsymbol{\nabla} w_{bc} - \frac{A_b}{\gamma_b} \boldsymbol{\nabla} \gamma_b \right] .\mathbf{B}_b \\ &= \sum_{b,\,c\,\in\,\mathcal{F}} m_b m_c \frac{A_b}{\gamma_b \rho_b^2} \boldsymbol{\nabla} w_{bc}.\mathbf{B}_b + \underbrace{\sum_{b,\,c\,\in\,\mathcal{F}} m_b m_c \frac{A_c}{\gamma_c \rho_c^2} \boldsymbol{\nabla} w_{bc}.\mathbf{B}_b}_{= -\sum_{b,\,c\,\in\,\mathcal{F}} m_b m_c \frac{A_b}{\gamma_b \rho_b^2} \boldsymbol{\nabla} w_{bc}.\mathbf{B}_c} - \sum_{b\,\in\,\mathcal{F}} V_b A_b \frac{1}{\gamma_b} \mathbf{B}_b.\boldsymbol{\nabla} \gamma_b \\ &= -\sum_{b\,\in\,\mathcal{F}} V_b A_b \left[-\frac{1}{\gamma_b \rho_b} \sum_{c\,\in\,\mathcal{F}} m_c \mathbf{A}_{bc}.\boldsymbol{\nabla} w_{bc} + \frac{1}{\gamma_b} \mathbf{A}_b.\boldsymbol{\nabla} \gamma_b \right] \\ &= -\sum_{b\,\in\,\mathcal{F}} V_b A_b \widetilde{\mathrm{Div}}_b\{\mathbf{B}_c\} \\ &= -\left(A_b,\, \widetilde{\mathrm{Div}}_b\{\mathbf{B}_a\}\right) \end{aligned} \tag{A.14}$$

where we have used the antisymmetry of the kernel gradient and have exchanged the mute indices b and c to complete the prove. The prove of the skew-adjunction of the operator (1.7) presented in Chapter 1 is just a special case of the present prove where γ_a is fixed at 1 everywhere and $\boldsymbol{\nabla}\gamma \equiv 0$.

Bibliography

[1] *Code_ Saturne : a Finite Volume Code for the Computation of Turbulent Incompressible Flows - Industrial Applications*, vol. 1 (International Journal on Finite Volumes, 2004).

[2] J. Bonet & T. S. L. Lok, Variational and momentum preservation aspects of Smooth Particle Hydrodynamic formulations, *Computer Methods in applied mechanics and engineering* 1999, **180**, 97–115.

[3] G. Colicchio, M. Greco & O.M. FaltinsenMarongiu, Fluid-body interaction on a Cartesian grid: dedicated studies for a CFD validation Proc., in 21^{st} *International Workshop on Water Waves and Floating Bodies*, Loughborough, UK, 2006 .

[4] Violeau D. & Issa R., *Guide to the SPARTACUS-2D V1P2 code: Lagrangian modelling of two-dimensional laminar and turbulent flows using the SPH method*, vol. HP-75/04/046/A (EDF R&D, restricted accessibility, 2007).

[5] R. A. Dalrymple & B. D. Rogers, Numerical modeling of water waves with the SPH method, *Coastal Engineering* February 2006, **53** (2-3), 141–147.

[6] R. Das & P. W. Cleary, Modelling 3D fracture and fragmentation in a thin plate under high velocity projectile impact using SPH, in *Proc. IIIrd SPHERIC International Workshop*, Lausanne, Swiss, 2008 .

[7] M. De Leffe, D. Le Touzé & B. Alessandrini, Normal flux method at the boundary for SPH, in 4^{th} *SPHERIC workshop*, Nantes, France, 2009 p. 149 – 156.

[8] A. Di Monaco, S. Manenti, M. Gallati, S. Sibilla, G. Agate, R. Guandalini & A. Maffio, A semi-analytic approach for SPH modelling of solid boundaries, in 4^{th} *SPHERIC workshop*, Nantes, France, 2009 p. 165 – 172.

[9] J. Feldman & J. Bonet, Dynamic refinement and boundary contact forces in SPH with applications in fluid flow problems, *Int. Journal for Numerical Methods in Engineering* 2007, **72** (3), 295 – 324, Meshfree Methods: Recent Advances and New Applications.

[10] M. Ferrand, D. Laurence, B.D. Rogers & D. Violeau, Improved time scheme integration approach for dealing with semi analytical boundary conditions in SPARTACUS2D, in *Proc. Vth SPHERIC International Workshop*, Manchester, UK, 2010 .

[11] R. A. Gingold & J. J. Monaghan, Smoothed Particle hydrodynamic: theory and application to non-spherical stars, *Monthly Notices of the Royal Astronomical Society* 1977, **181**, 375–389.

[12] H. Goldstein, C. Poole & J. Safko, *Conservation of the Hamiltonian* (Addison Wesley, San Francisco, 2002), 3^{rd}*edition*.

[13] J.M. Hervouet, *Hydrodynamics of Free Surface Flows: Modelling with the Finite Element Method* (John Wiley, 2007).

[14] R. Issa, E. S. Lee, D. Violeau & D. Laurence, Incompressible separated flows simulations with the smoothed particle hydrodynamics gridless method, *International Journal for Numerical Methods in Fluids* 2005, **47** (10-11), 1101–1106.

[15] S. Kulasegaram, J. Bonet, R. W. Lewis & M. Profit, A variational formulation based contact algorithm for rigid boundaries in two-dimensional SPH applications 2004.

[16] B. E. Launder & D. B. Spalding, Mathematical Models of Turbulence, *London: Academic Press* 1972.

[17] E. S. Lee, *Truly incompressible approach for computing incompressible flow in SPH and comparisons with the traditional weakly compressible approach*, Thèse de doctorat, University of Manchester Institute of Science and Technology, Manchester, UK, 2007.

[18] Leon B. Lucy, A Numerical Approach to Testing the Fission Hypothesis, *The Astronomical Journal* 1977, **82** (12), 1013–1924.

[19] J. C. Marongiu, F. Leboeuf & J. Caro, Low Mach number numerical schemes for the SPH-ALE method. Application in free surface flows in Pelton turbines, in 4^{th} *SPHERIC workshop*, Nantes, France, 2009 p. 323 – 330.

[20] J. C. Marongiu, F. Leboeuf & E. Parkinson, Numerical simulation of the flow in a Pelton turbine using the meshless method SPH and a new simple solid boundary treatment, in *7th European Conference on Turbomachinery Fluid Dynamics and Thermodynamics*, Athens, Greece, 2007 .

[21] J. E. Marsden & M. West, Discrete mechanics and variational integrators, *Acta Numerica* 2001, **10** (-1), 357–514.

[22] J.J. Monaghan & J.B. Kajtar, SPH particle boundary forces for arbitrary boundaries, *Computer Physics Communications* 2009, **180** (10), 1811 – 1820.

[23] J. J. Monaghan, Smoothed Particle Hydrodynamics, *Annual review of Astronomy and Astrophysics* 1992, **30**, 543–574.

[24] J. J. Monaghan, Simulating free surface flows with SPH, *Journal of Computational Physics* 1994, **110**, 399–406.

[25] J. J. Monaghan, SPH without a tensile instability, *Journal of Computational Physics* 1999, **159**, 290–311.

[26] J. J. Monaghan, Smoothed particle hydrodynamics, *Reports on Progress in Physics* 2005, **68**, 1703–1759.

[27] Joseph P. Morris, Patrick J. Fox & Yi Zhu, Modeling Low Reynolds Number Incompressible Flows Using SPH, *Journal of Computational Physics* 1997, **136**, 214–226.

[28] G. Oger, M. Doring, B. Alessandrini & P. Ferrant, An improved SPH method: Towards higher order convergence, *Journal of Computational Physics* 2007, **225** (2), 1472 – 1492.

[29] P. A. Patsis & E. Athanassoula, SPH simulations of gas flow in barred galaxies. Effect of hydrodynamical and numerical parameters, *aap* 6 2000, **358**, 45–56.

[30] S. B. Pope, *Turbulent Flows.* (Cambridge University Press, 2000).

[31] D. Shepard, A two dimensional function for irregularly spaced data, in *ACM National Conference*, 1968 .

[32] J. P. Vila, Weighted particle previous termmethodsnext term and smooth particle hydrodynamics., *Math. Models Meth. Appl. Sci.* 1999, **9** (2), 161–209.

[33] D. Violeau, *The Mechanics of weakly compressible flows and its application to the SPH method* (to be published, 2010).

[34] D. Violeau & R. Issa, Numerical modelling of complex turbulent free-surface flows with the SPH method: an overview, *International Journal for Numerical Methods in Fluids* 2007, **53** (2), 277–304.

[35] D. Violeau, R. Issa, S. Benhamadouche, K. Saleh, J. Chorda & M.-M. Maubourguet, Modelling a fish passage with SPH and Eulerian codes: the influence of turbulent closure, in *Proc.* III^{rd} *SPHERIC International Workshop*, Lausanne, Suisse, 2008 p. 85–91.

[36] H. Wendland, Piecewise polynomial, positive definite and compactly supported radial functions of minimal degree, *Advances in Computational Mathematics* December 1995, **4** (1), 389–396.

[37] R. Xu, *An Improved Incompressible Smoothed Particle Hydrodynamics Method and Its Application in Free-Surface Simulations*, Thèse de doctorat, University of Manchester, Institute of Science and Technology, Manchester, UK, 2009.